Final Report

Synthesis of N-Doped Ordered Mesoporous Carbons with Immobilization of Ni or Co as Alternative Counter Electrode Materials for Dye-Sensitized Solar Cells (DSCs)

By Dr. Panitat Hasin

January/ 2016

Contract No TRG
5780277

Final Report

Synthesis of N-Doped Ordered Mesoporous Carbons with Immobilization of Ni or Co as Alternative Counter-Electrode Materials for Dye-Sensitized Solar Cells (DSCs)

Researcher Institute
Dr. Panitat Hasin Kasetsart University

This project granted by the Thailand Research Fund

Abstract

Project Code : TRG 5780277

Project Title : Synthesis of N-Doped Ordered Mesoporous Carbons with Immobilization of Ni or Co as Alternative Counter-Electrode Materials for Dye-Sensitized Solar Cells (DSCs)

Investigator : Dr. Panitat Hasin

E-mail Address : fscipths@ku.ac.th

Project Period : 17 July 2014 – 17 July 2016

บทคัดย่อ:

วัสดุคาร์บอนที่มีรูพรุนในระดับนาโนที่ถูกเจือด้วยธาตุไนโตรเจนและมีโลหะ Ni (Ni-N-MC) หรือ Co (Co-N-MC) เป็นองค์ประกอบ ถูกสังเคราะห์โดยวิธีพอลิเมอร์ไรเซชั่นของพอลิอะนิลีนในรูพรุนระดับนาโนของวัสดุซิลิกาเพื่อใช้เป็นขั้วเคาน์เตอร์อิเล็กโทรดราคาถูกในเซลล์แสงอาทิตย์ชนิดสีย้อมไวแสง จากผลการทดลองที่ได้พบว่า Co-N-MC และ Ni-N-MC มีสมบัติการเร่งเชิงเคมีไฟฟ้าต่อปฏิกิริยาการรับอิเล็กตรอนของ I_3^- ที่ดีกว่า N-MC อย่างมีนัยสำคัญ เนื่องจากวัสดุ Co-N-MC และ Ni-N-MC ที่เตรียมได้นั้นเป็นการนำเอาสมบัติการนำไฟฟ้าที่สูงและสมบัติการเร่งปฏิกิริยาเชิงเคมีไฟฟ้าที่ดีมารวมอยู่ในวัสดุเดียวกัน โดยที่ Co หรือ Ni ทำหน้าที่เป็นตัวเร่งปฏิกิริยาเชิงเคมีไฟฟ้า ในขณะที่ N-MC ทำหน้าที่เป็นตัวนำไฟฟ้า ซึ่งสามารถพิสูจน์ได้จากค่าความต้านทานการแลกเปลี่ยนประจุ (R_{ct}) ตรงบริเวณรอยต่อระหว่างขั้วเคาน์เตอร์อิเล็กโทรดและสารละลายอิเล็กโทรไลต์ที่ต่ำ นอกจากนี้ยังพบว่าวัสดุ Co-N-MC และ Ni-N-MC ยังมีพื้นที่ผิวสูงและมีขนาดรูพรุนที่ใหญ่อีกด้วย ซึ่งทำให้สารละลายอิเล็กโทรไลต์เคลื่อนที่ได้เร็วขึ้น ยิ่งไปกว่านั้นยังพบว่าวัสดุ Co-N-MC และ Ni-N-MC มีปริมาณ pyridinic N และ quaternary N มาก ซึ่งส่งผลให้สมบัติการเร่งปฏิกิริยาเชิงเคมีไฟฟ้าของวัสดุดังกล่าวดีขึ้นเป็นอย่างยิ่ง นอกจากนี้ยังพบว่าขั้วเคาน์เตอร์อิเล็กโทรดที่ทำมาจาก Ni-N-MC ยังมีความเสถียรเชิงเคมีไฟฟ้ามากกว่าขั้วแพลทินัมอีกด้วย จากผลการทดลองพบว่าเซลล์แสงอาทิตย์ชนิดสีย้อมไวแสงที่ใช้ Ni-N-MC เป็นขั้วเคาน์เตอร์อิเล็กโทรดภายใต้การทำงานของสารละลาย I^-/I_3^- อิเล็กโทรไลต์มีประสิทธิภาพการเปลี่ยนพลังงานแสงเป็นพลังงานไฟฟ้าสูงถึง 8.42% ซึ่งมีค่าสูงกว่าเซลล์แสงอาทิตย์ชนิดสีย้อมไวแสงที่ใช้แพลทินัมเป็นขั้วเคาน์เตอร์อิเล็กโทรด (8.22%) นอกจากนี้เซลล์แสงอาทิตย์ชนิดสีย้อมไวแสงที่ใช้ N-MC (5.90%), Co-N-MC (6.80%) และ Ni-N-MC (6.95%) เป็นขั้วเคาน์เตอร์อิเล็กโทรดยังมีประสิทธิภาพการเปลี่ยนพลังงานแสงเป็นพลังงานไฟฟ้าสูงกว่าเซลล์แสงอาทิตย์ชนิดสีย้อมไวแสงที่ใช้ขั้วแพลทินัม (5.25%) ภายใต้การทำงานของสารละลาย di-5-(1-methyltetrazole) disulfide/5-mercapto-1-methyltetrazole *N*–tetramethylammonium salt (T_2/T^-) อิเล็กโทรไลต์อีกด้วย ดังนั้นวัสดุคาร์บอนที่มีรูพรุนในระดับนาโนที่ถูกเจือด้วยธาตุไนโตรเจนและมีโลหะ Ni หรือ Co เป็นองค์ประกอบจึงมีศักยภาพสูงในการนำมาใช้แทนขั้วแพลทินัมเพื่อเพิ่มประสิทธิภาพการเปลี่ยนพลังงานแสงเป็นพลังงานไฟฟ้าของเซลล์แสงอาทิตย์ชนิดสีย้อมไวแสงที่ใช้วัสดุคาร์บอนเป็นขั้วเคาน์เตอร์อิเล็กโทรด

Abstract:

Nanocomposites of cobalt or nickel species and N-doped mesoporous carbon (Co-N-MC or Ni-N-MC) were prepared by in situ polymerized mesoporous silica-supported polyaniline (PANI) and then explored as the counter electrodes (CEs) in dye-sensitized solar cells (DSCs). It is shown that Co-N-MC and Ni-N-MC significantly improve the electrocatalytic activity towards the reduction of I_3^- compared to N-MC. These are attributed to combining high electrical conductivity and electrocatalytic activity into one material: Co-N-MC or Ni-N-MC, in which Co or Ni species serve as the electrocatalysts and N-MC serves as an electrical conductor. These have been proved by much lower charge-transfer resistance (R_{ct}) at the CE/electrolyte interface. The high surface area and the large mesopores in the Co-N-MC or Ni-N-MC can speed up the transport of electrolyte species. Moreover, the predominating contents of pyridinic and quaternary N species in the Co-N-MC or Ni-N-MC framework are considered to contribute significantly to the electrocatalytic activity. Furthermore, Ni-N-MC CE exhibits much better electrochemical stability than platinized CE. The I^-/I_3^--based DSC using Ni-N-MC CE could reach a cell efficiency of 8.42%, which surpassed the efficiency of the DSC employing traditional platinized CE (8.22%). In addition, all N-doped mesoporous (N-MC (5.90%), Co-N-MC (6.80%), and Ni-N-MC (6.95%)) based DSCs showed the high performance than the cell with a platinized CE (5.25%) for the regeneration of organic redox couple, di-5-(1-methyltetrazole) disulfide/5-mercapto-1-methyltetrazole *N*-tetramethylammonium salt (T_2/T^-). The nanocomposites of Co or Ni species on N-MC matrix readily provide a possible solution to replace costly Pt-based CE and enhance the performance of DSCs with carbon based CEs.

Keywords : 3-5 words

N-Doped Ordered Mesoporous Carbon, Immobilization of Ni or Co, Polyaniline, Counter electrode, Dye-Sensitized Solar Cell

Final report content:

1. Abstract

Nanocomposites of cobalt or nickel species and N-doped mesoporous carbon (Co-N-MC or Ni-N-MC) were prepared by in situ polymerized mesoporous silica-supported polyaniline (PANI) and then explored as the counter electrodes (CEs) in dye-sensitized solar cells (DSCs). It is shown that Co-N-MC and Ni-N-MC significantly improve the electrocatalytic activity towards the reduction of I^-/I_3^- compared to N-MC. These are attributed to combining high electrical conductivity and electrocatalytic activity into one material: Co-N-MC or Ni-N-MC, in which Co or Ni species serve as the electrocatalysts and N-MC serves as an electrical conductor. These have been proved by much lower charge-transfer resistance (R_{ct}) at the CE/electrolyte interface. The high surface area and the large mesopores in the Co-N-MC or Ni-N-MC can speed up the transport of electrolyte species. Moreover, the predominating contents of pyridinic and quaternary N species in the Co-N-MC or Ni-N-MC framework are considered to contribute significantly to the electrocatalytic activity. Furthermore, Ni-N-MC CE exhibits much better electrochemical stability than platinized CE. The I^-/I_3^--based DSC using Ni-N-MC CE could reach a cell efficiency of 8.42%, which surpassed the efficiency of the DSC employing traditional platinized CE (8.22%). In addition, all N-doped mesoporous (N-MC (5.90%), Co-N-MC (6.80%), and Ni-N-MC (6.95%)) based DSCs showed the high performance than the cell with a platinized CE (5.25%) for the regeneration of organic redox couple, di-5-(1-methyltetrazole) disulfide/5-mercapto-1-methyltetrazole *N*-tetramethylammonium salt (T_2/T^-). The nanocomposites of Co or Ni species on N-

MC matrix readily provide a possible solution to replace costly Pt-based CE and enhance the performance of DSCs with carbon based CEs.

2. Executive summary

2.1 Introduction to Research

2.1.1 Introduction of dye-sensitized solar cell (DSC)

The availability of energy is one of the major influences on human life quality even before the industrial revolutions. The high and savage use of conventional sources of energy such as fossil resource or petroleum oil in energy generation are leading to forecasted energy and environmental crises. Developing an affordable, reliable, environmentally friendly energy technology in the future could be a potential solution to confront these problems. Renewable energy such as solar energy emerged as a feasible alternative because this technology generates electrical power from a direct conversion of sunlight without emission of both greenhouse gases and another polluting agent harming the environment and our society. This can be confirmed by N. S. Lewis since he mentioned in *Science* in 2007 that *"More energy from sunlight strikes Earth in 1 hour than all of the energy consumed by humans in an entire year."*[1] This means the harvest of a fraction of the solar energy reaching the Earth may solve the problem of both the energy shortages and global environment.[2] Therefore, intensive research articles from an expert in Chemistry, Physics, and Engineering working on solar technology have resulted in attention-grabbing to the different categories of organic and inorganic based solar cells.

Actually, silicon photovoltaic technology is market leader in photovoltaic technologies. However since Michael Grätzel invented dye-sensitized solar cells (DSCs) in 1991,[3] this new generation of photovoltaic technology has become one of the most promising and important technology in photovoltaic field. DSCs, the new

solar cell generation, with a nano-working electrode play a more important role in photo-electrochemical cells than classical solid-state homo and hetero-junction device. This technology offers a very low cost, easy fabrication, environmental-friendliness, and considerable power conversion efficiency (PCE).[4, 5] The schematic overview of the main components of a DSC is illustrated in Fig. 1.[6] DSC is composed of three main elements: A dye (sensitizer)-covered nanostructured wide bandgap semiconducting TiO_2 layer on a glass substrate coated with a thin film of transparent conductive oxide (TCO) layer such as fluorine doped tin oxide (FTO), a redox electrolyte, and counter electrode (CE).

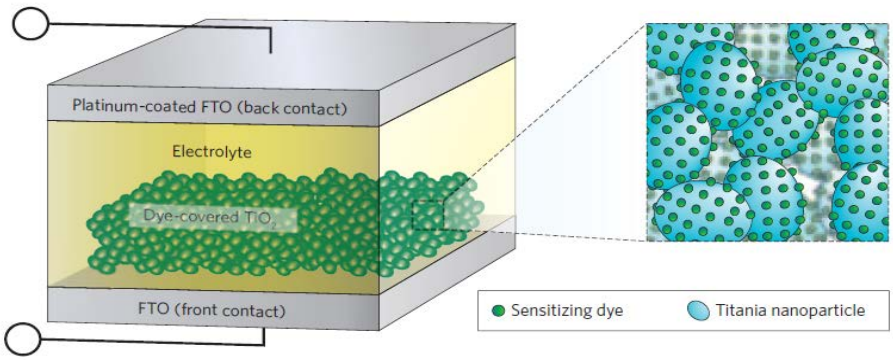

Fig. 1. Schematic of the structure of the dye sensitized solar cell.[6]

2.1.2 Mechanism operation

Fig. 2. shows a typical schematic energy diagram of DSCs. All photovoltaic devices present two important steps to convert photons to current:

1. Radiation absorption with electrical excitation.

2. Charge carriers separation.

Wide band gap oxide semiconductor materials, such as TiO_2, ZnO, or SnO_2 is deposited on transparent conducting oxide (TCO)-coated glass (photoelectrode) to provide the necessary large surface area to adsorb photosensitizers (dye molecules). Upon absorption of photons, the electrons of photosensitizers are excited from the ground state (S) or the highest occupied molecular orbital (HOMO) to the excited

state (S*) or the lowest unoccupied molecular orbital (LUMO) owing to the metal to ligand charge transfer (MLCT) transition as shown schematically in Figure 2. This process is represented by Eq. 1. Once the excited electrons are injected into the conduction band of the wide band gap semiconductor nanostructured TiO_2 electrode, the oxidation of the photosensitizer occurs (Eq. 2.). The injected electrons in the conduction band of TiO_2 are transported between the TiO_2 nanoparticles with diffusion toward the back contact (TCO) and then are extracted to the external load including wiring where the work done is delivered as an electrical energy. Consequently, the electrons reach the counter electrode (CE) (Eq. 3.). The oxidized redox mediator, I_3^-, in the electrolyte diffuses toward the counter CE and is reduced to I^- ions (Eq. 4.). The ground state of photosensitizer (S) is regenerated by accepting electrons of the oxidized photosensitizer (S^+) from I^- ion redox mediator. After that I^- gets oxidized to the oxidized state, I_3^-. This process is represented by Eq. 5. The movement of electrons in the conduction band of the mesoscopic TiO_2 films is accompanied by the diffusion of the charge–compensating cations in the electrolyte layer close to the surface of nanoparticles. Therefore, the electric power generation in DSC causes no permanent chemical change or transformation.[7]

Excitation process: $S + \text{photon} \longrightarrow S^*$ …(1)

Injection process: $S^* + TiO_2 \longrightarrow e^-(TiO_2) + S^+$ …(2)

Energy generation: $e^-(TiO_2) + CE \longrightarrow TiO_2 + e^-(CE) + \text{electrical energy}$ …(3)

Tri-iodide reduction: $I_3^- + 2e^-(CE) \longrightarrow 3I^-$ …(4)

Regeneration of dye: $2S^+ + 3I^- \longrightarrow 2S + I_3^-$ …(5)

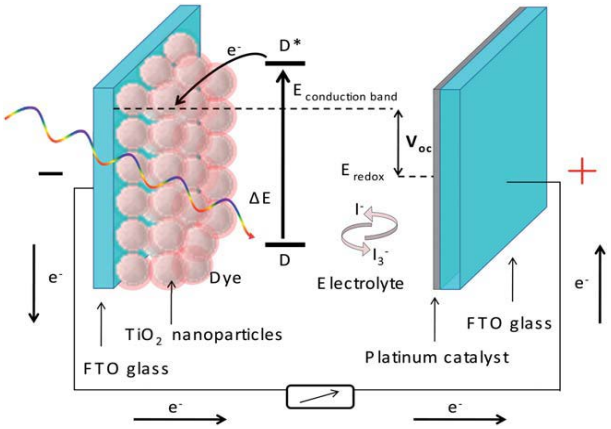

Fig. 2. Schematic illustration of operation principle of dye sensitized solar cell.[7]

2.1.3 Counter electrode

In a DSC system, the traditional platinum CE works as an electron collector and an electrocatalyst for regeneration of redox couple in the electrolyte, which can be prepared by the thermal decomposition of H_2PtCl_6, a platinum precursor, on F-doped tin oxide (FTO) conductive glass. Pt exhibits good electron collector and high electrocatalytic activity for reducing the I_3^- to I^- by electron migrating through the external circuit.[8, 9] Pt CE is an appropriate choice to a single-minded pursuit of high efficiency. Considering the practical and economic issues, Pt CE is considered to be unsuitable for mass production of DSCs due to its drawbacks of scarce resource and high expense.[10, 11] Hence, finding other cheaper materials with relatively high efficiency to replace the expensive Pt as the electrochemical catalysts on CEs is required to further bring down the final costs of devices. It is therefore highly urgent to develop alternative low-cost CE materials but well-performed CE.

2.1.4 Current Challenge

Among all the alternative catalysts to Pt,[10, 11] carbon materials including graphite,[12] carbon black,[13] carbon nanofiber,[14] carbon nanotube,[15-17] well-ordered mesoporous carbon,[18] and graphene[19, 20] were first considered due to their excellent electrical conductivity, low cost, nontoxicity, and reasonable electrocatalytic activity. On the basis of previous research, although carbon CEs show high electrocatalytic

activity, there still remains chief weakness for carbon CEs. The unsolved problem is that thick film (about several tens of millimeters) is required for conventional carbon CEs to attain desired catalytic activity limiting their optical transmittance. This leads to difficulty in fabricating bifacial DSCs. This may cause lower PCEs of those DSCs using carbon CEs compared to the one with Pt CE. To retain the thickness of electrocatalyst on CEs, the electrocatalytic activity of carbonaceous CEs should be enhanced by increasing the active surface area in order to ensure facile molecular conversion of reactants to products resulting in possessing high surface reactivity.[21] Therefore, applying the mesoporous carbon with a narrow pore size distribution, tunable pore sizes, high surface area, and large pore volume as a CE in DSCs could be a possible solution to improve the electrocatalytic activity of carbon-based materials.[22, 23] Besides high electrocatalytic activity, an ideal electrocatalyst should also have excellent electronic conductivity.[21] Among all carbonaceous materials, unfortunately the electrical conductivity of mesoporous carbon is low which still can not match up to that of Pt. Generally, the improvement in electrical conductivity of carbon materials could be achieved by doping with heteroatoms such as nitrogen or phosphorus due to the extra electrons obtained from the heteroatoms.[24, 25] Besides nonmetals, metals-mainly iron or cobalt ions-have also been used as dopants to improve the electrocatalytic activity of carbon-based materials. Furthermore, heteroatom doping, both nonmetals or metals, has also been demonstrated to introduce the electrocatalytic active sites and to enhance the surface hydrophilicity leading to facilitating the charge transfer between electrolyte and electrode and improving the electrolyte–electrode interactions, respectively.[26, 27]

Indeed, doping with heteroatoms (boron, nitrogen, oxygen, phosphorus, or metals) into carbon materials has been studied for some years with attempts to enhance the electrocatalytic activities and long-term operation stability for oxygen

reduction in fuel cells.[26-28] Such previous study has clearly shown that carbon materials functionalized by doping with heteroatoms exhibit decent electrocatalytic activities, good stability, and more tolerance to crossover/poisoning effects relative to a platinum electrode.[29, 30] The recent discovered electrocatalytic reduction activities, along with the doping-enhanced electrical conductivities and surface hydrophilicity, made N-doped carbonaceous materials immobilized by metal to be the ideal candidates for low cost, but very effective CEs in DSCs. As far as we are aware, however, no N-doped mesoporous carbons immobilized by metal has been used as a metal-free electrocatalyst at the CEs for I_3^- reduction in DSCs.

In this proposal, the aim is to design a superior catalyst through in situ synthesis by combining high electrical conductivity and catalytic activity into one material: N-doped mesoporous carbons immobilized by Ni or Co, in which the nitrogen and oxygen as well as Ni or Co dopants serve as the electrocatalyst and mesoporous carbon serves as an electron collector. Although N-doping is normally carried out by the heat treatment of carbon material under nitrogen or ammonia atmosphere, possible control of nitrogen content in the mesoporous carbon could still not be done. In this regard, it will be a significant advancement if we can control the quantity of nitrogen in the mesoporous carbon. In this proposal, polyaniline (PANI) (Fig. 3.) is chosen as a nitrogen precursor for making the N-doped mesoporous carbons owing to its high N/C atomic ratio (0.167) and high molar weight, which prevents its vaporization at high temperatures.[31, 32]

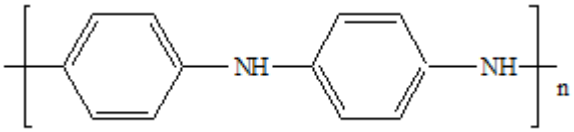

Fig. 3. The molecular structure of polyaniline (PANI).

We hope that the obtained N-doped mesoporous carbon immobilized by Ni or Co would show not only high surface area but also high N content due to the impeding small CN species vaporized during the pyrolyzing PANI precursor within the thermally robust nanosized cavities of SBA-15 used as the mesoporous template and oxygen precursor. This electrocatalyst could demonstrate the higher electrocatalytic activity and long-term stability.

2.2 Literature review

As mentioned above in the DSCs, the counter electrode (CE), one of the essential factors in achieving a highly efficient DSC device,[10] functions to transfer electrons from the external circuit and back to the redox electrolyte for I_3^- reduction. A Pt thin film deposited on a fluorine doped tin oxide (FTO) substrate often serves as a CE in conventional DSCs because of its high electrochemical activity for I_3^- reduction, excellent electrical conductivity, and corrosion resistance. However, Pt is a noble, relatively expensive, as well as rare metal and shows poor stability in a corrosive iodide/tri-iodide redox system.[33] The Pt CE costs over 40% of the whole photovoltaic cell, regardless of its fabrication approach. Therefore, to lower materials cost and achieve feasible large-scale production, a low-cost alternative material for CE with superior electrocatalytic activity, chemical stability, and high conductivity is highly desirable.

2.2.1 Carbon-based counter electrode used in dye-sensitized solar cell (DSC)

As more cost-effective materials for CE, carbon-based materials have been evaluated as the potential CEs for many years because of their high durability, excellent electrocatalytic activity, high electrical conductivity, large surface area, and low cost (~ 165,000% cheaper (per kg) than Pt).[13, 34-36]

2.2.1.1 Graphite/Activated carbon

Andreas Kay and Michael Gratzel[34] reported a new porous carbon electrode prepared from graphite powder with adding about 20% of carbon black as a CE of DSC. Compared to bare graphite electrode, the electrocatalytic activity of the composite was largely influenced by the very high surface area of carbon black, while the improved conductivity resulted from the partial filling of large pores between the graphite flakes with smaller carbon black aggregates. However, the energy conversion efficiency of DSC with this CE was found to be 30% lowering compared to the one with Pt CE, probably due to its much higher electrical resistance resulting in lower electrocatalytic activity.

Imoto et al.[35] tried to use a carbon CE consisting of an activated carbon powder in order to decrease the electrical resistance. The photocurrent-voltage characteristics were considerably enhanced which were due to both the large roughness factor and low electrical resistance of the activated carbon CE. After all, a high-performance activated carbon CE exhibit higher energy conversion efficiency than the traditional Pt CE.

2.2.1.2 Organic polymer

Yasuteru Saito et al.[37] demonstrated a low cost DSC using *p*-toluenesulfonate doped poly(3,4-ethylenedioxythiophene) (PEDOT-TsO) CE (Fig. 4.) with the enhancement of energy conversion efficiency in the DSC. This electrode shows low charge transfer resistance at the interface of the electrolyte and the PEDOT CE, owing to its porous structure. This leads to the increase of surface area of CE. Their promising result makes the porous PEDOT-TsO CE superior to Pt and carbon CEs in terms of fabrication process, fabrication cost and performance.

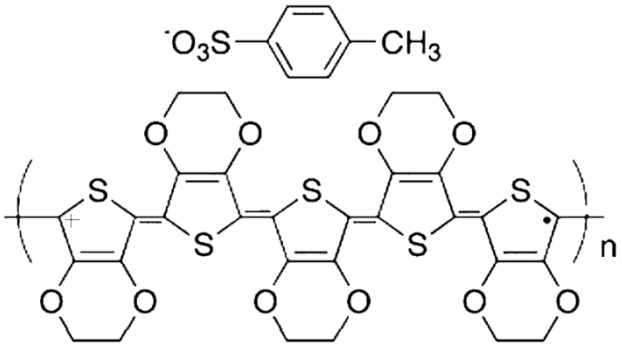

Fig. 4. Chemical structures of *p*-toluenesulfonate doped poly(3,4-ethylenedioxythiophene) (PEDOT-TsO).[37]

2.2.1.3 Nanosized carbon

To further increase the efficiency of the DSCs, the internal resistance of carbon CE needs to be decreased when the thickness of the film is above few tens of micrometers in order to attain comparable electrocatalytic performance of Pt CE. Easwaramoorthi Ramasamy et al.[38] compared the performance of DSC using nanosized carbon powder (Fig. 5.) as a CE to that using Pt CE. The surface area of nanosized carbon powder electrode increased with the thickness because of its porous structure. The increase of active area in the nanosized carbon powder CE improved the photovoltaic performance of the DSC. This improvement corresponds to the decrease of charge transfer resistance at the interface of the electrolyte and the nanosized carbon powder CE. These results suggested that the increase of surface area of CE was effective to enhance photovoltaic performance in the DSC. The nanosized carbon powder CE would make DSC technology one step closer to commercialization.

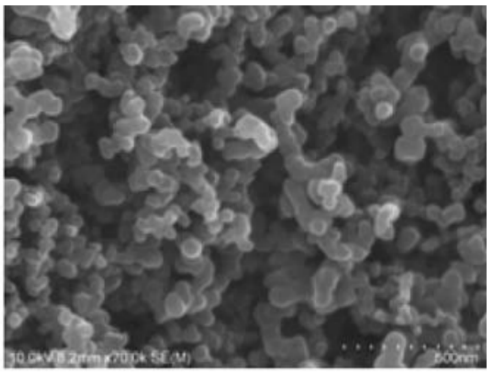

Fig. 5. FESEM image of 20 μm thick carbon layer on FTO glass substrate.[38]

2.2.1.4 Carbon nanotubes (CNTs)

Recently, carbon nanotubes (CNTs) are of interest because of the combined advantages of a much great surface area to volume ratio, high chemical stability, good mechanical properties, and high electrical conductivity. Easwaramoorthi Ramasamy et al.[16] also reported the successful application of spray coated multi-wall CNTs (Fig. 6.) as the electrocatalysts for tri-iodide reduction in a DSC. The porous and three dimensional network of multi-wall CNTs facilitates the fast electron transfer kinetics, resulting in a reduced charge transfer resistance at the CE/electrolyte interface and an improved energy conversion efficiency to 7.59%.

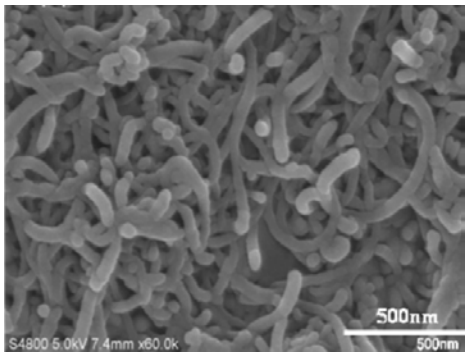

Fig. 6. Photograph of spray coated multi-wall CNT film on FTO glass substrate.[16]

The previous works focusing on the electrocatalytic applications of multi-wall CNTs show that the edge planes of the graphene, a constituent of multi-wall CNTs, have more favorable electron-transfer kinetics than the basal planes. Single-wall and hollow-structure multi-wall CNTs, which are composed of nearly perfect atomically

smooth basal plane may not pave the way for novel electrocatalytic applications.[39, 40] Won Jae Lee et al.[15] described the use of bamboolike-structure multiwall CNTs on FTO glass substrate as the CEs (Fig. 7.) for I_3^- reduction in DSCs. Defect-rich edge planes of bamboolike-structure multiwall CNTs reduced the charge transfer resistance at the CE/electrolyte interface and led to an energy conversion efficiency of 7.7% under 1 sun illumination (100 mW/cm^2, air mass 1.5 G).

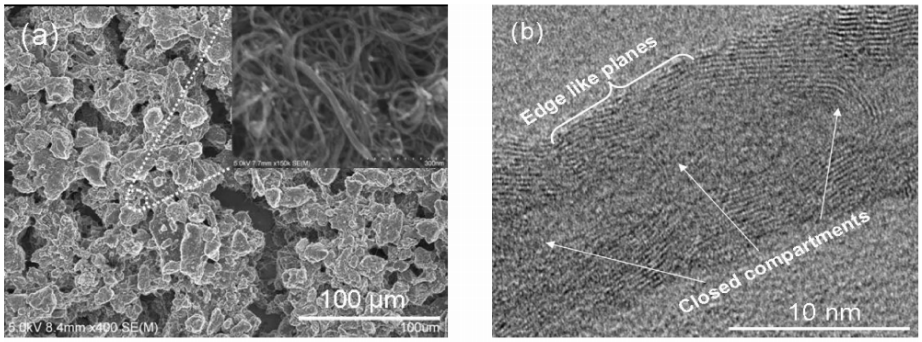

Fig. 7. Microstructure characterization of multiwall CNTs: (a) FE-SEM and (b) TEM images of the bamboolike structure in multiwall CNTs used in this study.[15]

2.2.1.5 Carbon composite

Besides the disadvantage of the thick carbon films as previously described, another chief weakness is the poor connection between carbon materials and the substrate (FTO glass) causing the long-term instability in those DSCs using the carbon CEs.[11] The carbon/TiO_2 composite (Fig. 8.) was synthesized by Prakash Joshi et al.[41] to improve the binding strength between carbon materials and the substrate (FTO glass) which carbon acts as a catalyst and the TiO_2 functions as a binder. Although the energy conversion efficiency (η) of carbon/TiO_2 composite-based DSC was slightly lower than that of Pt-based cell, its circuit current density (J_{SC}) and open circuit voltage (V_{OC}) were comparable. The reason for lower cell performance using the carbon/TiO_2 CE was because of its lower fill factor (*FF*) than that of Pt-based cell, probably caused by high series resistance which needs to be solved in the future.

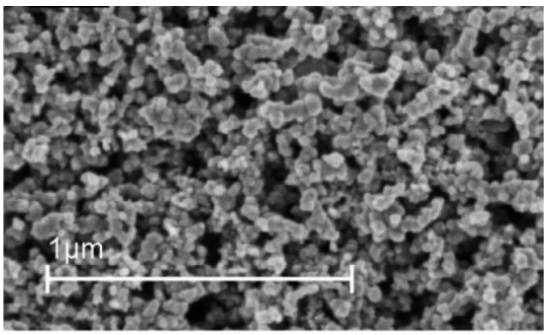

Fig. 8. Top view SEM image of the thick carbon/TiO_2 composite layer.[41]

2.2.1.6 carbon nanofibers

Prakash Joshi et al.[14] tried to improve the series resistance of the carbonaceous CEs by using electrospun carbon nanofibers (ECNs) (Fig. 9.). These cells have shown low charge-transfer resistance, large capacitance, and fast reaction rates of tri-iodide reduction. However, the total series resistance of ECN-based cells was still found to be a little higher than that of Pt-based cells, leading to a slightly lower *FF*. A promising approach to decrease total series resistance is to reduce the thickness of the ECNs CE by using thinner and highly porous ECNs.

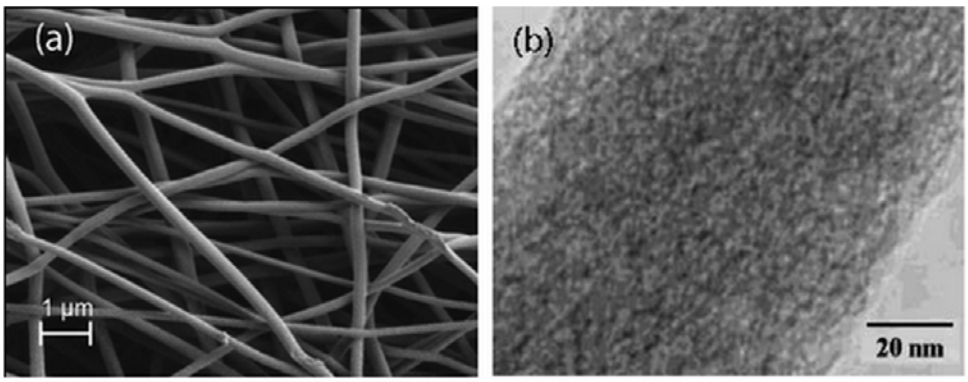

Fig. 9. (a) Top view SEM image of the electrospun carbon nanofiber (ECN) sheets. (b) TEM image of a single typical ECN.[14]

2.2.1.7 Graphene

Graphene has attracted extensive attention in condensed-matter physics and materials science.[42] Graphene is composed of a flat two-dimensional (2D) sheet

of hexagonally arrayed sp^2-covalently bonded carbon atoms arranged into a honeycomb lattice as shown in Figure 10.[43]

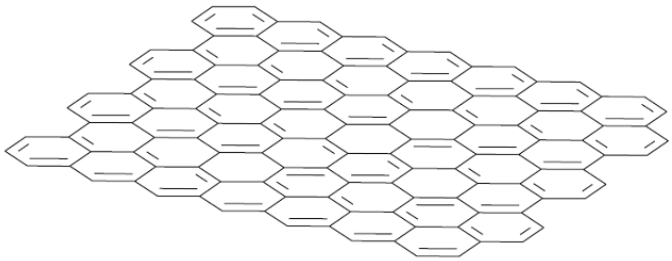

Fig. 10. Graphene structure.[43]

Very recently, graphene has been emerged to be a potential electrocatalyst for DSC cathodes, due to its excellent conductivity, exceptional surface area, and high electrocatalytic activity.[44-46] Wenjing Hong et al.[45] demonstrated a CE in DSC using a transparent thin graphene/PEDOT-PSS film (Fig. 11.). From photocurrent-voltage characteristics, the energy conversion efficiencies of the DSCs with the CE of graphene/PEDOT-PSS composite films were higher than those of PEDOT/PSS. The composite electrodes can be fabricated at room temperature providing them to be the one of candidates for a CE in DSC using plastics as the substrates. Furthermore, the high transmittance of the films makes them with potential applications in power-producing windows or metal-foil-supported DSCs. However, the low fill factor (*FF*) of DSC with a graphene/PEDOT–PSS CE still limited its performance compared to that with Pt CE.

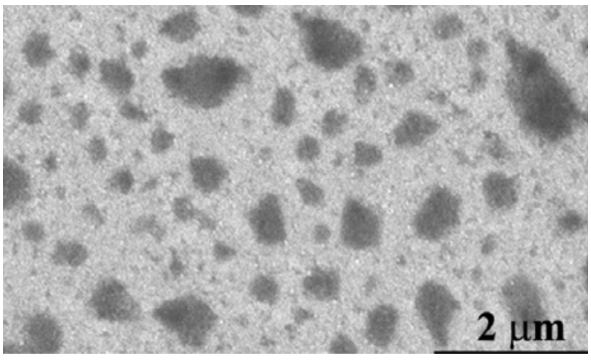

Fig. 11. SEM image of the graphene/PEDOT-PSS film.[45]

To further increase the conversion efficiency of the DSCs using graphene as a CE, the graphene-based multi-walled carbon nanotubes (GMWNTs) (Fig. 12.) were applied as the CE by Hyonkwang Choi et al.[46] to enhance the fill factor (*FF*) of DSCs. As a result, the DSC with the CE of graphene-based multi-walled carbon nanotubes (GMWNTs) showed comparable energy conversion efficiency with those of MWNTs CE. The results demonstrate that GMWNTs are the promising substitute for the expensive Pt CE for low-cost DSCs.

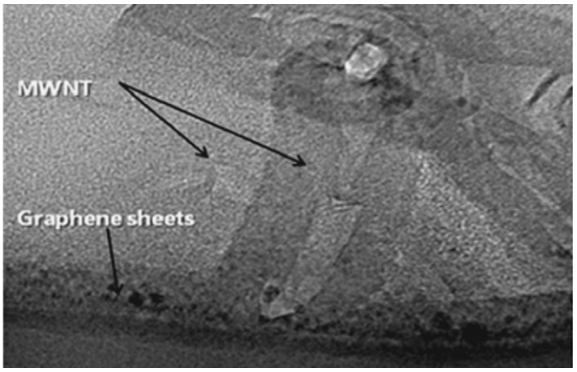

Fig . 12. Cross-sectional HRTEM image of GMWNTs.[46]

Unfortunately, the electrical conductivity and the electrocatalytic activities of carbon materials without modifications are low which still can not match up to those of Pt. To further improve and tune the device performance for DSCs with a carbon-based CE, it is important to trade off between its electrical conductivity and the electrocatalytic activity.[24, 25, 47] Joseph D. Roy-Mayhew et al.[25] suggested that increasing the number of defect sites (e.g. oxygen-containing functional groups in reduced graphene oxide) often leads to an increase of apparent electrocatalytic activity of carbon materials for the tri-iodide reduction. A high effective charge-transfer resistance (R_{ct}) may be observed when the perfect carbon materials are used as the CEs in DSCs owing to a small amount of active sites for catalyzing the reduction of tri-iodide. Although the chemical functionalization of carbon surface can introduce electrocatalytic active sites, the conjugated structure in the graphitic basal plane is

damaged resulting in a concomitant decrease in the electrical conductivity. Unlike the chemical functionalization, the introduction of surface heteroatoms (e.g. nitrogen, oxygen, boron, or phosphorus) into the carbon network could further cause electron modulation to introduce desirable electrocatalytic active sites with a minimized change of the conjugation length for many electrocatalytic processes of practical significance.[26] Furthermore, there are some reports revealed that heteroatom doping is vital factor for enhancing the electrical conductivity and surface hydrophilicity in order to facilitate charge-transfer and electrolyte–electrode interactions, respectively, because they significantly affect the electron transport in electrodes and active sites for electrocatalytic activities.[26, 27] As reported, generally nitrogen or oxygen doping into sp^2-hybridized carbon frameworks (called N- or O-doping) has clearly shown that nitrogen-doped carbon nanomaterials can effectively modulate their electrical property and chemical reactivity.[26-28, 30, 48] The additional negative charges from the lone pair electron in nitrogen can get into the delocalized π system leading to a significant improvement of the interaction between carbon structures and foreign molecules.[49] These results in higher electrocatalytic activities and better long-term operation stability which are of central importance in catalysis.[29, 30] The recent discovered electrocatalytic reduction activities, along with the doping-enhanced electrical conductivities and surface hydrophilicity, brought along tremendous technological implication of N- and O-doped carbonaceous materials for low cost, but very effective CEs in DSCs due to the potential replacement of traditional expensive platinum catalysts.

It has been suggested that the introduction of oxygen-containing functional groups has a great influenced on the observed electrocatalytic performance of carbonaceous materials, while the effect of the degree of material functionalization on apparent electrocatalytic performance has not been extensively studied in detail.[50, 51]

Functionalized graphene sheets (FGSs) were used as a stand-alone electrocatalyst in DSC and the effect of tuning potentially electrocatalytic functional groups on FGS was investigated by Joseph D. Roy-Mayhew et al.[25] The amount of oxygen-containing functional groups, such as hydroxyls, carbonyls, and epoxides, as shown in Fig. 13.[52-54] can be tuned by thermal processing of the material, leading to changing its carbon to oxygen (C/O) ratio.[55] The increased electrical conductivity with the decreased number density of oxygen-containing functional groups on the surface of the FGSs was obtained by thermal treatment at the temperatures up to 1000 °C. In addition, the lattice defect in FGSs could be healed by annealing process at temperatures up to higher than 1500 ^{o}C.[53, 56] An advantage of their material is that the effect of the C/O ratio on the electrocatalytic activity of the FGS can be systematically examined because the C/O ratio can be adjusted. Furthermore, fabricating a more porous FGS shows the improvement of electrocatalytic activity. The FGSs with the C/O ratio of 13 (Fig. 14.) showed excellent electrocatalytic activity towards tri-iodide reduction. Tailoring the functionalization or morphology of the FGS electrodes is expected to significantly decrease their charge-transfer resistance and to reduce the production cost of catalytic, flexible, and conductive CEs for DSCs.

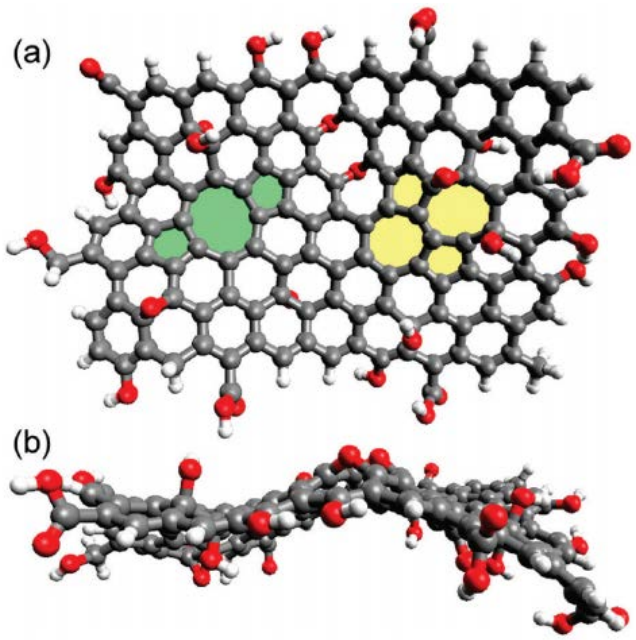

Fig. 13. (a) Schematic of functional groups and lattice defects on an FGS. Epoxides and hydroxyls are on both sides of the graphene plane, while carbonyl and carboxyl groups are at the edges. A 5-8-5 defect (green) and a 5-7-7-5 (Stone-Wales) defect (yellow) are also shown. Carbon atoms are gray, oxygen atoms are red, and hydrogen atoms are white. (b) Side view exphasizing the topology of the sheet.[25, 52-54]

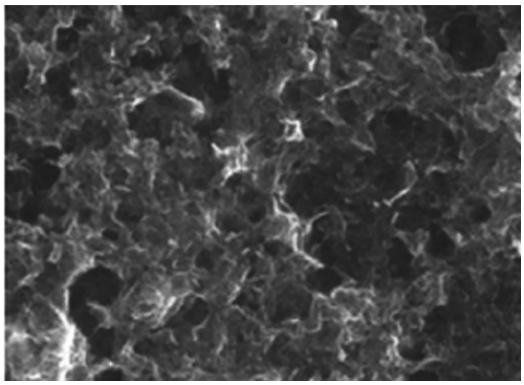

Fig. 14. SEM image of film of FGS with the C/O ratio of 13.[25]

2.2.1.8 Order mesoporous carbons (OMC)

Order mesoporous carbons (OMC) have emerge as the versatile carbon materials because of their unique features and promising applications.[23, 57] Recently, Easwaramoorthi Ramasamy and Jinwoo Lee[58] have successfully employed OMC (Fig. 15.) as favorable a CE material in DSCs. The charge transfer resistance and energy conversion efficiency of OMC-based DSC showed promising results. The high catalytic effects mainly arose from the large sized mesopores with an interconnected pore structure of the sub-micron size ordered mesoporous carbon particles favoring the fast diffusion of redox species. This study suggests that the photovoltaic performance in Pt-free DSCs may be improved by using OMC.

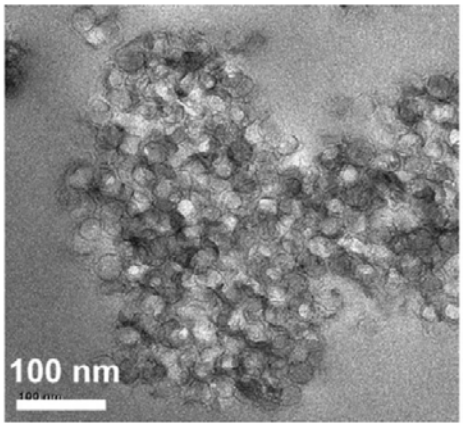

Fig. 15. TEM images of microtomed order mesoporous carbon.[58]

2.2.1.9 N-doped carbon

Lee et al.[17] have, for the first time, prepared vertically aligned nitrogen doped-CNT (N-CNT) (Fig. 16.) and have demonstrated its application as a metal-free electrocatalyst for the reduction of tri-iodide to replace the Pt cathode in DSCs, leading to a power conversion efficiency up to 7.34%. This unique material has several advantages: (1) Vertically aligned CNT arrays provide an extremely large surface area with a highly ordered geometry. (2) N-CNTs possess high electrical conductivity and catalytic activity. The doped nanotubes are metallic and exhibit high electrocatalytic activity because the substituted electron-rich nitrogen doped in a CNT graphite layer reduces the band gap of the CNT.[59, 60] This work also indicated that N-CNTs, in particular, and nitrogen-doped carbon nanomaterials, in general, can be used as the low-cost and substrate-independent Pt-free CEs for DSCs.

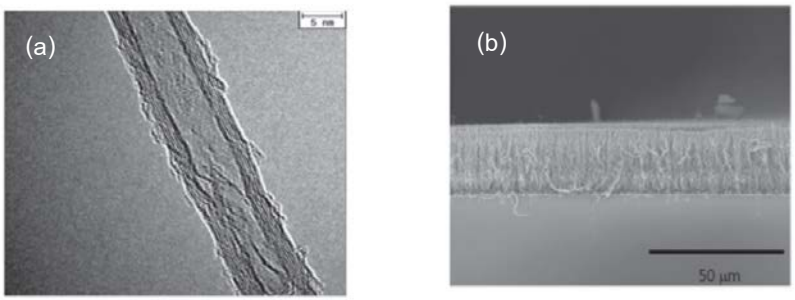

Fig. 16. (a) HR-TEM image of N-CNTs and (b) SEM image of transferred N-CNT arrays.[17]

A nitrogen-doped 3D graphene foam (N-GF)[19] (Fig. 17.) was synthesized and used as a substitute for Pt CE in DSCs by Yuhua Xue et al. The DSC with N-GFs-based CE exhibited a conversion efficiency high up to 7.07%. This value of efficiency is comparable to that of a DSC with a Pt CE constructed under the same condition. The authors also demonstrated that further electrode/device optimization will lead to DSCs based on the N-GF CE with outperforming even their counterparts with a Pt CE. Overall, nitrogen-doped graphene offers a promising route to low-cost and substrate-independent Pt-free CEs for DSCs.

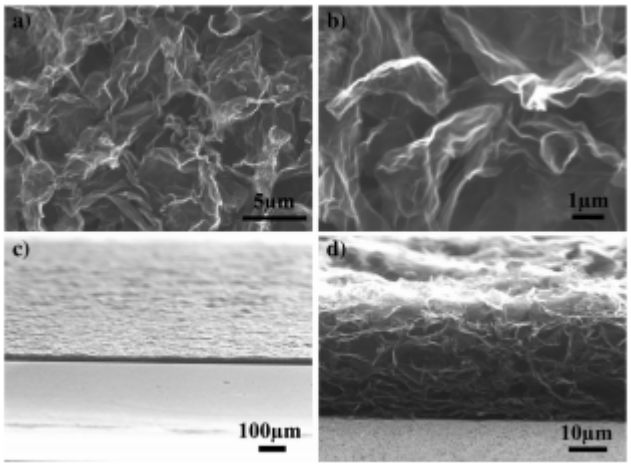

Fig. 17. (a,b) Top-view SEM images and (c,d) side-view SEM images of the prepared N-GF counter electrode at different magnifications.[19]

2.2.2 Carbon-based counter electrode used for other catalysis applications

In addition to using N- doped carbon materials as the CE electrocatalysts towards the redox reaction of tri-iodide/iodide in DSCs, such materials still can be used for catalysis applications in the other reduction reactions, for example, the oxygen reduction in fuel cells or Li-air batteries.

2.2.2.1 N-doped carbon nanotubes

Vertically aligned nitrogen-containing carbon nanotubes (VA-NCNTs) (Fig. 18(A) – Fig. 18(C)) were synthesized by Kuanping Gong et al.[29] These materials

can acts as a metal-free electrode with a much better electrocatalytic activity, long-term operation stability, and tolerance to crossover effect than platinum for oxygen reduction reaction (ORR) in alkaline fuel cells. They observed that the incorporation of electron-accepting nitrogen heteroatoms in the conjugated nanotube carbon plane leads to the relatively high positive charge density on adjacent carbon atoms (Fig. 18(D)). This makes VA-NCNTs provide additional benefits to the metal-free nanotube ORR electrode in achieving superb electrocatalytic performance because they can offer a four-electron pathway for the ORR (Fig. 18(E)). Furthermore, this work clearly demonstrate that the important role of N-doping to ORR can be applied to other carbon materials for the design and development of various other metal-free efficient ORR catalysts for fuel cell applications. These nitrogen-containing carbon nanotube electrodes could even be employed as the new electrocatalytic materials for applications beyond fuel cells such as Li-air batteries.

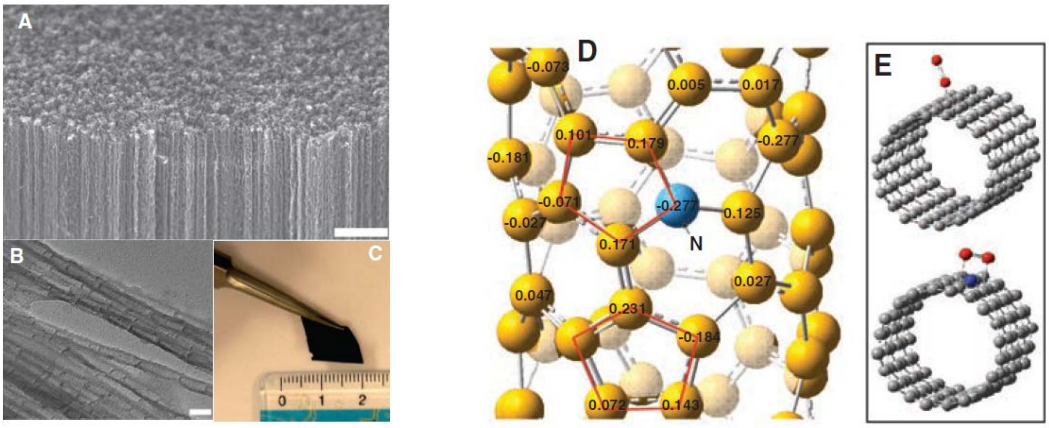

Fig. 18. (A) SEM image of the as-synthesized VA-NCNTs on a quartz substrate. (B) TEM image of the electrochemically purified VANCNTs. (C) Digital photograph of the VANCNT array after having been transferred onto a PS-nonaligned CNT conductive nanocomposite film . Scale bars, 2 μm (A); 50 nm (B). (D) Calculated charge density distribution for the NCNTs. (E) Schematic representations of possible adsorption modes of an oxygen molecule at the CCNTs (top) and NCNTs (bottom).

The C atoms around the pyrrolic-like nitrogen could possess much higher positive charges than do the C atoms around the pyridinic-like nitrogen.[29]

2.2.2.2 N-doped graphene

Liangti Qu et al.[48] used N-doped graphene films (Fig. 19.) that have been developed from a facile CVD approach as the efficient metal-free electrocatalysts for ORR in fuel cells. Compared to the reported metal-free graphene catalysts, the N-doped graphene film shows superb performance for ORR associated with alkaline fuel cells. The observation of long-term stability, tolerance to crossover, and poison effect improves the cathode performance when using N-doped graphene films. In addition, the similar remarkable electrocatalytic properties for ORR to nitrogen-containing vertically aligned carbon nanotubes were also observed in N-doped graphene films. This progress will likely lead to extensive application of N-doped graphene for the development of metal-free efficient ORR electrocatalysts for application beyond fuel cells.

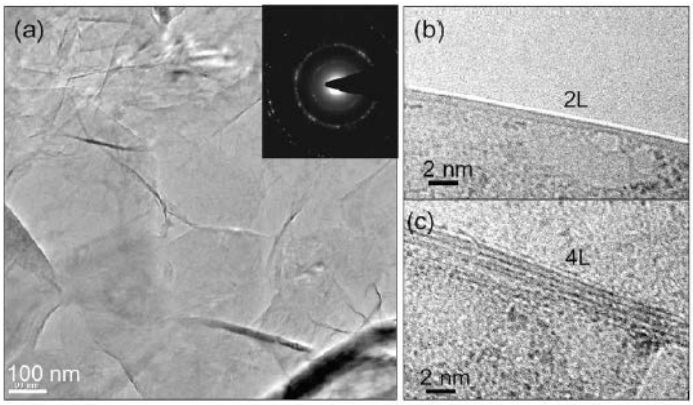

Fig. 19. TEM of the N-graphene films. (a) Low-magnification TEM image showing a few layers of the CVD grown N-graphene film on a grid. Inset shows the corresponding electron diffraction pattern. (b-c) High magnification TEM images showing edges of the N-graphene film regions consisting of (b) 2, (c) 4.[48]

The application of N-doped graphene for the development of metal-free efficient ORR electrocatalysts in nonaqueous Li-O_2 battery cathode was demonstrated

by Gang Wu et al.[31] They have successfully prepared nitrogen-doped graphene-rich composite catalysts from a graphitization process of a heteroatom polymer (polyaniline, PANI) under the catalysis of the cobalt species, using multiwalled carbon nanotubes (MWNTs) as a supporting template (Fig. 20. – Fig. 21.). These novel materials with the addition of Co species exhibit the significant improvement of ORR performance. The nitrogen-doped graphene-rich composite catalysts show much better ORR activity mainly due to their much high mass including electron transports, high specific interactions between active site and CNTs, and high corrosion resistance. The Co species are indispensable for achieving high activity, due to its effects on the final catalyst morphology and structure, including surface area, nitrogen doping, and graphene formation. Compared to the reported metal-free graphene electrocatalysts, a high level of quaternary and pyridinic N (Fig. 22.) was found which may be concomitant with much improved electrocatalytic activity for ORR. Promotional roles in ORR improvements were also found owing to the unique properties of the MWNTs acting as a support. This study clarifies the key issue that the established synthesis-structure-activity correlations provide new insight into further optimization of chemical and physical properties in the graphene nanocomposites, offering the control of morphology and nitrogen functionality with enhanced ORR catalytic activity for applications in nonaqueous Li-O_2 battery cathode electrocatalysts.

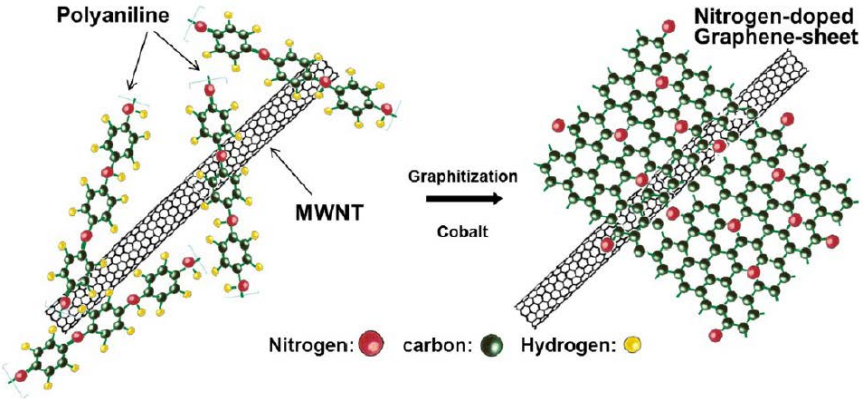

Fig. 20. Scheme of the formation for nitrogen-doped graphene sheets derived from polyaniline and Co precursors using MWNTs as a template.[31]

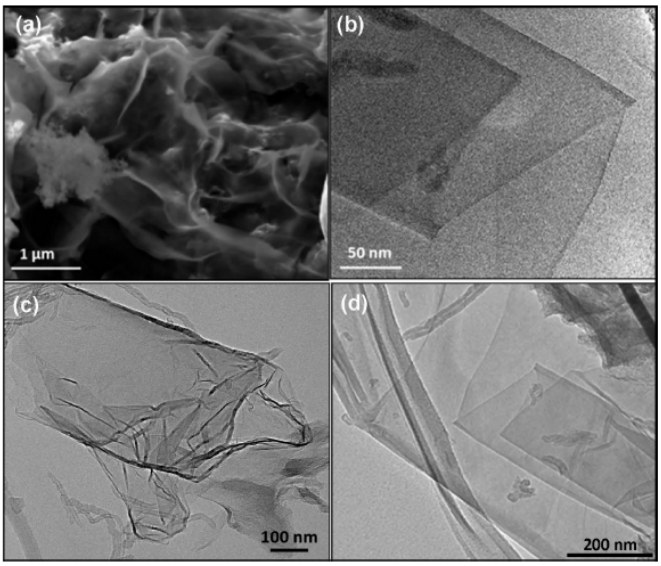

Fig. 21. SEM (a) and HR-TEM (b - d) images of the graphene-rich nanocomposites observed in Co-N-MWNT catalysts.[31]

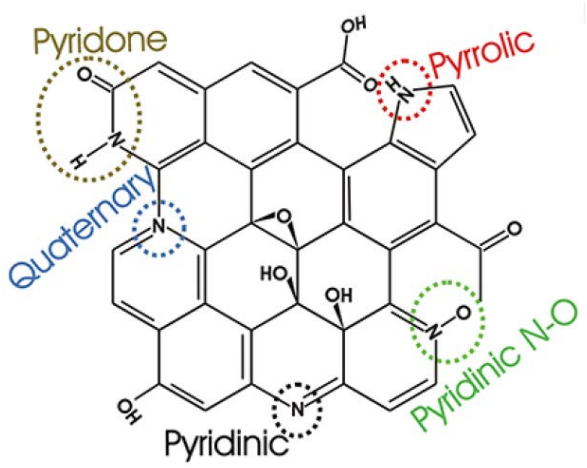

Fig. 22. Schematic representation of the different N-based functional groups detected on the N-doped graphene by XPS.

2.2.2.3 N-doped mesoporous carbon

Since there are micropores embedded in the mesopore walls in the structure of mesoporous carbons, this makes the mesoporous carbons have the unique structural feature because they appear to contain more easily accessible active sites to reactant molecules than those of the conventional microporous carbons. The more efficient activation processes with a homogeneous distribution of functionalized sites are typically observed when applying mesoporous carbons as the electrocatalysts. In addition, the other important properties of mesoporous carbons are high surface area and uniform pore size facilitating the access of reactants to the active sites and allowing a good reactant flux.[61] Therefore, the synthesis of the ordered mesoporous carbons showing high activity and stable stability toward ORR was reported by Xiqing Wang et al.[28] This finding would have a considerable impact to other applications beyond fuel cells.

Although N-doping on carbon materials is normally carried out by the heat treatment under gaseous nitrogen, ammonia, or hydrogen cyanide atmosphere, the possible control of nitrogen content in carbon materials could still not be done. In this regard, it will be a significant advancement if the quantity of nitrogen in the carbon

materials can be controlled. As previous described, Gang Wu et al.[31] have chosen the polyaniline (PANI) as a precursor for making the N-doped carbon material owing to its high N/C atomic ratio (0.167) and high molar weight, which prevents its vaporization at high temperatures.

According to the advantages of using polyaniline as a nitrogen precursor for synthesizing the N-doped carbon materials, Rafael Silva et al.[32] have prepared alternative nonmetal ORR electrocatalysts, N-doped mesoporous carbons, via pyrolysis of PANI exhibiting good activities toward ORR. The achieving high density of adsorbed oxygen in the mesopores of the metal-free N-doped mesoporous carbons with unprecedented high electrocatalytic activity was attributed to the effect of the N species that were present as a dopant on the materials and were formed during pyrolysis. The authors expect that these materials can urge the development of advanced Pt-free catalytic materials to meet the requirements of ORR catalysts toward wide applications of PEMFCs.

The outcome of literature review shows a high potential to use N-doped mesoporous carbons immobilized by Ni or Co with high N content and large specific active surface area as the economical CE electrocatalysts for DSCs. However, the systematic study of employing N-doped mesoporous carbons immobilized by Ni or Co as the electrocatalysts at the CE for I_3^- reduction in DSCs is not yet performed. In this proposal, the aim is to design a superior catalyst through in situ synthesis by combining high electrical conductivity and catalytic activity into one material: N-doped mesoporous carbons immobilized by Ni or Co, in which the nitrogen and oxygen as well as Ni or Co dopants serve as the electrocatalyst and mesoporous carbon serves as an electron collector. As previously described, polyaniline (PANI) has high N/C atomic ratio (0.167) and high molar weight preventing its vaporization at high temperatures. Therefore, polyaniline (PANI) is chosen as a nitrogen precursor

for making the N-doped mesoporous carbons. Mesoporous silica (SBA-15) is chosen as a oxygen precursor because it contains oxygen atoms as the constituent and it is also used as a mesoporous template. We hope that the obtained N- and O-doped mesoporous carbons immobilized by Ni or Co would show not only high surface area but also high N content due to the impeding small CN species vaporized during the pyrolyzing PANI precursor within the thermally robust nanosized cavities of SBA-15 used as a mesoporous template. This electrocatalyst could demonstrate the higher electrocatalytic activity and long-term stability. The outcome of this electrocatalyst will be a significant and interested step forward to electrocatalysis applications in the other electrochemical reduction processes, for example, oxygen reduction reaction in Li-air batteries or hydrogen evolution for producing hydrogen gas used as a starting material in fuel cell. As previously described, the proposed electrocatalyst would be extremely valuable for the applications in energy conversion and storage.

2.3 Objective

(i) To develop highly active and stable N-doped mesoporous carbon-based immobilized by Ni or Co electrocatalysts using polyaniline (PANI) and mesoporous silica (SBA-15) as the nitrogen and oxygen precursors, respectively, to facilitate tri-iodide reduction.

(ii) To optimize the active reaction sites for tri-iodide reduction as a function of surface nitrogen, the contents of nitrogen, oxygen, Ni, and Co, and porosities.

(iii) To determine catalyst stability under long-term performance studies.

2.4 Research methodology

2.4.1 Reagents and Materials. Poly(ethylene glycol)-*block*-poly(propylene glycol)-*block*-poly(ethylene glycol) ((PEG)20(PPG)70(PEG)20) (Pluronic® 123), average molecular weight of 5800 Da, was obtained from BASF. Tetraethyl orthosilicate (TEOS), sodium persulfate, aniline, nickel(II) nitrate ($Ni(NO_3)_2$), cobalt(II) nitrate ($Co(NO_3)_2$), hexane, and hexamethyldisilazane (HMDS). Hydrochloric acid solution and absolute ethanol (99.99%) were obtained from Fischer Scientific. *N*-(2-aminoethyl)-3-aminopropyltrimethoxysilane was acquired from Gelest, Inc.

2.4.2 Synthesis of SBA-15 Mesoporous Silica Functionalized with Organodiamine Groups (SBA-15/Diamine). SBA-15 was synthesized as reported previously.1,2 Pluronic® 123 (4 g) was dissolved in a solution of HCl (20 mL) and distilled water (130 mL). After the temperature of the solution was adjusted to 45 °C, TEOS (8.5 g) was added in it. The solution was vigorously stirred for 20 h, and after which it was kept in an oven at 80 °C for 24 h. The as-prepared mesostructured silica was recovered by filtration, washed copiously with distilled water, and then dried under ambient conditions. Prior to template extraction, the external surface of the as-prepared mesostructured silica was modified with -SiMe3 groups by stirring 4 g of the material in HMDS/toluene (5 mL/60 mL) solution for 18 h. This helped the external surface silanol groups of the as-prepared mesostructured silica to be coated with trimethylsilyl (-SiMe3) groups. After this, the Pluronic® 123 template was removed by stirring the SiMe3-functionalized mesostructured silica material (0.5 g) in 100 mL of diethyl ether:ethanol (1:1 ratio) solution for 5 h. This yielded SiMe3-capped mesostructured silica (labeled here as Me-SBA-15). Organodiamine (“Diamine”) groups were then grafted onto the inner channel walls of the Me-SBA-15 by stirring Me-SBA-15 (0.1 g) in a solution of *N*-(2-aminoethyl)-3-aminopropyltrimethoxysilane

(1.0 mL) and anhydrous toluene (100 mL) for 18 h at 80 °C. The resulting material was washed with copious amount of ethanol, and dried under ambient conditions, giving a mesoporous material, labeled as “SBA-15/Diamine”, whose external surface is functionalized with -Me groups and whose internal surfaces were functionalized with -alkyldiamine groups.

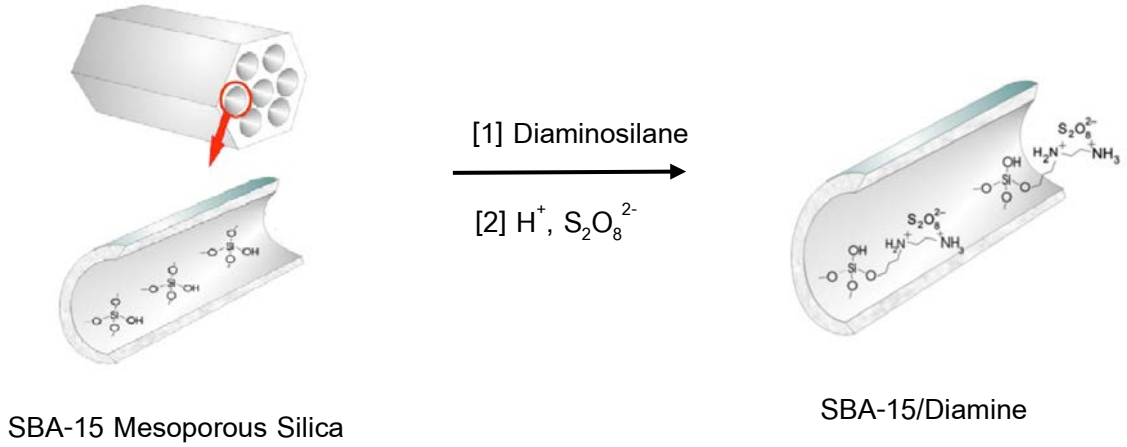

Fig. 23. Schematic illustration of synthesis of SBA-15 mesoporous silica functionalized with organodiamine groups (SBA-15/Diamine)

2.4.3 Synthesis of Polyaniline (PANI) within the Pores of SBA-15 (PANI/SBA-15 Nanocomposite Materials). SBA-15/Diamine (100 mg) was treated with 1 mol/L hydrochloric acid (10 mL) containing sodium persulfate (600 mg). After stirring for 2 h at room temperature, the solid material was recovered from the solution by filtration and washed with distilled water to remove any residual persulfate ions that are not electrostatically immobilized in it. The resulting solid material, denoted as SBA-15/Diammonium-Persulfate, was stirred in a solution containing aniline (150 μL) and 1 mol/L hydrochloric acid (10 mL) in an ice bath (0-5 °C) for 4 h. This led to polymerization of aniline into PANI, as seen by the color changes of the sample from white to green. The solid material was recovered by

filtration and washed copiously with acetone:ethanol (1:1 ratio). It was then treated with 1.0 M ammonia solution (10 mL), filtered, washed several times with distilled water and let to dry under ambient conditions. This gave the material PANI/SBA-15.

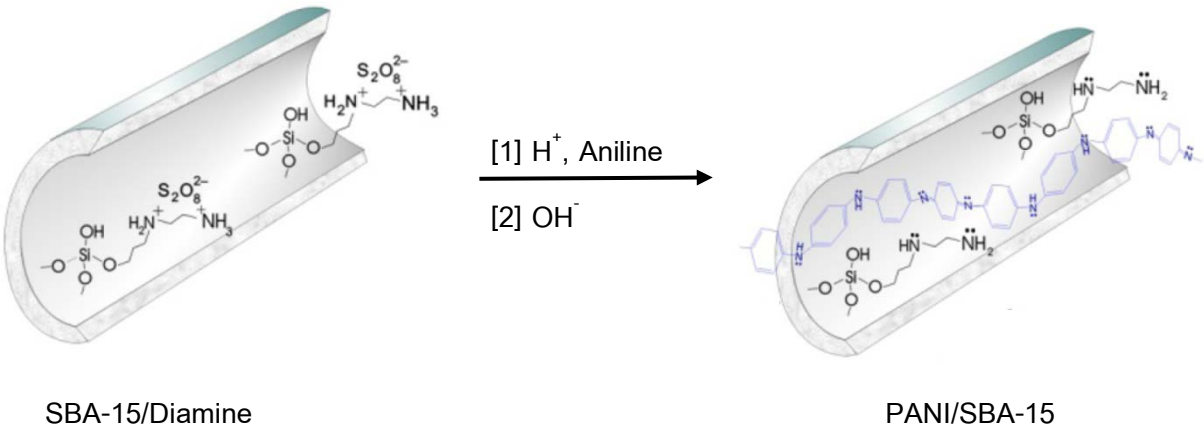

Fig. 24. Schematic illustration of synthesis of polyaniline (PANI) within the pores of SBA-15 (PANI/SBA-15 Nanocomposite Materials)

2.4.4 Metal-Doped PANI/SBA-15. Cobalt(II), Fe(III) or mixed Cobalt(II)/Fe(III) ions were chelated onto PANI/SBA-15 by stirring PANI/SBA-15 (100 mg) in 0.1 mol/L aqueous solutions containing the corresponding metal salts (4 mL). The solution was stirred for 6 h, and after which the solid material was recovered by centrifugation, washed with ethanol, and then dried under ambient conditions.

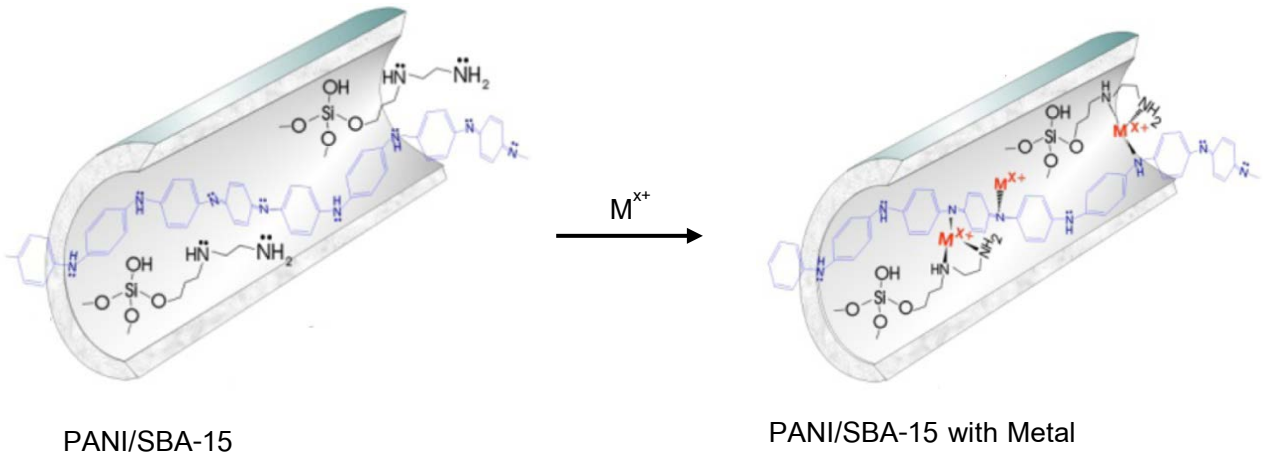

Fig. 25. Schematic illustration of synthesis of Metal-Doped PANI/SBA-15.

2.4.5 Thermal Treatment (Pyrolysis) of PANI/SBA-15 Containing with or without Metals. Pyrolysis the samples was performed by keeping samples in an alumina boat within a temperature-programmable tube furnace under a flow of argon with a flow rate of 30 mL/min. First, the temperature of the furnace was increased at a low rate ramp of 1 °C/min from ambient temperature to reach to two temperature plateaus of 200 and 300 °C. The time span in each plateau was 2 h. After the 300 °C, the temperature was increased once again to the final pyrolysis temperature (600, 700, 800 or 900 °C) with a ramp of 10 °C/min. The temperature is kept at the final pyrolysis temperature for 2 h. The sample was then cooled down to room temperature with a ramp of 10 °C/min.

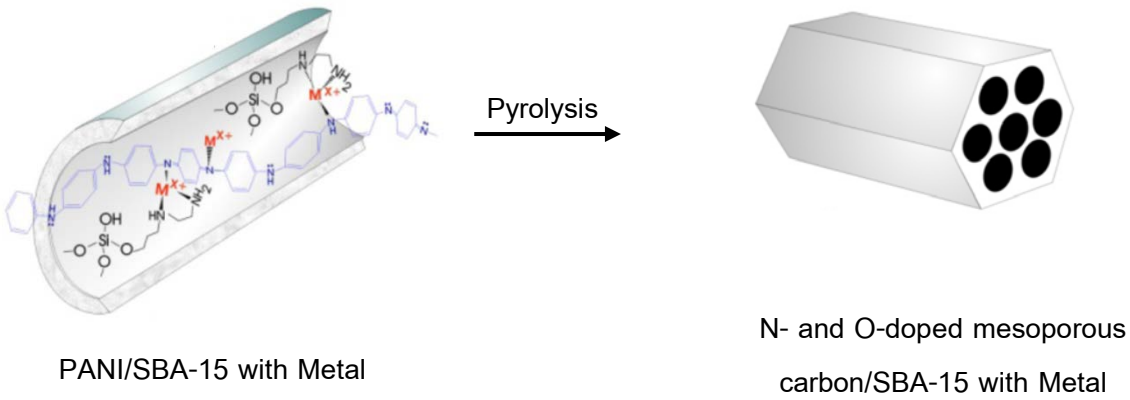

Fig. 26. Schematic illustration of thermal treatment (Pyrolysis) of PANI/SBA-15 with metal.

2.4.6 Etching of Mesoporous Silica. The SBA-15 mesoporous silica template around the resulting carbon-based samples was removed (or dissolved) by stirring the former with 1 mol/L NaOH solution at 100 °C for 2 h. After the pyrolysis, the obtained powder was dispersed in 1 mol/L NaOH solution (~10 μg/mL). The solutions were placed in polypropylene vials and kept in an oven at 100 oC for 4 h to age. After this, the powder was recovered using high speed centrifugation (12000 rpm

– 8064 RCF). The powder was repeatedly washed with distilled water and centrifuged until the Ph of the solution became neutral.

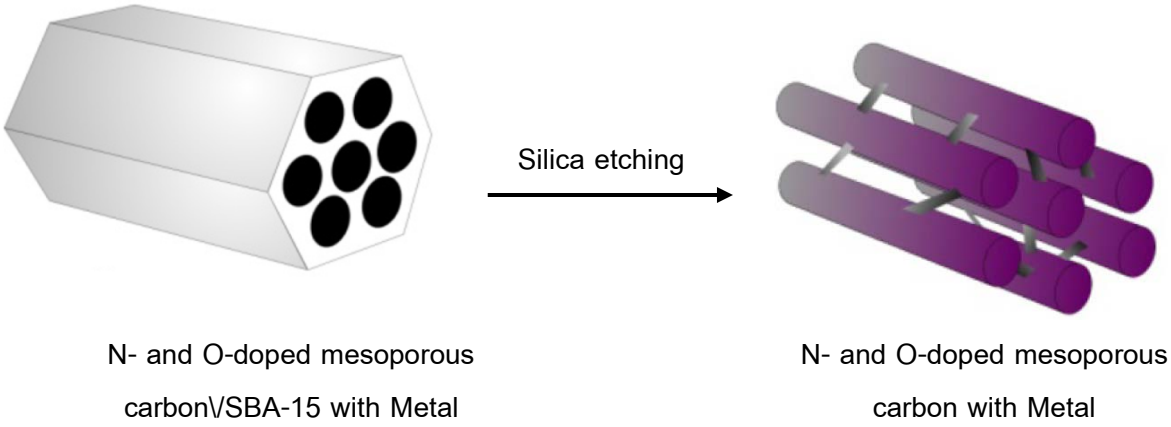

Fig. 27. Schematic illustration of Etching of mesoporous silica

2.4.7 Preparation of N-MC, Co-N-MC, Ni-N-MC, and platinized counter electrodes

To prepare the N-MC, Co-N-MC, or Ni-N-MC CE with a simple doctor-blading method, the paste was firstly prepared as follows: 130 mg of N-MC (or Co-N-MC, Ni-N-MC) sample was ultrasonically mixed with 15 mg of PEG-2000 in 4 mL of water for 30 min and magnetically stirred for 5 h subsequently. Meanwhile, 20 mg of TiO_2 (P25, Degussa) in 2 mL of water was also ultrasonically dispersed for 30 min and magnetically stirred to form the TiO_2 colloid. Then, the prepared TiO_2 colloid was subsequently added to the prepared N-MC (or Co-N-MC, Ni-N-MC) paste and continually stirred for 3 h to form a viscous mixture. Finally, the obtained paste was scraped onto a FTO (fluorine-doped tin oxide) conductive glass by doctor-blading method and then dried at 80 °C overnight, resulting in N-MC (or Co-N-MC, Ni-N-MC) CE. For comparison, the platinized CE was fabricated by deposition of 4 mM

H_2PtCl_6 (2 mg of H_2PtCl_6 in 1 mL of ethanol, 20 μL cm^{-2} of H_2PtCl_6 solution) on the surface of FTO glass and sintering at 400 °C for 30 min.

2.4.8 Preparation of photoanode and cells fabrication

The TiO_2 photoanode was prepared as follows: FTO conductive glass was first cleaned in detergent solution, water, and ethanol using an ultrasonic bath. The FTO substrate was treated with 50 mM aqueous $TiCl_4$ solution at 70 °C for 30 min and washed with water and ethanol. To prepare a colloidal TiO_2 suspension,[62] the titanium isoprpoxide precursor was hydrolyzed in aqueous solution and stirred at 80 °C. After adjusting the pH of the above solution to ~ 2, the resulting mixture was autoclaved at 250 °C for 12 h and solidified by rotary evaporation. The prepared TiO_2 colloidal paste was loaded onto FTO glass by the doctor-blading technique. After sintering at 120 °C for 15 min, the obtained layer was further calcined at 500 °C for 30 min. The TiO_2 film was treated with 50 mM aqueous $TiCl_4$ solution at 70 °C for 30 min, then washed with distilled water, and resintered at 500 °C for 30 min. After cooling to 80 °C, A layer of TiO_2 electrode was immersed in a 3×10^{-4} M N719 dye (Solaronix SA, Switzerland) ethanol solution and kept at room temperature for 24 h. Finally, the dye adsorbed TiO_2 film was cleaned with ethanol and dried. Two kinds of electrolyte solutions were used in this research. The triodide/iodide redox couple was prepared with 0.05 M I_2, 0.5 M LiI, 0.3 M 1,2-dimethyl-3-propylimidazoliumiodide (DMPII), and 0.5 M 4-*tert*-butyl pyridine, in acetonitrile. Another electrolyte solution was 5-mercapto-1-methyltetrazole di-5-(1-methyltetrazole) disulfide/N-tetramethylammonium salt ($NMe_4^+T^-$) (T_2/T^-, Figure S1) which was prepared as reported procedure[63]). The T_2/T^- electrolyte was composed of 0.4 M 5-mercapto-1-methyltetrazole N-tetramethylammonium salt ($NMe_4^+T^-$), 0.4 M di-5-(1-methyltetrazole) disulfide (T_2), 0.05 M $LiClO_4$, and 0.5 M 4-tert-butylpyridine (TBP) in acetonitrile/ethylene carbonate (6:4 volume ratio). A DSC was fabricated by a

photoanode, a counter electrode in a sandwich-type cell using a thermal adhesive film (60 μm thick Solaronix, Switzerland) as an electrolyte storage spacer. The active area for the *J–V* measurement was 0.20 cm^2.

2.4.9 Measurements

The X-ray diffraction (XRD) measurements were carried out with an X-ray diffractometer (Bruker D8 ADVANCE). The images of surface morphologies and the energy-dispersive spectrometry (EDS) spectra were acquired by scanning electron microscope (SEM) with JEOL JSM-5600LV and transmission electron microscope (TEM) with JEOL JEM-2011 F operated at 200 kV. The metal content in each sample was determined by atomic absorption spectroscopy (AAS; Varian Model AA280FS). The Raman spectra were measured by a confocal Raman microscope (Bruker Optics, 532 nm argon ion laser). Surface area and pore characteristics were measured by recording N_2 adsorption and desorption isotherms at 77 K using a Quantachrome® ASiQwin Automated Gas Sorption Autosorb Analyzer. Specific surface areas of the samples were calculated from nitrogen adsorption data in the relative pressure range from 0.05 to 0.2 using Brunauer–Emmett–Teller (BET) equation. Total pore volumes were analyzed from the amount of gas adsorbed at the relative pressure of 0.99. Pore-size distribution (PSD) was determined from adsorption branches by Barrett–Joyner–Halenda (BJH) method. The elemental composition and their bonding properties were determined by an X-ray photoelectron spectroscopy using synchrotron radiation from beamline no. 3.2 at the Synchrotron Light Research Institute, Thailand. Cyclic voltammetry (CV) was performed with a three-electrode system to study the electrocatalytic ability of the CEs. The scanning potential range was from −0.4 to 0.7 V at a scan rate of 50 mV s^{-1} by using potentiostat *(Metrohm* Autolab). A Pt served as a counter electrode and Ag/AgCl electrode served as a reference electrode. The electrolyte solution contained 0.1 M I_2, 0.1 M LiI, 0.6 M tetrabutylammonium iodide,

and 0.5 M 4-tertbutylpyridine (TBP) in an argon-purged acetonitrile. Electrochemical impedance spectroscopy (EIS) experiments were conducted with a traditional CE symmetrical cell by using Autolab Potentiostat PGSTAT 302 with FRA module. The measured frequency was in the range of 100 mHz to 1 MHz, and the AC amplitude was set at 10 mV. The bias was 0 V. Photovoltaic performance of the DSCs was measured with simulated AM 1.5 illumination from the Xenon arc lamp (100 mW cm^{-2}) with a Keithley 236 source-measure unit. A black mask was applied on the surface of DSCs to avoid stray light, and all solar cell tests were performed at room temperature.

3. Results and Discussion

3.1 Material Characterization

Figure 28 presents the XRD patterns of the prepared Co-N-MC and Ni-N-MC nanocomposites. In the XRD pattern of Co-N-MC composite (Figure 28 (a)), the three sharp diffraction peaks (circle label) can be indexed to the well-crystallized Co (JCPDS 15-0806), and other three obvious diffraction peaks (square label) identify that CoO (JCPDS 74-2392) is also present in the Co-N-MC composite. For Ni-N-MC composite, the intensity diffraction peaks at 2θ values of about 37.2, 43.3, and 62.8° in the XRD pattern (Figure 28(b)) are attributed to crystalline NiO (JCPDS 65-6920). Besides NiO, the other peak positions presented in the XRD pattern of Ni-N-MC composite can be indexed to those of $Ni(OH)_2$ (JCPDS 02-1112) and Ni (JCPDS 04-0850). Therefore, we can say that Co or Ni compounds imbedded in N-doped mesoporous carbons have been successfully synthesized. The average Co and NiO particle sizes are estimated using the Scherrer equation $d = 0.89\lambda/\beta \cdot \cos\theta$, where d is the average crystallite size of the Co and NiO, λ is the X-ray wavelength (Cu Kα, λ= 0.154 nm), β is the half-peak width for Co and NiO peaks in radians, and θ is the diffraction angle of Co (2θ = 44.2°) and NiO (2θ = 43.3°) peaks. The calculated

average crystallite sizes of Co and NiO are 56.0 and 54.9 nm for Co-N-MC and Ni-N-MC, respectively. The structure and particle dispersion of the samples were further investigated by TEM analysis.

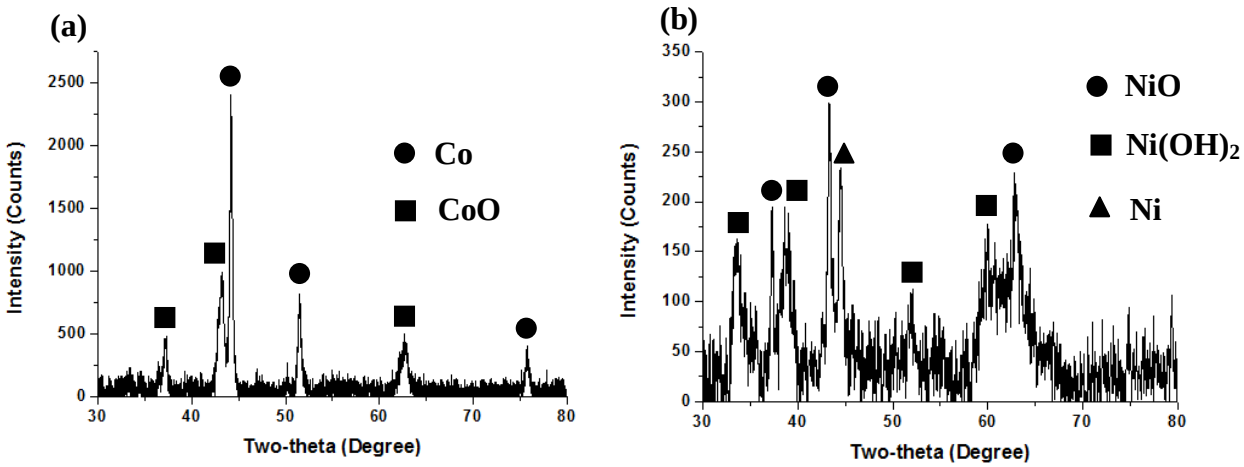

Fig. 28. XRD patterns of the N-doped mesoporous carbon imbedded with (a) Co species and (b) Ni species.

The crystallite structure of the carbons was characterized by XRD. The diffraction peak at $2\theta \approx 27°$ observed in the XRD patterns of all samples corresponds to the (002) diffraction of crystalline carbon as displayed in Figure 29. Although the culminating points of diffraction peak (002) related to graphitic carbon are similar for all samples, the shape of diffraction peaks (002) becomes sharper along with the addition of Co or Ni species. Then, the addition of Co or Ni species in N-doped mesoporous carbon is proved to cause an improved graphitic crystallinity. Moreover, it is also known that the (002) diffraction of the graphite structure is centered at 2θ of 26° and its interlayer spacing ($d_{(002)}$) is 0.336 nm. In our results, the interlayer spacing ($d_{(002)}$) of both Co-N-MC and Ni-N-MC was calculated to be 0.334 nm which was similar to that of graphite. This indicates a highly graphitic crystallinity resulting in excellent electrical conductivity. Consequently, the graphitic carbon structure in both synthesized nanocomposites might be theoretically beneficial for CE electrocatalysts in DSCs.

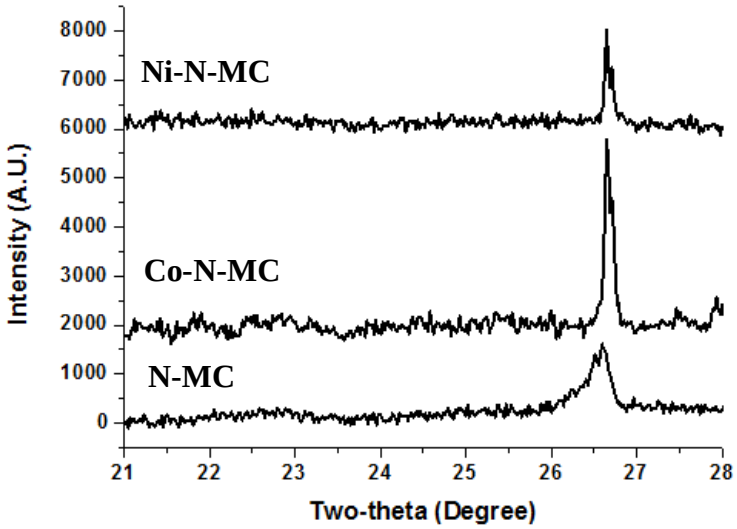

Fig. 29. XRD patterns of the N-doped mesoporous carbon, Co species, and Ni species imbedded in N-doped mesoporous carbons.

The microstructures of the Co-N-MC and Ni-N-MC electrocatalysts were examined by scanning electron microscopy (SEM) and transmission electron microscopy (TEM). The SEM images in Figure 30(b) – Figure 30(c) show that the microstructure of mesoporous carbons has the linear array of connected rod-like particles with a diameter of 30 - 70 nm and 500 – 750 nm long. This observation indicates that mesoporous carbon has been successfully synthesized because the obtained nanocomposites have similar geometric morphology to the original SBA-15 used as a template (Figure 30(a)).

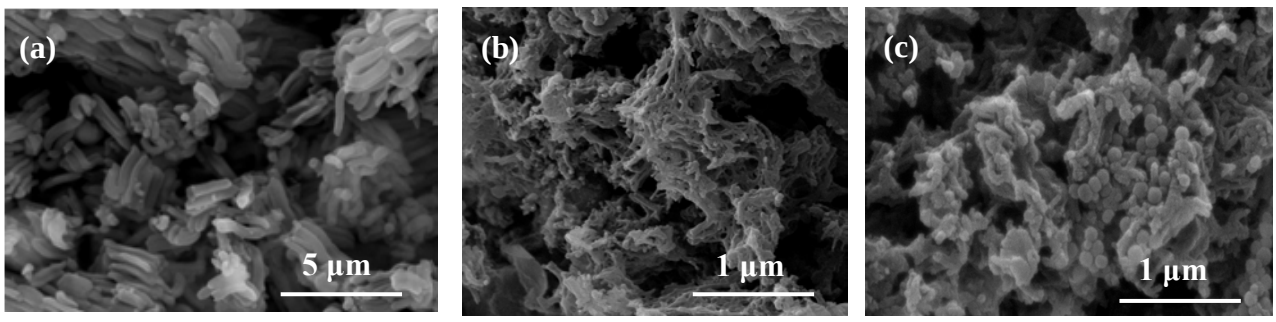

Fig. 30. Surface morphology of (a) SBA-15, (b) Co-N-MC, and (c) Ni-N-MC.

Figure 31. shows the energy-dispersive X-ray spectroscopy (EDX) analysis of Co-N-MC and Ni-N-MC, disclosing the existence of Co and Ni, respectively in the nanocomposites.

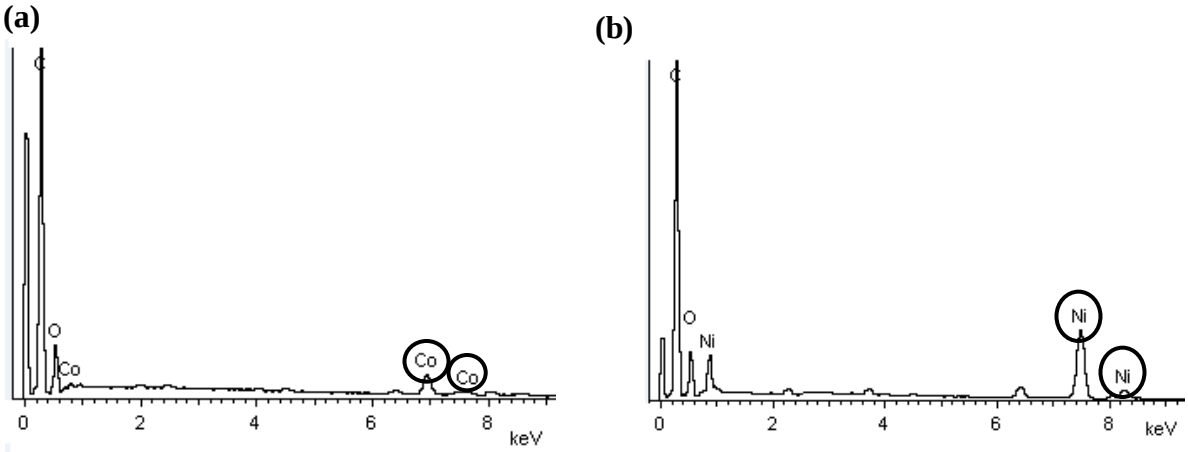

Figure 31. EDX analysis of (a) Co-N-MC and (b) Ni-N-MC.

Values of the Co and Ni contents of each sample were determined using atomic absorption spectrophotometry (AAS), after acid digestion of the samples. The synthesized Co-N-MC contained 3.28 mmol/g of Co (19.30 Wt.%) and the Ni-N-MC contained 5.66 mmol/g of Ni (33.27 Wt.%).

The TEM images in Figure 5 show that these nanocomposites are comprised of randomly oriented fibers retaining well rod-like morphology of the SBA-15 template. This observation is in good agreement with the corresponding SEM images. Furthermore, the TEM images of the metal-N-MC (Figure 32(b) – Figure 32(c)) also display the homogeneous distribution of Co or Ni-based nanoparticles with average particle size of ca. 50 nm throughout the frameworks of N-MC, confirming the formation of Co and Ni species imbedded in N-MC supports. The particle sizes of the metal compounds obtained from TEM images are consistent with the values calculated from the Scherrer equation. The observation from TEM measurement also suggests that the particles with small sizes of metal compounds uniformly decorated onto the mesoporous carbon support can be attributed to effective confinement of

mesoporous carbon structure towards growth process for particles of metal compounds. Moreover, it has been demonstrated by many studies that N species doped in carbon materials will act as localized defects which can provide initial nucleation sites for immobilizing nanoparticles. The presence of N species also helps dispersing particles of metal compounds on carbon support and avoids surface metal aggregation, thus achieving homogeneous dispersion of nanoperticles with small sizes on mesoporous carbon support.[64, 65] To further provide useful information about the nanoparticles in the composites, HRTEM images are also demonstrated in Figure 32(d) – Figure 32(e). It is obvious in magnifying images that Co and Ni-based compounds possess the well-crystallized structures. The lattice fringes of Co and Ni-based compounds with measured interplanar spacings of 0.20 nm (Figure 32(d)) and 0.21 nm (Figure 5(e)) are clearly observed, corresponding to the interplanar distances of cubic crystal metallic cobalt (111) facet and cubic crystal nickel oxide (200) facet, respectively. This can confirm the results analyzed by XRD. In addition, the well-defined crystalline lattice spacing between carbon layers is also measured to be 0.33 nm for both samples, which matches well with the (002) plane of the typical graphite phase. This phenomenon indicates that the degree of graphitization can be improved by Co or Ni-based nanoparticles which can be confirmed by XRD results.

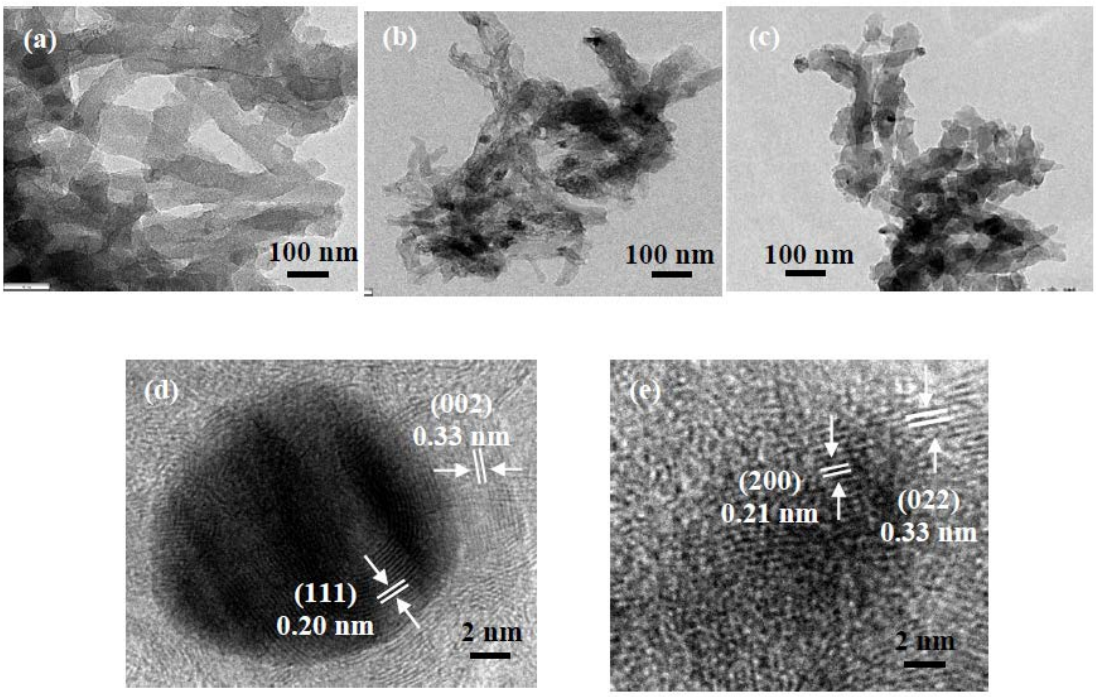

Figure 32. TEM images of (a) N-MC, (b) Co-N-MC, (c) Ni-N-MC and HRTEM images of (d) Co-N-MC, (d) Ni-N-MC samples.

Raman measurement was conducted to identify carbon phases and structural defects. In first order Raman spectra for N-MC, Co-N-MC, and Ni-N-MC (shown in Figure 33), there are two peaks apparent in the spectra for all three samples, corresponding to the D- and G- bands at the vibration of 1355 cm^{-1} and 1580 cm^{-1}, respectively. The D band clearly demonstrates the existence of disorders or vibrational of sp^3 hybridized carbon atoms in the carbon materials.[66] The G band is associated with sp^2 hybridized carbon atoms (graphitic sheet) presenting in all carbon materials which arises from the E_{2g} vibrational mode. The relative area under the peak for the D band and G band, I_D/I_G value, is determined to be proportional to the ratio of defect sites to graphitic structure of carbon materials. The decrease of I_D/I_G value is indicative of improving degree of graphitization.[67, 68] As shown in Figure 33, I_D/I_G values were estimated at 1.56 for N-MC, 1.43 for Co-N-MC, and 1.09 for Ni-N-MC which were decreased monotonically along with the incorporation of Co and Ni

species. This suggests that the graphitization degree of carbon samples can be enhanced with the addition of Co and Ni species because the metal dopants have catalytically graphitized the partly amorphous carbon during thermal treatment. This leads to a better graphitic crystallinity and electron conductivity of carbon composites. This result is in good agreement with those from XRD and HRTEM data.

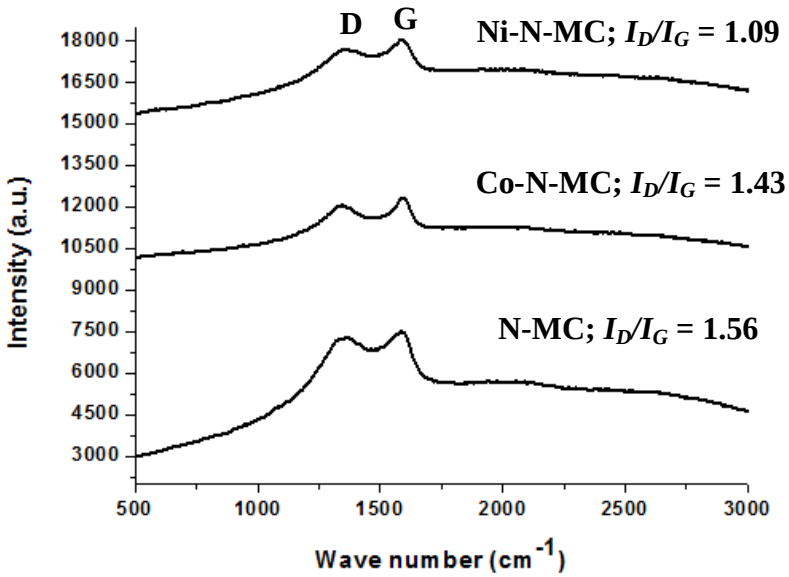

Figure 33. Raman spectra of N-MC, Co-N-MC, and Ni-N-MC samples.

The surface area, pore volume and mean pore size for the N-MC, Co-N-MC, and Ni-N-MC measured by nitrogen porosimetry are shown in Table 1. The surface areas for Co-N-MC and Ni-N-MC are 101 and 218 m^2/g, respectively, which are significantly higher than that of N-MC (35 m^2/g). The nitrogen adsorption-desorption isotherms of all samples shown in Figure 34. exhibit type IV isotherms, with distinct hysteresis loop at the relative pressure (P/P_0) range of 0.40 to 0.70, which is due to the capillary condensation of nitrogen in the mesoporous texture.[69, 70] The mesopore size distribution was centered at 3.8 nm for Co-N-MC and Ni-N-MC, respectively, according to the Barrett–Joyer–Halenda (BJH) model (insets in Figure 34(a) – Figure 34(b)), exhibiting narrow pore-size distribution. The pore-size distribution curve of N-MC, however, showed a broad pore size distribution which was centered at 6.5 and

9.5 nm (inset in Figure 34(a)). As concluded in Table 1, the N-MC obtained the smallest structure parameter, suggesting a greater shrinkage during the heat treatment. Nevertheless, the total pore volumes of the Co-N-MC (0.30 cm^2/g) and Ni-N-OMC (0.48 cm^2/g) are larger than that of N-MC (0.23 cm^2/g), which indicates that Co and Ni species can mechanically strengthen framework and decrease contraction during carbonization.

Table 1. Properties of Mesoporous Carbon

Carbon	Surface area (m^2/g)	Pore volume (cm^2/g)	Pore size (nm)
N-MC	35	0.23	3.8
Co-N-MC	101	0.30	3.8
Ni-N-MC	218	0.48	6.5

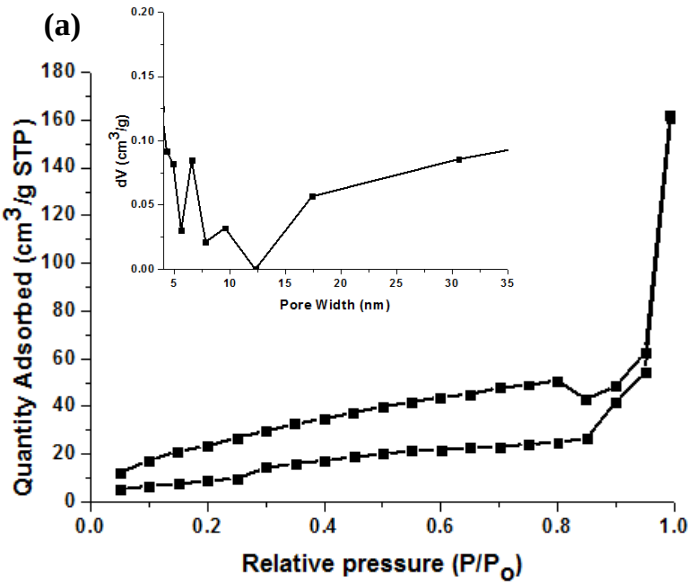

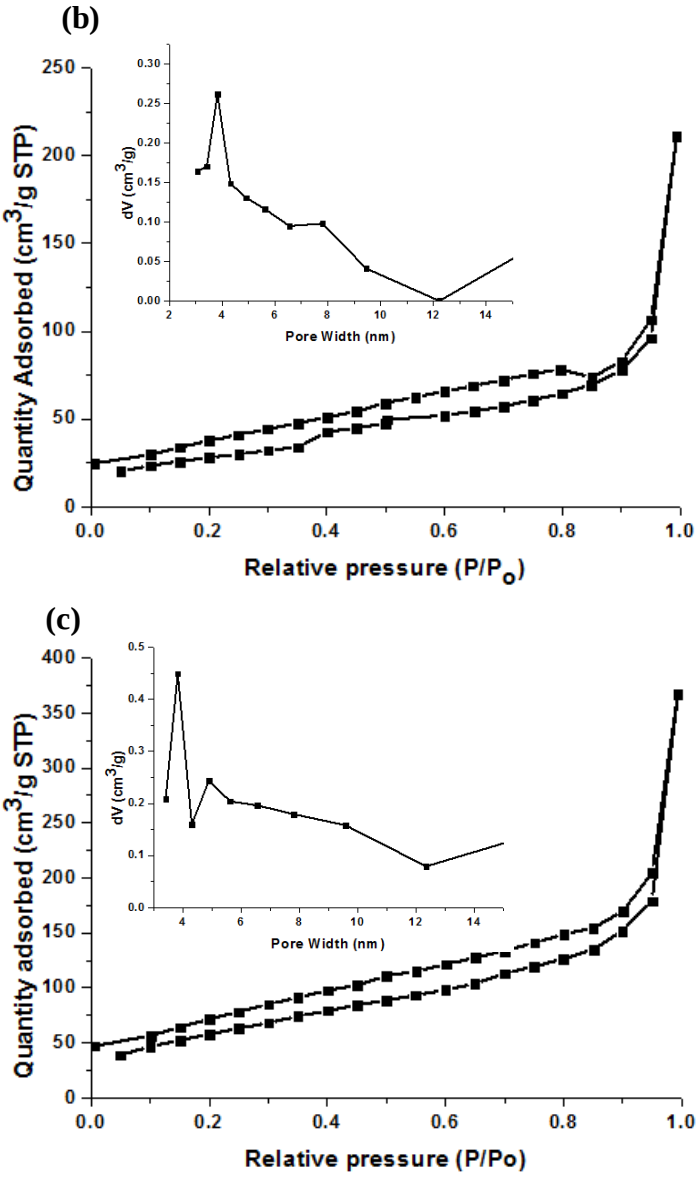

Figure 34. Nitrogen (77 K) adsorption−desorption isotherms of (a) N-MC, (b) Co-N-MC, and (c) Ni-N-MC samples (insets show the pore size distribution of the N-MC , Co-N-MC, and Ni-N-MC samples).

X-ray photoelectron spectroscopy (XPS) analyses were used to investigate and compare the surface electron states properties of carbon, nitrogen, cobalt, and nickel species in materials. The HR C 1s XPS spectra are depicted in Figure 35(a). C 1s spectra of three samples presented in Figure 35(a) can be deconvoluted to several single peaks corresponding to C-C=C (284.3 eV; labeled as I)[71], C-O/C-N (286.0 eV; labeled as II), and C=O (286.9 eV; labeled as III), indicating the existence of

heteroatoms in composites.[72] The atomic percentage ratios of C-C=C/C-O, C=O in the N-MC, Co-N-MC, and Ni-N-MC samples determined from the peak area of C 1s are founded to be 1.40, 1.61, and 2.53, respectively (Figure 35(b)). The C-C=C contents in Co-N-MC and Ni-N-MC composites are much higher than that in bared N-MC sample, which is attributed to the efficiency of transition metal towards carbonization process. The content of C-C=C increases upon the addition of Co or Ni species in carbon framework implying the improvement of electronic conductivity and fast electron transfer throughout the structural framework.

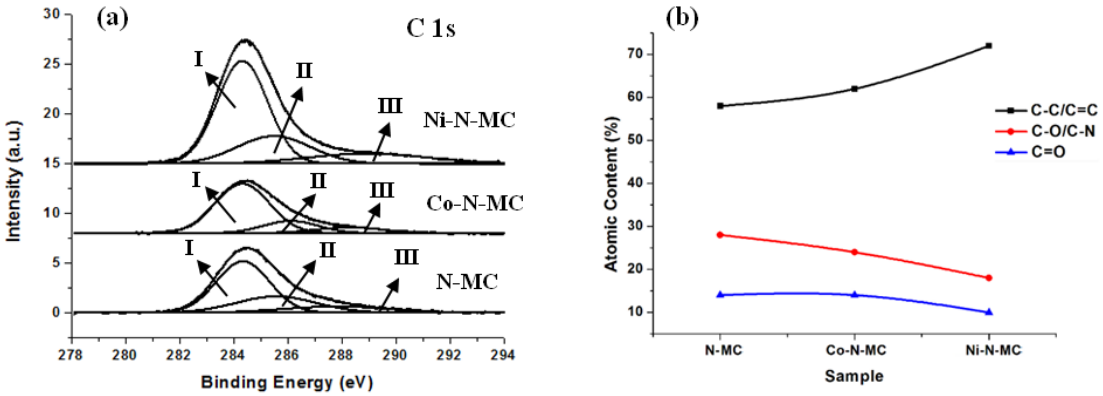

Figure 35. (a) XPS C 1s spectrum of N-MC, Co-N-MC and Ni-N-MC and (b) Atomic %C of each sample determined by XPS.

The binding energy peaks observed in the HR N 1s spectra shown in Figure 36(b) can be fitted into three peaks at 398.3, 400.1, and 401.2 eV, which are attributed to the pyridine-like nitrogen atoms[73], pyrrolic-like nitrogen atoms[74, 75], and graphitic nitrogen atoms[76], respectively (Figure 36(a)). This suggests that nitrogen was successfully doped into carbon framework. In addition, the total concentrations of pyridinic and graphitic N determined based on the integrated peak areas are 53%, 63%, and 67% for N-MC, Co-N-MC, and Ni-N-MC, respectively (Figure 36(c)). It was previously reported that both pyridinic and graphitic N functionalities may provide effective electrocatalytic active sites.[30, 77] Consequently, the increased

pyridinic and graphitic N contents are expected to improve the electrocatalytic performance towards I_3^- reduction of Co-N-MC and Ni-N-MC.

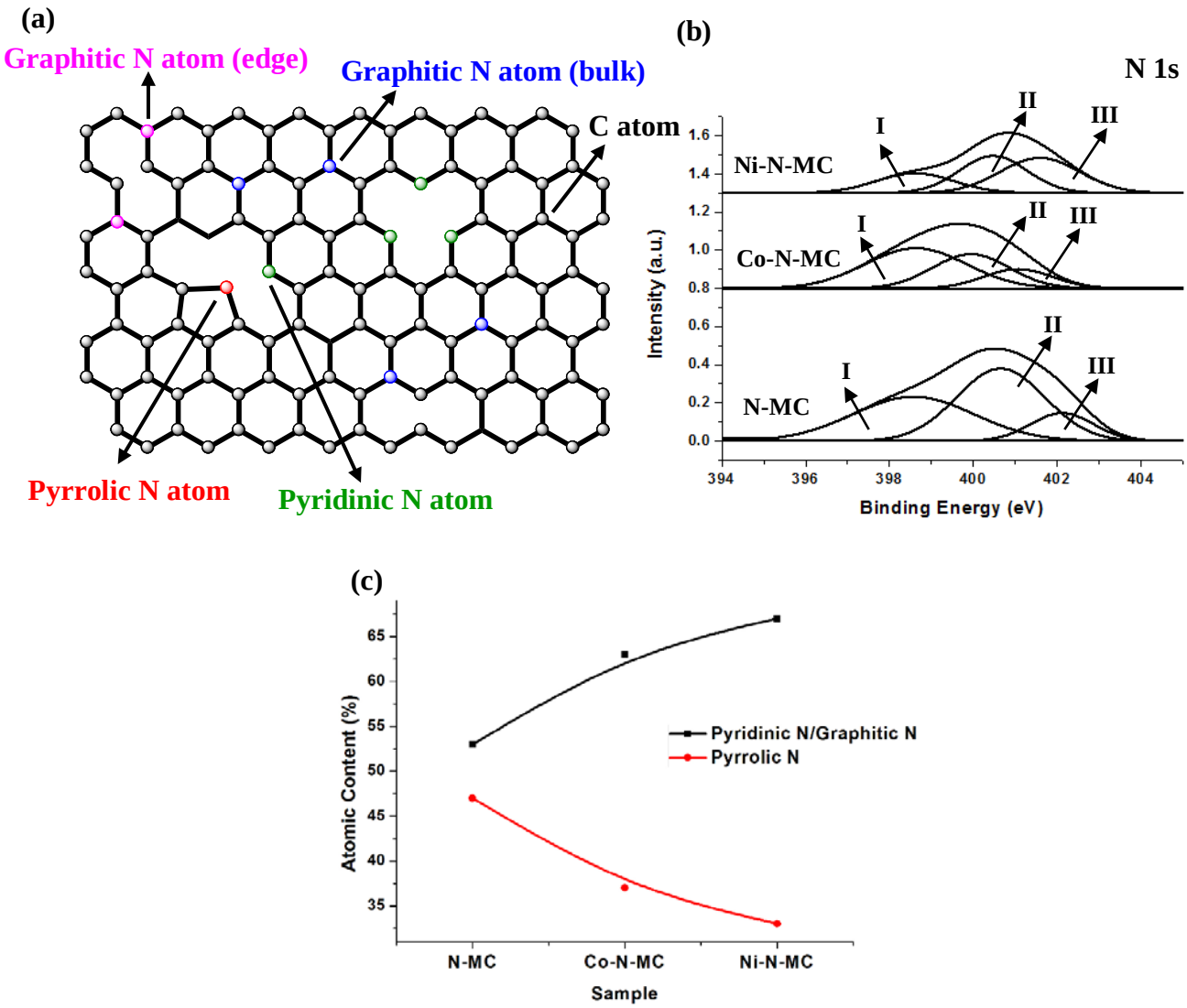

Figure 36. (a) Schematic representation of the different N-based functional groups detected on MC by XPS, (b) XPS N 1s spectrum of N-MC, Co-N-MC and Ni-N-MC, and (c) Atomic %N of each sample determined by XPS.

In addition, the high-magnification XPS spectra in the Co 2p region of Co-N-MC and Ni 2p region of Ni-N-MC are also used to further confirm the composition of the obtained products (Figure 37). The Co $2p_{3/2}$ peaks of Co-N-MC at 778.5 and 779.7 eV (Figure 37(a)) are attributed to Co^0 and Co^{2+}, respectively.[78-80] For Ni-N-MC, the Ni $2p_{3/2}$ region (Figure 37(b)) exhibits a small peak at binding energy of 852.6 eV which can be attributed to Ni^0 while the peak located at 854.0 eV is ascribed

to Ni^{2+}.[81, 82] Therefore, all of the results clearly confirm the formation of Co and CoO in Co-N-MC as well as Ni, NiO, and $Ni(OH)_2$ in Ni-N-MC. These findings agree well with the XRD and HRTEM results.

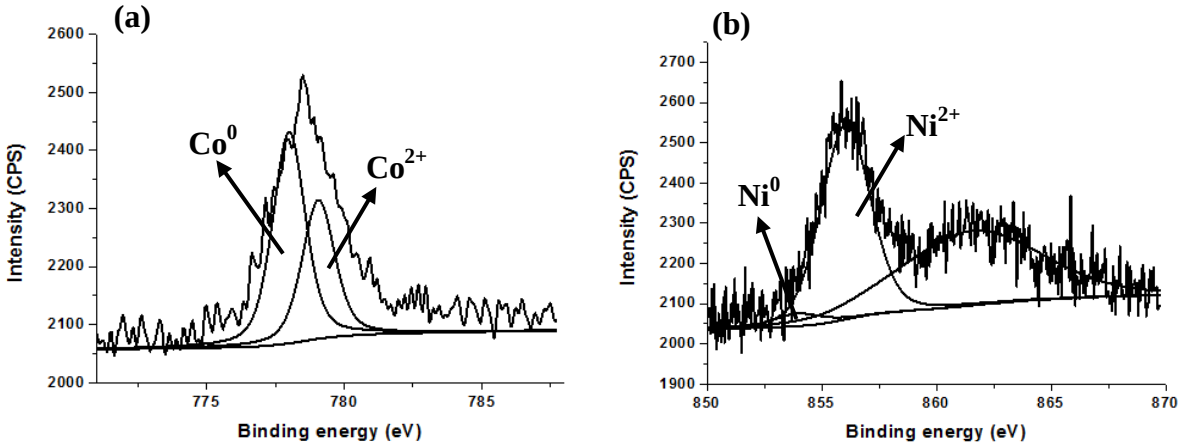

Figure 37. XPS spectra of (a) Co 2p of Co-N-MC and (b) Ni 2p of Ni-N-MC.

3.2 Electrocatalytic Activity Characterization.

The CE is an important component impacting the performance of the DSCs. To regenerate the tri-iodide/iodide redox species with a minimum energy loss, the CE electrocatalyst should be modified to enhance the electrical conductivity, the specific surface area, and the electrocatalytic activity.[83, 84] CV is a powerful tool to understand the electrocatalytic properties for N-doped mesoporous carbon immobilized by Co or Ni species. As shown in Figure 38(a), all electrodes show very well-resolved CV profiles with a pair of current peaks in CVs, exhibiting the electrocatalytic activity for I_3^-/I^- redox couple. The Ni-N-MC and Co-N-MC electrodes show a pair of current peaks similar to the platinized electrode, while N-MC electrode exhibits less intense current peaks. This suggests that the Co and Ni species immobilized on N-doped mesoporous carbons contribute to the electrocatalytic performance of the Co-N-MC and Ni-N-MC electrodes, respectively by providing more exposed active sites for accelerating the I_3^-/I^- redox reaction at the electrode-electrolyte interface.[85, 86] Moreover, the superior electrocatalytic activity of the Co-N-MC and Ni-N-MC

electrodes is also consistent with the efficient charge transport and transfer rates during the electrocatalytic reaction process. These are attributed to both high pyridinic and graphitic N contents to provide sufficient electrocatalytic active sites as well as large surface area to facilitate electrolyte penetration. In comparison with the Ni-N-MC and Co-N-MC electrodes, the N-MC electrode has the smallest current peaks due to the lack of conductive mesoporous carbon matrix resulting in less efficient charge transport.

In addition to the current peak, the peak potential separation (ΔE_p) between the anodic and cathodic peaks is also used to determine the rate of interfacial charge transfer between the electrolyte and the electrode. ΔE_p is inversely proportional to the rate of an electrochemical reaction. As compared with platinized, Ni-N-MC, and Co-N-MC electrodes, the anodic peak of N-MC electrode appears at a relative positive potential (0.450 V vs Ag/Ag^+, the same applies hereinafter), along with the cathodic peak, which appears at a negative potential (-0.029 V) leading to the largest ΔE_p value (Figure 38). This indicates a relatively large charge-transfer resistance implying a low reversibility of the I_3^-/I^- redox reaction when N-MC is used as an electrocatalyst. For the N-doped mesoporous electrodes with imbedding Co or Ni species, the cathodic peaks tend towards positive (0.103 V for Co-N-MC and 0.096 V for Ni-N-MC), whereas the anodic peaks tend towards negative (0.391 V for Co-N-MC and 0.406 V for Ni-N-MC), in contrast with N-MC electrode. This demonstrates that the electrocatalytic performance is improved by immobilizing Co or Ni species into N-MC because of their reversibility. Although the Co-N-MC and Ni-N-MC electrodes have similar current peaks and ΔE_p values to the platinized electrode, the electrocatalytic performance/cost is still higher than that of platinized electrode. In brief, the Co-N-MC and Ni-N-MC nanocomposites are advantageous as the potential

low cost electrocatalysts for CEs in DSCs to replace the conventional and expensive Pt CE.

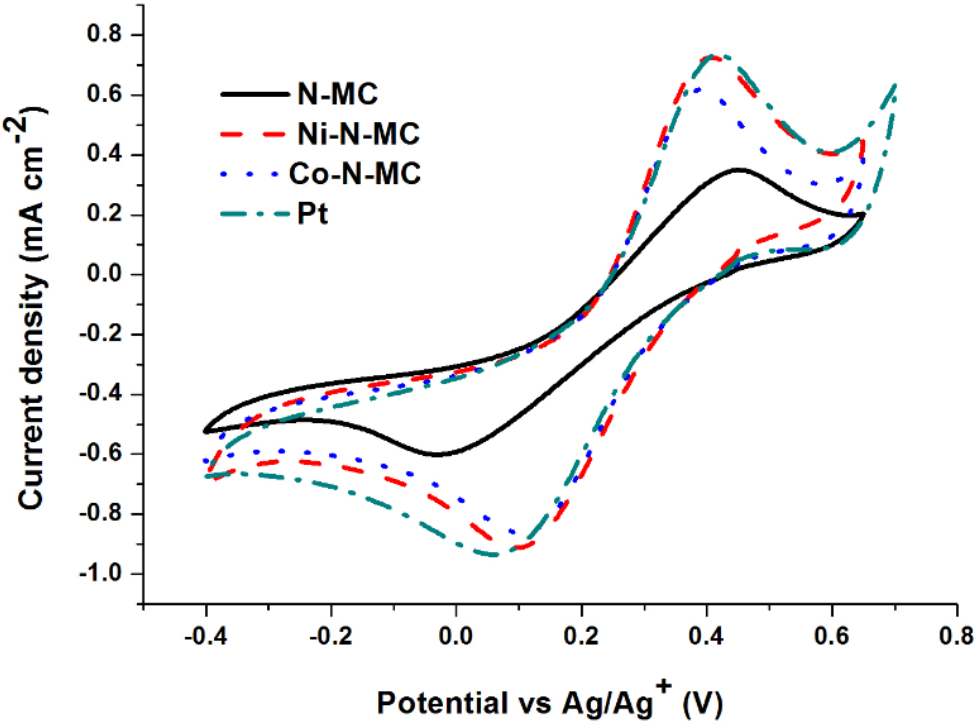

Figure 38. Cyclic voltammograms of the platinized, N-MC, Co-N-MC, and Ni-N-MC electrodes.

Chronoamperometry (CA) is an effective technique for investigating the mass transport of the redox couple in the bulk electrolyte solution and also within the structurally porous electrode as well as thereby for evaluating the electrocatalytic activity of an electrocatalyst. Particularly, it is more serious for mesoporous carbon which generally suffered from limited electrolyte diffusion and penetration through its pore.[87] The mass transport properties of I_3^- in our mesoporous carbon electrodes are more accurately characterized by chronoamperometry (CA) at room temperature (Figure 39). As expected from the semi-infinite Cottrell decay,[88] the observed current dropped linearly as $t^{-1/2}$ (t is time). The diffusion coefficient (D) can be calculated from the transition time (t) obtained by the extrapolation of both linear components of the chronoamperometric plot according to the eqs 1 and 2, where δ is the distance between electrodes.

$$\frac{n\,FAC.\sqrt{D}}{\sqrt{\pi\,t}} = \frac{2n\,FAC.D}{\delta} \quad \ldots(1)$$

$$D = t^{-1}\left(\frac{\delta^2}{4\pi}\right) \quad \ldots(2)$$

From the data in Figure 39 and eq 2, the *D* value can be calculated and was found to be ca. 1.1×10^{-5} cm^2/s (δ = 60 μm) for both all mesoporous carbons and platinized dummy cells in our system. Obviously, the obtained value is a reasonable agreement with values from the literature.[89] The limiting current of the Ni-N-MC was, however, slightly higher than that of platinized electrode. The higher limiting current of Ni-N-MC cell is mainly due to the enlargement of the surface area resulting in the enhancement of the mass transport for the redox couple within the structurally porous electrode.

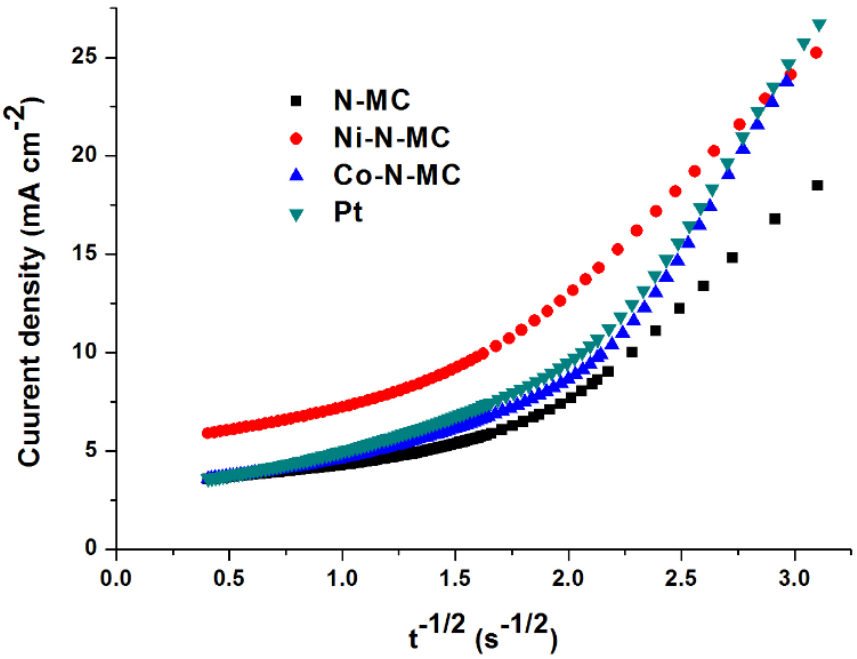

Figure 39. Potential-step chronoamperometry with the potential step from 0 V to 0.8 V for 10 s.

To validate the electrochemical performance of CEs for DSC application, EIS using symmetrical cells with two identical CEs was carried out.[90] Figure 40(a) depicts the Nyquist plots of the symmetrical cells employing platinized, N-MC, Co-N-MC,

and Ni-N-MC electrodes. Figure 40(b) gives a typical equivalent circuit used to fit the EIS spectra by using ZView software in order to obtain the electrochemical parameters. In a Nyquist plot, the ohmic process reflected by series resistance (R_s) can be obtained from the intercept on the real axis (Z') in high frequency end. This may include the contributions from the sheet resistance of FTO as well as the interfacial contact resistance between FTO and electrocatalyst layer and/or between individual electrocatalyst materials. In EIS spectra, there are two distinct characteristic semicircles. The left semicircle in high-frequency region can be attributed to the resistance capacitance (RC) networks of the electrode/electrolyte interface, including the charge-transfer resistance (R_{ct}) in parallel with the electric double layer capacitor (C_{μ}). For modeling porous electrodes, C_{μ} is generally replaced by a constant phase element (CPE) for non-ideal capacitor. The right semicircle in the low-frequency region can be assigned to the diffusion process of I^-/I_3^- species in the cell, which can be characterized by typical Nernst diffusion impedance (Z_N).[89] The EIS data were summarized in Table 2. Due to the high electrical conductivity of Pt electrocatalyst, the R_s value of cell using platinized electrode (25.2 Ω) is slightly lower than those of cells using N-MC (30.4 Ω), Co-N-MC (26.9 Ω), and Ni-N-MC (26.6 Ω) electrodes. The higher R_s values for all mesoporous carbon electrodes are resulting from large numbers of grain boundaries between the carbon nanoparticles. Among the N-doped mesoporous carbon electrodes, the decrease of R_s values was observed for Co-N-MC and Ni-N-MC electrodes, which may be attributed to the addition of Co and Ni compound nanoparticles that enhanced the graphitization degree of the Co-N-MC and Ni-N-MC composites, respectively. The R_{ct} values of Co-N-MC and Ni-N-MC are 4.6 and 3.8 Ω cm^2, respectively, which are lower than that of cell using N-MC (6.3 Ω cm^2), clearly demonstrating metal-doping effect. Moreover, the R_{ct} value of Ni-N-MC electrode is also lower than that of cell using platinized electrode (4.7 Ω cm^2). The

results are in good agreement with the cyclic voltammetry revealing that the Ni-N-MC electrode exhibits higher electrocatalytic ability for I^-/I_3^- couple. Furthermore, the C_μ values of all mesoporous carbon samples (Ni-N-MC = 49.8 μF cm^{-2}, Co-N-MC = 42.7 μF cm^{-2}, and N-MC = 34.6 μF cm^{-2}) are significantly larger than that of platinized electrode (5.8 μF cm^{-2}) and the highest C_μ value of Ni-N-MC nanocomposite is observed as well. The enhanced capacitance at the Ni-N-MC-electrolyte interface can be attributed to the large surface area and pore volume in the Ni-N-MC which is consistent with the results from nitrogen adsorption/desorption isotherms.

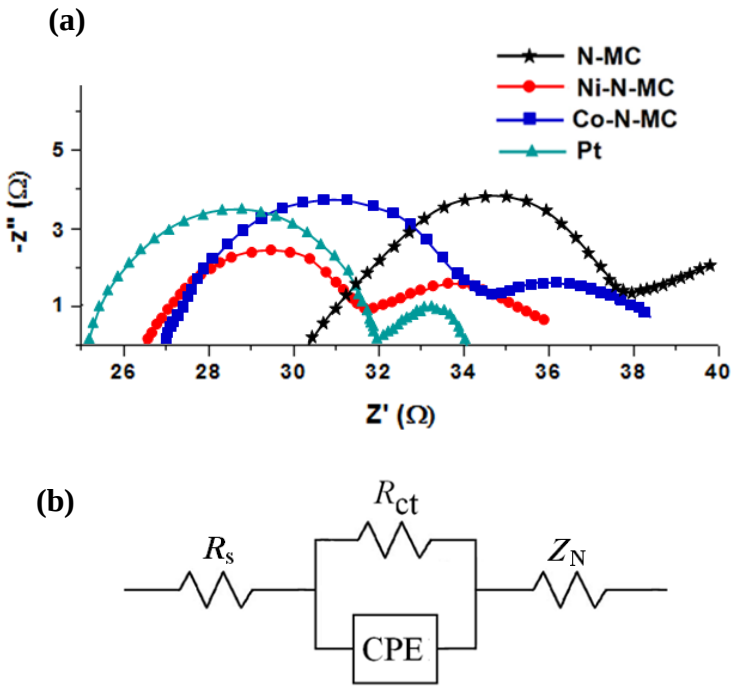

Figure 40. (a) Nyquist plots of EIS measured at 0 V from 10^6 to 0.1 Hz on the symmetrical dummy cells with platinized, N-MC, Co-N-MC, and Ni-N-MC as the counter electrodes using I^-/I_3^- redox couple in acetonitrile and (b) Equivalent circuit diagram for fitting of EIS data.

Table 2. Electrochemical Impedance Parameters in the Symmetrical Dummy Cells with Different Sample Electrodes and Electrolytes.

Electrolyte	Electrode	R_s (Ω)	R_{ct} (Ω cm^2)	CPE (μF/cm^2)	j_0 (mA/cm^2)
I^-/I_3^-	Platinized	25.2 ± 0.4	4.7 ± 0.2	5.8 ± 0.3	2.7 ± 0.1
	N-MC	31.8 ± 0.5	6.3 ± 0.4	34.6 ± 0.3	2.0 ± 0.4
	Co-N-MC	26.9 ± 0.3	4.9 ± 0.5	42.7 ± 0.5	2.6 ± 0.4
	Ni-N-MC	26.6 ± 0.1	3.8 ± 0.3	49.8 ± 0.4	3.4 ± 0.2
T_2/T^-	Platinized	31.1 ± 0.2	44.2 ± 0.5	4.1 ± 0.5	0.29 ± 0.04
	N-MC	42.4 ± 0.3	21.3 ± 0.1	20.9 ± 0.2	0.60 ± 0.01
	Co-N-MC	40.2 ± 0.2	16.0 ± 0.4	40.4 ± 0.3	0.80 ± 0.04
	Ni-N-MC	33.3 ± 0.4	14.4 ± 0.5	63.6 ± 0.1	0.89 ± 0.01

To evaluate the electrochemical stability of the sample electrodes, the EIS of these CEs is measured with varying CV cycles at room temperature. With increasing the scan numbers of CV cycles under cycling potential between −1.0 and 1.0 V in I^-/I_3^- solution in acetonitrile, the variation curves of Nyquist plots for both platinized and Ni-N-MC electrodes assembled in the dummy cell compartment are shown in Figure 41(a) and Figure 41(b), respectively. The R_{ct} value for the freshly platinized electrode was initially 4.7 Ω cm^2 but it was increased to 9.2 Ω cm^2 in the final cycle. On the contrary, the freshly assembled Ni-N-MC electrode exhibited the R_{ct} value of 3.8 Ω cm^2 in the first cycle and it was slightly increased up to 4.3 Ω cm^2 after 10 times. As shown in Figure 41(c), the much slower and milder deterioration of Ni-N-MC than platinized electrode clearly demonstrate that the Ni-N-MC had better electrochemical stability in I^-/I_3^- medium.

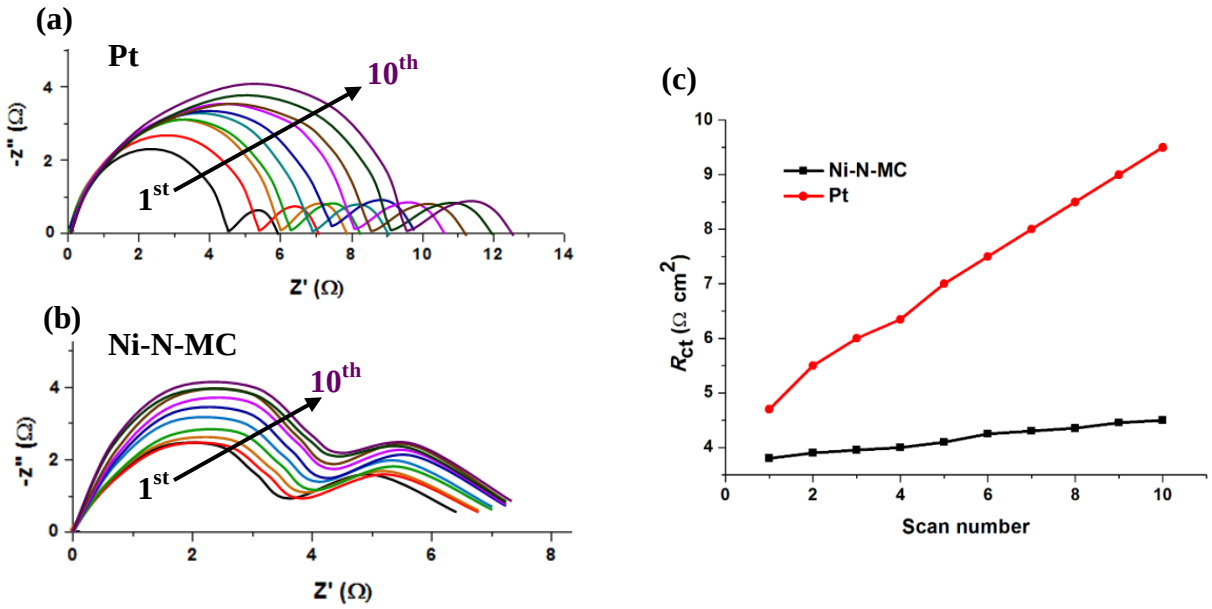

Figure 41. Electrochemical stability of dummy cells with (a) platinized and (b) Ni-N-MC in acetonitrile solution of I^-/I_3^-. The sequence of measurements is as follows: 10 × CV scans (from 0 V → 1 V→ −1 V→ 0 V at a scan rate of 50 mVs^{-1}) followed by 30 s relaxation at 0 V and then EIS measurement at zero bias potential. The sequence of electrochemical tests was repeated 10 times. (c) R_{CT} versus EIS scan number.

3.3 Photovoltaic Performances of the DSCs using Platinized, N-MC, Co-N-MC, and Ni-N-MC Counter Electrodes for Triiodide/Iodide and T_2/T^- Redox Couples.

To determine the effect of replacing Pt on the photovoltaic performance in DSC devices, the current-voltage characteristics of the DSCs fabricated with various CEs are analyzed at one sun of illumination as shown in Figure 42 and summarized in Table 3. All DSCs exhibit photovoltaic effect for converting light into electrical current with I^-/I_3^- redox couple as displayed in Figure 42(a). As compared with the DSC using N-MC CE, the short-circuit current densities (J_{sc}) of the DSCs using Co-N-MC and Ni-N-MC CEs are improved from 14.2 to 15.0 and 16.6 mA cm^{-2}, fill factors (FF) are improved from 0.62 to 0.70, and the power conversion efficiency (η) values are improved from 7.10 to 7.57 and 8.42 %, respectively. The lower degree of graphitization (as the Raman measurements confirm) and lower electrocatalytic

performance (as the CV experiments confirm) of N-MC CE give rise to a significantly decrease in the J_{sc} and FF values resulting in lower η value of DSC. The incorporation of metal compound nanoparticles into N-doped mesoporous carbon is indispensable for facilitating the heterogeneous electron-transfer process at the CE/electrolyte interface which is evident from the smaller value of R_{ct}. Moreover, the large surface area and wide pore volume including pore size of metal species immobilized on N-doped mesoporus carbon give also rise to high transport rate of electrolyte species. As shown in Table 3, both the open-circuit voltage (V_{oc}) and FF values of Ni-N-MC-based DSC (V_{oc} = 0.73 V, FF = 0.70) are slightly higher than those of platinized-based DSC (V_{oc} = 0.70 V, FF = 0.66) leading to the improvement of the overall cell performance (8.42 % for Ni-N-MC CE and 8.22% for platinized CE). The superior cell performance of Ni-N-MC based-DSC can be attributed to the high electrocatalytic activity as indicated by high pyridinic and graphitic N contents combined with the feasibility of the charge-transfer process as indicated by the small R_{ct} value. Therefore, these make Ni-N-MC applicable to the large-scale DSC application.

In the case of di-5-(1-methyltetrazole) disulfide/5-mercapto-1-methyltetrazole *N*-tetramethyl-ammonium salt redox couple[63, 91] Figure 42(b) shows the *J*–*V* curves of the N-MC, Co-N-MC, Ni-N-MC, and platinized-based DSCs with T_2/T^-, as a redox couple. The platinized-based DSC shows a J_{sc} of 16.6 mA cm^{-2}, a V_{oc} of 0.70 V, a FF of 0.45, and a η of 5.25%. When the CE was changed from platinized CE to all N-doped mesoporous carbon CEs, the FF values were improved significantly to 0.53, 0.60, and 0.62 for N-MC, Co-N-MC, and Ni-N-MC, respectively. Consequently, the η of DSCs based on all N-doped mesoporous carbon CEs increased to 5.90, 6.80, and 6.95 % for DSCs using N-MC, Co-N-MC, and Ni-N-MC, respectively. Interestingly, unlike in the case of I^-/I_3^- redox couple, all N-doped mesoporous carbon CEs show higher electrocatalytic activity than platinized CE for

the regeneration of T_2/T^- redox couple. This implies an ease or efficiency of the interfacial electron transfer reaction towards T_2/T^- redox couple at the interfaces between all N-doped mesoporous carbons and electrolyte. Therefore, it is highly desirable to match the appropriate CE electrocatalysts to the redox couple in order to achieve optimum devices.[91, 92]

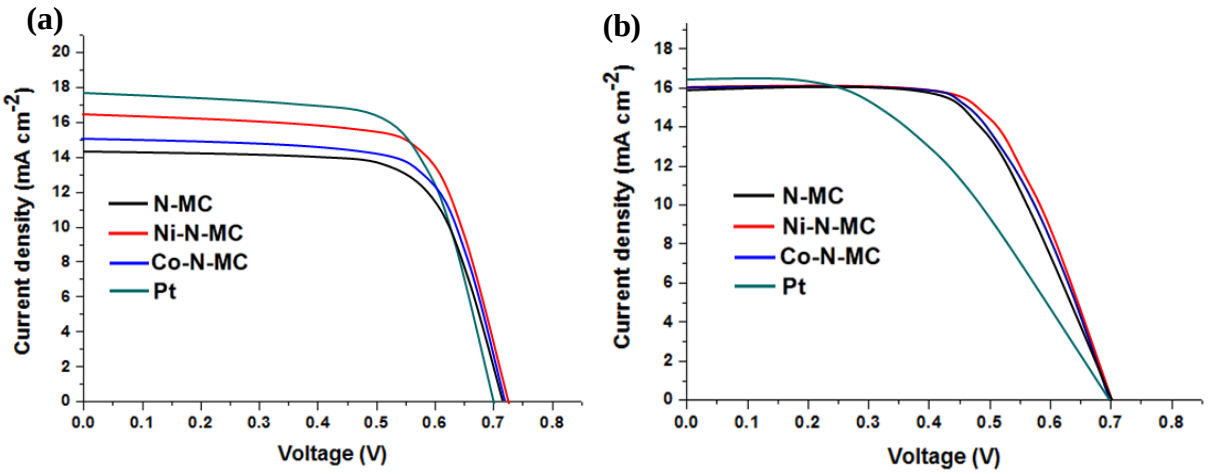

Figure 42. Current-voltage characteristics of DSCs with platinized, N-MC, Co-N-MC, Ni-N-MC as the CEs in (a) I^-/I_3^- and (b) T_2/T^- electrolytes.

Table 3. Photovoltaic Parameters of DSCs with Different CEs and Electrolytes

Electrolyte	CE	V_{oc} (V)	J_{sc} (mA/cm^2)	FF	η (%)
I^-/I_3^-	Platinized	0.70 ± 0.01	17.8 ± 0.1	0.66 ± 0.05	8.22 ± 0.02
	N-MC	0.72 ± 0.01	14.2 ± 0.1	0.62 ± 0.01	6.34 ± 0.01
	Co-N-MC	0.72 ± 0.03	15.0 ± 0.3	0.70 ± 0.01	7.57 ± 0.01
	Ni-N-MC	0.73 ± 0.04	16.6 ± 0.4	0.70 ± 0.02	8.42 ± 0.02
T_2/T^-	Platinized	0.70 ± 0.03	16.6 ± 0.5	0.45 ± 0.03	5.25 ± 0.02
	N-MC	0.70 ± 0.01	15.9 ± 0.1	0.53 ± 0.01	5.90 ± 0.01
	Co-N-MC	0.70 ± 0.01	16.0 ± 0.2	0.60 ± 0.01	6.80 ± 0.01
	Ni-N-MC	0.71 ± 0.03	16.0 ± 0.3	0.62 ± 0.03	6.95 ± 0.02

To further examine the electrocatalytic activity of N-MC, Co-N-MC, Ni-N-MC, and platinized electrodes with T_2/T^- redox couple, EIS experiments of dummy cells were carried out similarly, as previously discussed for the reduction of I^-/I_3^- redox system. Figure 43 shows the Nyquist plots of the N-MC, Co-N-MC, Ni-N-MC, and platinized symmetrically cells and EIS parameters are summarized in Table 2. The value of R_{ct} of the platinized (44.2 Ω cm^2) dummy cell is much larger than those

of the N-MC (21.3 Ω cm^2), Co-N-MC (16.0 Ω cm^2), and Ni-N-MC (14.4 Ω cm^2) dummy cells. This implies the enhanced power photovoltaic performance of the DSCs using N-MC, Co-N-MC, and Ni-N-MC CEs with T_2/T^- redox couple. However, the DSCs operating under T_2/T^- redox couple have higher R_{ct} values than those operating under I^-/I_3^- redox system, resulting in the lower photovoltaic performance. The higher R_{ct} values for the reduction of T_2 to T^- are due to the impediment of the electrolyte transport in the narrow pore channels inside the carbon matrix, leading to the increased mass-transfer resistance and slow diffusion of T_2/T^- redox couple. As an evident, the increase in impedance is observed in the low-frequency semicircle for T_2/T^- redox couple.

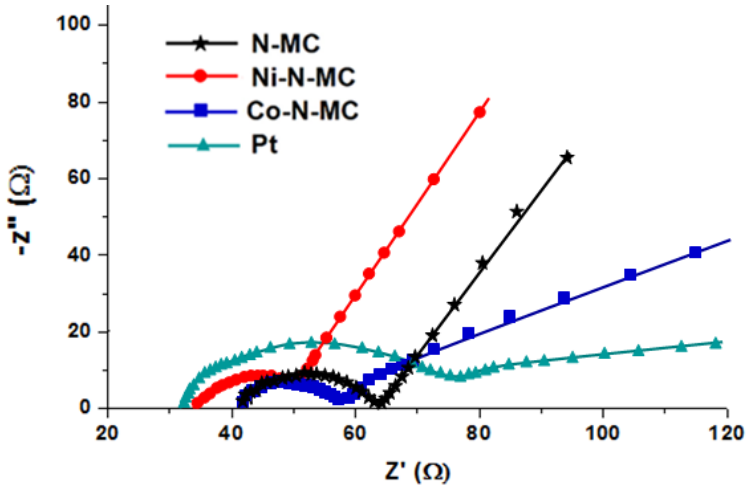

Figure 43. Nyquist plots measured at 0 V from 10^6 to 0.1 Hz on the symmetrical dummy cells with platinized, N-MC, Co-N-MC, and Ni-N-MC as the counter electrodes using T_2/T^- redox couple system.

4. Conclusions

In summary, the synthesized Co or Ni species immobilized on N-doped mesoporous carbon (Co-N-MC or Ni-N-MC) with high surface area showed excellent electrocatalytic activity towards the electrochemical reduction of triiodide in DSC systems as compared with N-doped mesoporous carbon (N-MC). The predominating contents of pyridinic and quaternary N species over pyrrolic N as well as good

electrical conductivity in the Co-N-MC and Ni-N-MC frameworks are considered to contribute positively on the photoelectric conversion efficiency of DSCs. Moreover, the improvement of photovoltaic performance can also be ascribed to a much lower charge-transfer resistance (R_{ct}) related to superb structural surface properties and metal-doping of the Co-N-MC and Ni-N-MC. Compared to the DSC employing platinized counter electrode (FF = 0.66 and η = 8.22%), the fill factor (FF) and photoelectric conversion efficiency (η) of DSC employing Ni-N-MC counter electrode (FF = 0.70 and η = 8.42%) were higher. Furthermore, the Ni-N-MC electrode that was experienced 10 CV cycles also showed good electrochemical stability. In addition, N-MC, Co-N-MC, and Ni-N-MC all preformed better than platinized electrode in catalyzing the T_2/T^- organic redox system. The combination of electrocatalytic Co or Ni species and N-doped mesoporous carbon matrix is an alternative design for counter electrode electrocalyst to reduce the cost of DSCs. Last but not least, in the fabrication procedure of DSCs, an attempt to couple the suitable counter electrode electrocatalysts and the redox couples should also be considered.

References

1. Lewis, N. S., Toward cost-effective solar energy use. *Science* **2007,** 315, (5813), 798-801.

2. Nansen, R., *Sun Power: The Global Solution for the Coming Energy Crisis.* Ocean Press: Washington, 1995.

3. O'REGAN, B.; GRÄTZEL, M., A low-cost, high-efficiency solar cell based on dye-sensitized colloidal TiO2 films. *Nature* **1991,** 353, 737-740.

4. Gratzel, M., Recent Advances in Sensitized Mesoscopic Solar Cells. *Accounts of Chemical Research* **2009,** 42, (11), 1788-1798.

5. Hagfeldt, A.; Boschloo, G.; Sun, L. C.; Kloo, L.; Pettersson, H., Dye-Sensitized Solar Cells. *Chemical Reviews* **2010,** 110, (11), 6595-6663.

6. Hardin, B. E.; Snaith, H. J.; McGehee, M. D., The renaissance of dye-sensitized solar cells. *Nature Photonics* **2012,** 6, (3), 162-169.

7. Grätzel, M., Solar Energy Conversion by Dye-Sensitized Photovoltaic Cells. *Inorg. Chem.* **2005,** 44, (20), 6841-6851.

8. Ma, T. L.; Fang, X. M.; Akiyama, M.; Inoue, K.; Noma, H.; Abe, E., Properties of several types of novel counter electrodes for dye-sensitized solar cells. *Journal of Electroanalytical Chemistry* **2004,** 574, (1), 77-83.

9. Calogero, G.; Calandra, P.; Irrera, A.; Sinopoli, A.; Citro, I.; Di Marco, G., A new type of transparent and low cost counter-electrode based on platinum nanoparticles for dye-sensitized solar cells. *Energy & Environmental Science* **2011,** 4, (5), 1838-1844.

10. Murakami, T. N.; Gratzel, M., Counter electrodes for DSC: Application of functional materials as catalysts. *Inorganica Chimica Acta* **2008,** 361, (3), 572-580.

11. Wu, M. X.; Ma, T. L., Platinum-Free Catalysts as Counter Electrodes in Dye-Sensitized Solar Cells. *Chemsuschem* **2012,** 5, (8), 1343-1357.

12. Veerappan, G.; Bojan, K.; Rhee, S. W., Sub-micrometer-sized Graphite As a Conducting and Catalytic Counter Electrode for Dye-sensitized Solar Cells. *Acs Applied Materials & Interfaces* **2011,** 3, (3), 857-862.

13. Murakami, T. N.; Ito, S.; Wang, Q.; Nazeeruddin, M. K.; Bessho, T.; Cesar, I.; Liska, P.; Humphry-Baker, R.; Comte, P.; Pechy, P.; Gratzel, M., Highly efficient dye-sensitized solar cells based on carbon black counter electrodes. *Journal of the Electrochemical Society* **2006,** 153, (12), A2255-a2261.

14. Joshi, P.; Zhang, L. F.; Chen, Q. L.; Galipeau, D.; Fong, H.; Qiao, Q. Q., Electrospun Carbon Nanofibers as Low-Cost Counter Electrode for Dye-Sensitized Solar Cells. *Acs Applied Materials & Interfaces* **2010,** 2, (12), 3572-3577.

15. Lee, W. J.; Ramasamy, E.; Lee, D. Y.; Song, J. S., Efficient Dye-Sensitized Solar Cells with Catalytic Multiwall Carbon Nanotube Counter Electrodes. *ACS Appl. Mater. Interfaces* **2009,** 1, (6), 1145-1149.

16. Ramasamy, E.; Lee, W. J.; Lee, D. Y.; Song, J. S., Spray coated multi-wall carbon nanotube counter electrode for tri-iodide (I-3(-)) reduction in dye-sensitized solar cells. *Electrochemistry Communications* **2008,** 10, (7), 1087-1089.

17. Lee, K. S.; Lee, W. J.; Park, N. G.; Kim, S. O.; Park, J. H., Transferred vertically aligned N-doped carbon nanotube arrays: use in dye-sensitized solar cells as counter electrodes. *Chemical Communications* **2011,** 47, (14), 4264-4266.

18. Wu, M. X.; Lin, X.; Wang, T. H.; Qiu, J. S.; Ma, T. L., Low-cost dye-sensitized solar cell based on nine kinds of carbon counter electrodes. *Energy & Environmental Science* **2011,** 4, (6), 2308-2315.

19. Xue, Y. H.; Liu, J.; Chen, H.; Wang, R. G.; Li, D. Q.; Qu, J.; Dai, L. M., Nitrogen-Doped Graphene Foams as Metal-Free Counter Electrodes in High-Performance Dye-Sensitized Solar Cells. *Angewandte Chemie-International Edition* **2012,** 51, (48), 12124-12127.

20. Wang, H.; Hu, Y. H., Graphene as a counter electrode material for dye-sensitized solar cells. *Energy & Environmental Science* **2012,** 5, (8), 8182-8188.

21. Rolison, D. R., Catalytic nanoarchitectures - The importance of nothing and the unimportance of periodicity. *Science* **2003,** 299, (5613), 1698-1701.

22. Joo, S. H.; Choi, S. J.; Oh, I.; Kwak, J.; Liu, Z.; Terasaki, O.; Ryoo, R., Ordered nanoporous arrays of carbon supporting high dispersions of platinum nanoparticles (vol 412, pg 169, 2001). *Nature* **2001,** 414, (6862), 470-470.

23. Lee, J.; Kim, J.; Hyeon, T., Recent progress in the synthesis of porous carbon materials. *Advanced Materials* **2006,** 18, (16), 2073-2094.

24. Mattevi, C.; Eda, G.; Agnoli, S.; Miller, S.; Mkhoyan, K. A.; Celik, O.; Mostrogiovanni, D.; Granozzi, G.; Garfunkel, E.; Chhowalla, M., Evolution of Electrical, Chemical, and Structural Properties of Transparent and Conducting Chemically Derived Graphene Thin Films. *Advanced Functional Materials* **2009,** 19, (16), 2577-2583.

25. Roy-Mayhew, J. D.; Bozym, D. J.; Punckt, C.; Aksay, I. A., Functionalized Graphene as a Catalytic Counter Electrode in Dye-Sensitized Solar Cells. *Acs Nano* **2010,** 4, (10), 6203-6211.

26. Yu, D. S.; Nagelli, E.; Du, F.; Dai, L. M., Metal-Free Carbon Nanomaterials Become More Active than Metal Catalysts and Last Longer. *Journal of Physical Chemistry Letters* **2010,** 1, (14), 2165-2173.

27. Yang, S. B.; Feng, X. L.; Wang, X. C.; Mullen, K., Graphene-Based Carbon Nitride Nanosheets as Efficient Metal-Free Electrocatalysts for Oxygen Reduction Reactions. *Angewandte Chemie-International Edition* **2011,** 50, (23), 5339-5343.

28. Wang, X. Q.; Lee, J. S.; Zhu, Q.; Liu, J.; Wang, Y.; Dai, S., Ammonia-Treated Ordered Mesoporous Carbons as Catalytic Materials for Oxygen Reduction Reaction. *Chemistry of Materials* **2010,** 22, (7), 2178-2180.

29. Gong, K. P.; Du, F.; Xia, Z. H.; Durstock, M.; Dai, L. M., Nitrogen-Doped Carbon Nanotube Arrays with High Electrocatalytic Activity for Oxygen Reduction. *Science* **2009,** 323, (5915), 760-764.

30. Yu, D. S.; Zhang, Q.; Dai, L. M., Highly Efficient Metal-Free Growth of Nitrogen-Doped Single-Walled Carbon Nanotubes on Plasma-Etched Substrates for Oxygen Reduction. *Journal of the American Chemical Society* **2010,** 132, (43), 15127-15129.

31. Wu, G.; Mack, N. H.; Gao, W.; Ma, S. G.; Zhong, R. Q.; Han, J. T.; Baldwin, J. K.; Zelenay, P., Nitrogen Doped Graphene-Rich Catalysts Derived from

Heteroatom Polymers for Oxygen Reduction in Nonaqueous Lithium-O-2 Battery Cathodes. *Acs Nano* **2012,** 6, (11), 9764-9776.

32. Silva, R.; Voiry, D.; Chhowalla, M.; Asefa, T., Efficient Metal-Free Electrocatalysts for Oxygen Reduction: Polyaniline-Derived N- and O-Doped Mesoporous Carbons. *Journal of the American Chemical Society* **2013,** 135, (21), 7823-7826.

33. Oslen, E.; Hagen, G.; Linquist, S. E., Dissolution of platinum in methoxy propionitrile containing LiI/I2. *Sol. Energy Mater. Sol. Cells* **2000,** 63, 267.

34. Andreas Kay; Gratzel, M., Low cost photovoltaic modules based on dye sensitized nanocrystalline titanium dioxide and carbon powder. *Solar Energy Materials and Solar Cells* **1996,** 44, 99-117.

35. Imoto, K.; Takahashi, K.; Yamaguchi, T.; Komura, T.; Nakamura, J.; Murata, K., High-performance carbon counter electrode for dye-sensitized solar cells. *Solar Energy Materials and Solar Cells* **2003,** 79, (4), 459-469.

36. Nam, J. G.; Park, Y. J.; Kim, B. S.; Lee, J. S., Enhancement of the efficiency of dye-sensitized solar cell by utilizing carbon nanotube counter electrode. *Scripta Materialia* **2010,** 62, (3), 148-150.

37. Saito, Y.; Kubo, W.; Kitamura, T.; Wada, Y.; Yanagida, S., I-/I-3(-) redox reaction behavior on poly(3,4-ethylenedioxythiophene) counter electrode in dye-sensitized solar cells. *Journal of Photochemistry and Photobiology a-Chemistry* **2004,** 164, (1-3), 153-157.

38. Ramasamy, E.; Lee, W. J.; Lee, D. Y.; Song, J. S., Nanocarbon counterelectrode for dye sensitized solar cells. *Applied Physics Letters* **2007,** 90, (17).

39. Nugent, J. M.; Santhanam, K. S. V.; Rubio, A.; Ajayan, P. M., Fast electron transfer kinetics on multiwalled carbon nanotube microbundle electrodes. *Nano Letters* **2001,** 1, (2), 87-91.

40. Banks, C. E.; Compton, R. G., New electrodes for old: from carbon nanotubes to edge plane pyrolytic graphite. *Analyst* **2006,** 131, (1), 15-21.

41. Joshi, P.; Xie, Y.; Ropp, M.; Galipeau, D.; Bailey, S.; Qiao, Q. Q., Dye-sensitized solar cells based on low cost nanoscale carbon/TiO2 composite counter electrode. *Energy & Environmental Science* **2009,** 2, (4), 426-429.

42. Li, D.; Kaner, R. B., Graphene-Based Materials. *Science (Washington, DC, U. S.)* **2008,** 320, (5880), 1170-1171.

43. Li, X. L.; Zhang, G. Y.; Bai, X. D.; Sun, X. M.; Wang, X. R.; Wang, E.; Dai, H. J., Highly conducting graphene sheets and Langmuir-Blodgett films. *Nature Nanotechnology* **2008,** 3, (9), 538-542.

44. Xu, Y. X.; Bai, H.; Lu, G. W.; Li, C.; Shi, G. Q., Flexible graphene films via the filtration of water-soluble noncovalent functionalized graphene sheets. *Journal of the American Chemical Society* **2008,** 130, (18), 5856-+.

45. Hong, W. J.; Xu, Y. X.; Lu, G. W.; Li, C.; Shi, G. Q., Transparent graphene/PEDOT-PSS composite films as counter electrodes of dye-sensitized solar cells. *Electrochemistry Communications* **2008,** 10, (10), 1555-1558.

46. Choi, H.; Kim, H.; Hwang, S.; Choi, W.; Jeon, M., Dye-sensitized solar cells using graphene-based carbon nano composite as counter electrode. *Solar Energy Materials and Solar Cells* **2011,** 95, (1), 323-325.

47. Zhang, D. W.; Li, X. D.; Li, H. B.; Chen, S.; Sun, Z.; Yin, X. J.; Huang, S. M., Graphene-based counter electrode for dye-sensitized solar cells. *Carbon* **2011,** 49, (15), 5382-5388.

48. Qu, L. T.; Liu, Y.; Baek, J. B.; Dai, L. M., Nitrogen-Doped Graphene as Efficient Metal-Free Electrocatalyst for Oxygen Reduction in Fuel Cells. *Acs Nano* **2010,** 4, (3), 1321-1326.

49. Ayala, P.; Arenal, R.; Rummeli, M.; Rubio, A.; Pichler, T., The doping of carbon nanotubes with nitrogen and their potential applications. *Carbon* **2010,** 48, (3), 575-586.

50. Trancik, J. E.; Barton, S. C.; Hone, J., Transparent and catalytic carbon nanotube films. *Nano Letters* **2008,** 8, (4), 982-987.

51. Fang, B. Z.; Fan, S. Q.; Kim, J. H.; Kim, M. S.; Kim, M.; Chaudhari, N. K.; Ko, J.; Yu, J. S., Incorporating Hierarchical Nanostructured Carbon Counter Electrode into Metal-Free Organic Dye-Sensitized Solar Cell. *Langmuir* **2010,** 26, (13), 11238-11243.

52. Schniepp, H. C.; Li, J. L.; McAllister, M. J.; Sai, H.; Herrera-Alonso, M.; Adamson, D. H.; Prud'homme, R. K.; Car, R.; Saville, D. A.; Aksay, I. A., Functionalized single graphene sheets derived from splitting graphite oxide. *Journal of Physical Chemistry B* **2006,** 110, (17), 8535-8539.

53. Kudin, K. N.; Ozbas, B.; Schniepp, H. C.; Prud'homme, R. K.; Aksay, I. A.; Car, R., Raman spectra of graphite oxide and functionalized graphene sheets. *Nano Letters* **2008,** 8, (1), 36-41.

54. Schniepp, H. C.; Kudin, K. N.; Li, J. L.; Prud'homme, R. K.; Car, R.; Saville, D. A.; Aksay, I. A., Bending Properties of Single Functionalized Graphene Sheets Probed by Atomic Force Microscopy. *Acs Nano* **2008,** 2, (12), 2577-2584.

55. McAllister, M. J.; Li, J. L.; Adamson, D. H.; Schniepp, H. C.; Abdala, A. A.; Liu, J.; Herrera-Alonso, M.; Milius, D. L.; Car, R.; Prud'homme, R. K.; Aksay, I. A., Single sheet functionalized graphene by oxidation and thermal expansion of graphite. *Chemistry of Materials* **2007,** 19, (18), 4396-4404.

56. Sato, K.; Saito, R.; Oyama, Y.; Jiang, J.; Cancado, L. G.; Pimenta, M. A.; Jorio, A.; Samsonidze, G. G.; Dresselhaus, G.; Dresselhaus, M. S., D-band Raman

intensity of graphitic materials as a function of laser energy and crystallite size. *Chemical Physics Letters* **2006,** 427, (1-3), 117-121.

57. Wan, Y.; Shi, Y. F.; Zhao, D. Y., Supramolecular aggregates as templates: Ordered mesoporous polymers and carbons. *Chemistry of Materials* **2008,** 20, (3), 932-945.

58. Ramasamy, E.; Lee, J., Ferrocene-derivatized ordered mesoporous carbon as high performance counter electrodes for dye-sensitized solar cells. *Carbon* **2010,** 48, (13), 3715-3720.

59. Czerw, R.; Terrones, M.; Charlier, J. C.; Blase, X.; Foley, B.; Kamalakaran, R.; Grobert, N.; Terrones, H.; Tekleab, D.; Ajayan, P. M.; Blau, W.; Ruhle, M.; Carroll, D. L., Identification of electron donor states in N-doped carbon nanotubes. *Nano Letters* **2001,** 1, (9), 457-460.

60. Lee, D. H.; Lee, W. J.; Kim, S. O., Highly Efficient Vertical Growth of Wall-Number-Selected, N-Doped Carbon Nanotube Arrays. *Nano Letters* **2009,** 9, (4), 1427-1432.

61. Chang, H.; Joo, S. H.; Pak, C., Synthesis and characterization of mesoporous carbon for fuel cell applications. *Journal of Materials Chemistry* **2007,** 17, (30), 3078-3088.

62. Wang, G. Q.; Huang, C. C.; Xing, W.; Zhuo, S. P., Micro-meso hierarchical porous carbon as low-cost counter electrode for dye-sensitized solar cells. *Electrochimica Acta* **2011,** 56, (16), 5459-5463.

63. Wang, M. K.; Chamberland, N.; Breau, L.; Moser, J. E.; Humphry-Baker, R.; Marsan, B.; Zakeeruddin, S. M.; Gratzel, M., An organic redox electrolyte to rival triiodide/iodide in dye-sensitized solar cells. *Nature Chemistry* **2010,** 2, (5), 385-389.

64. Roy, S. C.; Harding, A. W.; Russell, A. E.; Thomas, K. M., Spectroelectrochemical Study of the Role Played by Carbon Functionality in Fuel Cell

Electrodes (vol 144, pg 2323, 1997). *Journal of the Electrochemical Society* **2011,** 158, (2), S3-S3.

65. Yue, B.; Ma, Y. W.; Tao, H. S.; Yu, L. S.; Jian, G. Q.; Wang, X. Z.; Wang, X. S.; Lu, Y. N.; Hu, Z., CNx nanotubes as catalyst support to immobilize platinum nanoparticles for methanol oxidation. *Journal of Materials Chemistry* **2008,** 18, (15), 1747-1750.

66. Maldonado, S.; Morin, S.; Stevenson, K. J., Structure, composition, and chemical reactivity of carbon nanotubes by selective nitrogen doping. *Carbon* **2006,** 44, (8), 1429-1437.

67. Ferrari, A. C.; Robertson, J., Interpretation of Raman spectra of disordered and amorphous carbon. *Physical Review B: Condensed Matter and Materials Physics* **2000,** 61, (20), 14095-14107.

68. Jia, N. Q.; Wang, Z. Y.; Yang, G. F.; Shen, H. B.; Zhu, L. Z., Electrochemical properties of ordered mesoporous carbon and its electroanalytical application for selective determination of dopamine. *Electrochemistry Communications* **2007,** 9, (2), 233-238.

69. Liu, S. H.; Wu, M. T.; Lai, Y. H.; Chiang, C. C.; Yu, N. Y.; Liu, S. B., Fabrication and electrocatalytic performance of highly stable and active platinum nanoparticles supported on nitrogen-doped ordered mesoporous carbons for oxygen reduction reaction. *Journal of Materials Chemistry* **2011,** 21, (33), 12489-12496.

70. Wang, T.; Zhang, C. X.; Sun, X.; Guo, Y. X.; Guo, H.; Tang, J.; Xue, H. R.; Liu, M. Z.; Zhang, X. X.; Zhu, L.; Xie, Q. Q.; He, J. P., Synthesis of ordered mesoporous boron-containing carbon films and their corrosion behavior in simulated proton exchange membrane fuel cells environment. *Journal of Power Sources* **2012,** 212, 1-12.

71. Xia, Y. D.; Mokaya, R., Generalized and facile synthesis approach to N-doped highly graphitic mesoporous carbon materials. *Chemistry of Materials* **2005,** 17, (6), 1553-1560.

72. Lin, Z. Y.; Waller, G.; Liu, Y.; Liu, M. L.; Wong, C. P., Facile Synthesis of Nitrogen-Doped Graphene via Pyrolysis of Graphene Oxide and Urea, and its Electrocatalytic Activity toward the Oxygen-Reduction Reaction. *Advanced Energy Materials* **2012,** 2, (7), 884-888.

73. Pels, J. R.; Kapteijn, F.; Moulijin, J. A.; Zhu, Q.; Thomas, K. M., Evolution of nitrogen functionalities in carbonaceous materials during pyrolysis. *Carbon* **1995,** 33, (11), 1641-1653.

74. Delpeux, S.; Beguin, F.; Benoit, R.; Erre, R.; Manolova, N.; Rashkov, I., Fullerene core star-like polymers. 1. Preparation from fullerenes and monoazidopolyethers. *European Polymer Journal* **1998,** 34, (7), 905-915.

75. Lahaye, J.; Nanse, G.; Bagreev, A.; Strelko, V., Porous structure and surface chemistry of nitrogen containing carbons from polymers. *Carbon* **1999,** 37, (4), 585-590.

76. Hulicova-Jurcakova, D.; Seredych, M.; Lu, G. Q.; Bandosz, T. J., Combined Effect of Nitrogen- and Oxygen-Containing Functional Groups of Microporous Activated Carbon on its Electrochemical Performance in Supercapacitors. *Advanced Functional Materials* **2009,** 19, (3), 438-447.

77. Hou, S. C.; Cai, X.; Wu, H. W.; Yu, X.; Peng, M.; Yan, K.; Zou, D. C., Nitrogen-doped graphene for dye-sensitized solar cells and the role of nitrogen states in triiodide reduction. *Energy & Environmental Science* **2013,** 6, (11), 3356-3362.

78. McIntyre, N. S.; Cook, M. G., X-ray photoelectron studies on some oxides and hydroxides of cobalt, nickel, and copper. *Analytical Chemistry* **1975,** 47, (13), 2208-2213.

79. Mandale, A. B.; Badrinarayanan, S.; Date, S. K.; Sinha, A. P. B., Photoelectron-spectroscopic study of nickel, manganese and cobalt selenides. *Journal of Electron Spectroscopy and Related Phenomena* **1984,** 33, (1), 67-72.

80. Tan, B. J.; Klabunde, K. J.; Sherwood, P. M. A., XPS studies of solvated metal atom dispersed (SMAD) catalysts. Evidence for layered cobalt-manganese particles on alumina and silica. *Journal of the American Chemical Society* **1991,** 113, (3), 855-861.

81. Kenney, M. J.; Gong, M.; Li, Y. G.; Wu, J. Z.; Feng, J.; Lanza, M.; Dai, H. J., High-Performance Silicon Photoanodes Passivated with Ultrathin Nickel Films for Water Oxidation. *Science* **2013,** 342, (6160), 836-840.

82. El Baydi, M.; Tiwari, S. K.; Singh, R. N.; Rehspringer, J.-L.; Chartier, P.; Koenig, J. F.; Poillerat, G., High specific surface area nickel mixed oxide powders LaNiO3 (Perovskite) and NiCo2O4 (spinel) via sol-gel type routes for oxygen electrocatalysis in alkaline media. *Journal of Solid State Chemistry* **1995,** 116, (1), 157-169.

83. Papageorgiou, N., Counter-electrode function in nanocrystalline photoelectrochemical cell configurations. *Coordination Chemistry Reviews* **2004,** 248, (13-14), 1421-1446.

84. Li, G. R.; Wang, F.; Jiang, Q. W.; Gao, X. P.; Shen, P. W., Carbon Nanotubes with Titanium Nitride as a Low-Cost Counter-Electrode Material for Dye-Sensitized Solar Cells. *Angewandte Chemie-International Edition* **2010,** 49, (21), 3653-3656.

85. Motlak, M.; Barakat, N. A. M.; Akhtar, M. S.; Hamza, A. M.; Kim, B. S.; Kim, C. S.; Khalil, K. A.; Almajid, A. A., High performance of NiCo nanoparticles-doped carbon nanofibers as counter electrode for dye-sensitized solar cells. *Electrochimica Acta* **2015,** 160, 1-6.

86. Saranya, K.; Subramania, A.; Sivasankar, N., Influence of earth-abundant bimetallic (Fe-Ni) nanoparticle-embedded CNFs as a low-cost counter electrode material for dye-sensitized solar cells. *Rsc Advances* **2015,** 5, (54), 43611-43619.

87. Tsao, H. N.; Comte, P.; Yi, C. Y.; Gratzel, M., Avoiding Diffusion Limitations in Cobalt(III/II)-Tris(2,2'-Bipyridine)-Based Dye-Sensitized Solar Cells by Tuning the Mesoporous TiO2 Film Properties. *Chemphyschem* **2012,** 13, (12), 2976-2981.

88. Liberatore, M.; Petrocco, A.; Caprioli, F.; La Mesa, C.; Decker, F.; Bignozzi, C. A., Mass transport and charge transfer rates for Co-(III)/Co-(II) redox couple in a thin-layer cell. *Electrochimica Acta* **2010,** 55, (12), 4025-4029.

89. Hauch, A.; Georg, A., Diffusion in the electrolyte and charge-transfer reaction at the platinum electrode in dye-sensitized solar cells. *Electrochimica Acta* **2001,** 46, (22), 3457-3466.

90. Papageorgiou, N.; Maier, W. F.; Grätzel, M., An iodine/triiodide reduction electrocatalyst for aqueous and organic media. *J. Electrochem. Soc.* **1997,** 144, 876-884.

91. Wu, M. X.; Lin, X.; Wang, L.; Guo, W.; Wang, Y. D.; Xiao, J. Q.; Hagfeldt, A.; Ma, T. L., In Situ Synthesized Economical Tungsten Dioxide Imbedded in Mesoporous Carbon for Dye-Sensitized Solar Cells As Counter Electrode Catalyst. *Journal of Physical Chemistry C* **2011,** 115, (45), 22598-22602.

92. Yang, D. S.; Kim, C.; Song, M. Y.; Park, H. Y.; Kim, J. C.; Lee, J. J.; Ju, M. J.; Yu, J. S., N-Doped Hierarchical Hollow Mesoporous Carbon as Metal-Free Cathode for Dye-Sensitized Solar Cells. *Journal of Physical Chemistry C* **2014,** 118, (30), 16694-16702.

6. Output (Acknowledge the Thailand Research Fund)

6.1 International Journal Publication

Hasin P, Amornkitbamrung V, Chanlek N; Economical Nanocomposites of Cobalt or Nickel Species and Polyaniline-Derived N-Doped Mesoporous Carbons for Dye-Sensitized Solar Cells as Counter Electrodes. *Journal of Catalysis, Submitted*, 2017.

6.2 Research Utilization and Application

(i) Establish the new knowledge and research foundation in utilizing the cheap resource for the research on the development of the new materials with a variety of properties in order to employ them in many applications

(ii) Establish the collaboration with National Science and Technology Development Agency (NSTDA), National Metal and Materials Technology Center (MTEC), National Nanotechnology Center (NANOTEC) to reinforce the research on the use of N-doped mesoporous carbons immobilized by Ni or Co as the CEs in DSCs.

(iii) Establish the research foundation in Thailand through the undergraduate program of Chemistry department at Kasetsart University.

6.3 Others e.g. national journal publication, proceeding, international conference, book chapter, patent

(i) Poster presentation

2015 Development of Economical Counter Electrode Catalyst for Dye-Sensitized Solar Cells by Employing N-Doped Mesoporous Carbon Derived by Polyaniline with surface modification of Cobalt and Nickel in 7th International

Kasetsart University Science and Technology Annual Research Symposium.

2016 Mesoporous Silica-Template Synthesis of Polyaniline-Derived N-Doped Mesoporous Carbons with Cobalt or Nickel as a Counter Electrode for Dye-Sensitized Solar Cells in 8th International Kasetsart University Science and Technology Annual Research Symposium.

(i) Oral presentation

2016 Development of economical counter electrode catalyst for dye-sensitized solar cells in Symposium on Materials Concepts for Solar Energy Conversion and Energy Storage

Elsevier Editorial System(tm) for Journal of Catalysis

Manuscript Draft

Manuscript Number:

Title: Economical Nanocomposites of Cobalt or Nickel Species and Polyaniline-Derived N-Doped Mesoporous Carbons for Dye-Sensitized Solar Cells as Counter Electrodes

Article Type: Research paper

Keywords: Nanocomposite; Cobalt or nickel species; Polyaniline-derived N-doped mesoporous carbon; Dye-sensitized solar cell; Counter electrode

Corresponding Author: Dr. Panitat - Hasin, M.S.-Ph.D.

Corresponding Author's Institution: Kasetsart University

First Author: Panitat - Hasin, M.S.-Ph.D.

Order of Authors: Panitat - Hasin, M.S.-Ph.D.; Vittaya Amornkitbamrung, Ph.D.; Narong Chanlek , Ph.D.

January 11, 2017

Editor
Journal of Catalysis

Dear Editor,

Enclosed please find the manuscript entitled "Economical Nanocomposites of Cobalt or Nickel Species and Polyaniline-Derived N-Doped Mesoporous Carbons for Dye-Sensitized Solar Cells as Counter Electrodes" that we are submitting to *Journal of Catalysis* for your consideration as an *Article*.

The corresponding author is Panitat Hasin. The address is: Department of Chemistry, Faculty of Science, Kasetsart University, Chatuchak, Bangkok, 10900, Thailand. Phone: (662) 562-5444 Ext. 2186. Email: fscipths@ku.ac.th

Considering the target of expanding solar generation up to the tetrawatt scale, much effort has been made to replace the expensive and instability Pt counter electrode (CE) by alternatives with low cost, high stability under corrosive electrolyte, and high electrocatalytic activity in order to achieve the large-scale deployment of DSCs. Thus, rational design of the CE is still challenging to obtain high performance electrocatalyst. In this work, we report the alternate design for CE electrocatalyst by combining high electrical conductivity and electrocatalytic activity into one material: cobalt or nickel species imbedded in N-doped mesoporous carbons, in which cobalt or nickel species serve as the electrocatalysts and N-doped mesoporous carbon serves as an electrical conductor. To our best knowledge, this is the first alternate design for CE electrocatalyst demonstrating the combination of excellent properties for the cobalt or nickel species and N-doped mesoporous carbon to develop low-cost and high-efficiency DSCs. Therefore, this study might potentially open up new alternate design for nanocomposites of cobalt or nickel species on N-doped mesoporous carbon matrix, particularly considering the significant applications in electrocatalysis, energy conversion, and storage. Moreover, this research also demonstrates an attempt to couple the suitable CE electrocatalysts and the redox couples in the fabrication procedure of DSCs. Due to these reasons; we think this work is novel and should be of interest to the wide readership of *Journal of Catalysis.*

I would like to suggest the following reviewers for your consideration.

Reviewer	Institution	e-mail
Prof. Sining Yun	Functional Materials Laboratory (FML), School of Materials & Mineral Resources, Xi'an University of Architecture and Technology, Xi'an, Shaanxi, 710055, China	yunsining@xauat.edu.cn
Prof. Longwei Yin	Key Laboratory for Liquid-Solid Structural Evolution and Processing of Materials, Ministry of Education, School of Materials Science and Engineering, Shandong University, Jinan 250061, PR China	yinlw@sdu.edu.cn
Prof. Chien-Kuo Hsieh	Department of Materials Engineering, Ming Chi University of Technology, 84 Gungjuan Rd., Taishan Dist., New Taipei City 24301, Taiwan, ROC.	jack_hsieh@mail.mcut.edu.tw
Prof. Jae Su Yu	Department of Electronics and Radio Engineering, Institute for Wearable Convergence Electronics, Kyung Hee University, 1 Seocheon-dong, Giheung-gu, Yongin-si, Gyeonggi-do 446-701, Republic of Korea	jsyu@khu.ac.kr
Prof. Qiu-Ping Luo	Laboratory of Optical Information Technology, School of Science, Wuhan Institute of Technology, Wuhan 430205, China	lqp_lzu@163.com
Prof. Yuan-Hsiang Yu	Department of Chemistry, Fu Jen Catholic University, New Taipei City 24205, Taiwan	084916@mail.fju.edu.tw

Finally, in accordance to the Elsevier guidelines, we would like to assure you that this paper has not been published or submitted to any other medium of a public nature, including printed and electronic journals and databases.

Thank you very much for your time and consideration of our manuscript.

With best regards,

Panitat Hasin

Department of Chemistry, Faculty of Science

Kasetsart University

Chatuchak, Bangkok,

10900, Thailand.

Phone: (662) 562-5444 Ext. 2186

Email: fscipths@ku.ac.th

***Referee Suggestions**

I would like to suggest the following reviewers for your consideration.

Reviewer	Institution	e-mail
Prof. Sining Yun	Functional Materials Laboratory (FML), School of Materials & Mineral Resources, Xi'an University of Architecture and Technology, Xi'an, Shaanxi, 710055, China	yunsining@xauat.edu.cn
Prof. Longwei Yin	Key Laboratory for Liquid-Solid Structural Evolution and Processing of Materials, Ministry of Education, School of Materials Science and Engineering, Shandong University, Jinan 250061, PR China	yinlw@sdu.edu.cn
Prof. Chien-Kuo Hsieh	Department of Materials Engineering, Ming Chi University of Technology, 84 Gungjuan Rd., Taishan Dist., New Taipei City 24301, Taiwan, ROC.	jack_hsieh@mail.mcut.edu.tw
Prof. Jae Su Yu	Department of Electronics and Radio Engineering, Institute for Wearable Convergence Electronics, Kyung Hee University, 1 Seocheon-dong, Giheung-gu, Yongin-si, Gyeonggi-do 446-701, Republic of Korea	jsyu@khu.ac.kr
Prof. Qiu-Ping Luo	Laboratory of Optical Information Technology, School of Science, Wuhan Institute of Technology, Wuhan 430205, China	lqp_lzu@163.com
Prof. Yuan-Hsiang Yu	Department of Chemistry, Fu Jen Catholic University, New Taipei City 24205, Taiwan	084916@mail.fju.edu.tw

Graphical abstracts

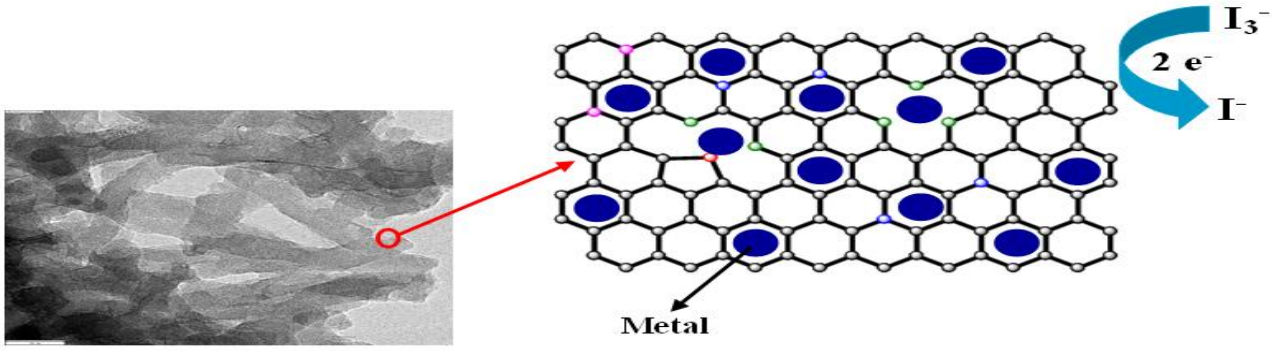

Highlights

- Co or Ni-N-MC is the first alternate design for CE electrocatalyst of DSCs.
- An attempt to couple the CE electrocatalysts and the redox couples is considered.
- Co or Ni-N-MC with high surface area shows excellent electrocatalytic activity.
- DSC with Ni-N-MC CE shows a high efficiency of 8.42% in I^-/I_3^- solution.
- DSC with Ni-N-MC CE shows a high efficiency of 6.95% in T_2/T^- solution.

Economical Nanocomposites of Cobalt or Nickel Species and Polyaniline-Derived N-Doped Mesoporous Carbons for Dye-Sensitized Solar Cells as Counter Electrodes

Panitat Hasin [a,*] , *Vittaya Amornkitbamrung* [b], *Narong Chanlek* [c]

[a] Department of Chemistry and Center of Excellence for Innovation in Chemistry, Faculty of Science, Kasetsart University, Bangkok 10900, Thailand

[b] Department of Physics, Faculty of Science, Khon Kaen University, Khon Kaen 40002, Thailand

[c] Synchrotron Light Research Institute, Nakhon Ratchasima 30000, Thailand

* Email: fscipths@ku.ac.th

*Phone: (662) 562-5444 Ext. 2186

*Fax: (662) 579-3955

Abstract

Nanocomposites of cobalt or nickel species and N-doped mesoporous carbon (Co-N-MC or Ni-N-MC) were prepared by in situ polymerized mesoporous silica-supported polyaniline (PANI) and then explored as the counter electrodes (CEs) in dye-sensitized solar cells (DSCs). It is shown that Co-N-MC and Ni-N-MC significantly improve the electrocatalytic activity towards the reduction of I_3^- compared to N-MC. These are attributed to combining high electrical conductivity of N-doped mesoporous carbon and high electrocatalytic activity of Co or Ni species into one material. The I^-/I_3^--based DSC using Ni-N-MC CE could reach a cell efficiency of 8.42%, which surpassed the efficiency of the DSC employing traditional platinized CE (8.22%). In addition, all N-doped mesoporous (N-MC (5.90%), Co-N-MC (6.80%), and Ni-N-MC (6.95%)) based DSCs showed the high performance than the cell with a platinized CE (5.25%) for the regeneration of organic redox couple, di-5-(1-methyltetrazole) disulfide/5-mercapto-1-methyltetrazole *N*–tetramethylammonium salt (T_2/T^-).

KEYWORDS: *Nanocomposite; Cobalt or nickel species; Polyaniline-derived N-doped mesoporous carbon; Dye-sensitized solar cell; Counter electrode*

1. Introduction

As one of the most promising photovoltaic devices to convert solar energy to electricity directly, dye-sensitized solar cells (DSCs) have attracted considerable attention over the past several decades due to their low cost, simple assembly, good stability, green feature, and relatively high conversion efficiency.[1, 2] To date, the certified power conversion efficiency (PCE) record of over 10 % has been achieved by DSCs.[3, 4] Typically, the structure of DSCs consists of the photosensitized dye, porous semiconductor photoanode, I^-/I_3^- redox electrolyte, and counter electrode (CE). In DSCs, the role played by the CE is to deliver electrons from external circuit to I^-/I_3^- redox species used as a mediator to regenerate the sensitizer after electron injection in order to complete the light-electricity conversion process.[5] Accordingly, the CE for a well operating DSCs should provide the functions not only as an electron collector with great conductivity but also as an electrocatalyst with superior electrocatalytic ability.

The most common material used as a CE is Pt deposited on F-doped tin oxide (FTO) conductive glass because Pt has already been proven to have high electrical conductivity and excellent electrocatalytic activity for I_3^- reduction.[6, 7] Based on the designed DSCs with high efficiency, Pt is an appropriate material used as a CE. Considering the target of expanding solar generation up to the tetrawatt scale, however, much effort has been made to replace the expensive and instability Pt CE by alternatives with low cost, high stability under corrosive electrolyte, and high electrocatalytic activity in order to achieve the large-scale deployment of DSCs.[8] In particular, carbon-based materials have been one of the most practical candidates for Pt-free CEs because of their low cost, excellent electrical conductivity, good electrocatalytic activity, and high resistance against corrosion.[9, 10]

Recently, several carbonaceous materials have been explored considerably, such as activated carbon[11], carbon black[12], graphite[13], graphene[14], carbon nanotubes[15, 16], bio-derived carbon[17], etc. Compared to bulk carbon materials, mesoporous carbon could offer improvement on PCE which is attracting increasing interests for CE application in DSCs because of its sufficient contact at the electrode/electrolyte interface, large pore volume, tunable pore structure, and continuous electron conduction pathways.[10, 18] Although much progress has been realized, the electrochemical performance of the mesoporous carbon is still a challenge so far, because its electrocatalytic activity could not satisfy the DSCs application demand. Moreover, the weak bonding strength between mesoporous carbon materials and the substrate (FTO glass) limits their use as the CEs in DSCs. These may cause instability and insufficient PCE of DSCs with mesoporous carbon CEs.[19] Doping with heteroatoms, particularly N or O atom is an attractive approach to enhance electrochemical reactivity, electron-transfer properties, and surface hydrophilicity of carbon materials as the CEs for DSCs.[20-22] It was found that N-doped carbon nanomaterials remarkably improve the interfacial charge transfer activity towards I_3^- reduction and enhance charge polarization to increase bonding strength between carbon materials and FTO glass due to the large difference in electronegativity between carbon (χ = 2.55) and nitrogen (χ =3.04).[21, 23, 24] Recent advances in carbon materials also discover that pyridinic and graphitic N states are capable of promoting electrocatalytic activity towards I_3^- reduction due to the weaker adsorption of redox species compared to pyrrolic states.[22] The stronger adsorption between pyrrolic N and redox species leads to the difficulty of I* (absorbed) transformation to I^- (solution) for I_3^- reduction reaction.[22]

Although the introduction of nitrogen on carbon materials is normally carried out by the heat treatment under gaseous nitrogen, ammonia, or hydrogen cyanide atmosphere, the quantity of nitrogen in carbon materials obtained by this route is still low. In this regard, it

would be a significant advancement if an increase of nitrogen content in the carbon materials could be achieved. The carbonization of N-containing aromatic polymers such as polyaniline (PANI)[25-27] and polypyrrole (PPy)[28] has been adopted to prepare N-doped carbon materials owing to their high N/C atomic ratios and high molecular weights, which prevents vaporization of small CN species at high temperatures.[25] This method offers N-containing carbon materials with not only high N content but also high surface area resulting in possibly better electrocatalytic activity.

Furthermore, it is also noted that some early transition metals have been proposed as the potential substitutes for Pt due to their low cost, high electrocatalytic activity, selectivity, and good thermal stability under vigorous conditions.[29-31] However, the transition metal materials generally have the poor electron transport efficiency between particles, resulting in restriction of their electrocatalytic activity for the I_3^- reduction. Thus, rational design of the CE is still challenging to obtain high performance electrocatalyst. Recently, researchers found out that the nanocomposites of transition metal compound-carbon are constructed to combine the advantages of both individual components such as CoS/PEDOT-PSS[32], TiN/carbon black[33], CoS/graphene[34], WS_2/multi-wall carbon nanotube[35], WO_2/mesoporous carbon[36], Co_3O_4/mesoporous carbon[37], and Co_2N mesoporous carbon[37]. Nevertheless, the nanocomposites of cobalt or nickel based compounds on N-doped mesoporous carbon matrix have not been reported as CE electrocatalysts to replace expensive Pt CE.

In this paper, the Co or Ni based compounds imbedded in N-doped mesoporous carbon (Co-N-MC or Ni-N-MC), which can efficiently catalyze I_3^- reduction were prepared by the method of carbonizing PANI and introduced to the DSC system as the novel CE materials. The Co or Ni based compounds incorporated in N-doped mesoporous carbon have superb characteristics such as large surface area, well-developed channel like mesoporous

structure, uniform particle size, narrow pore size distribution (PSD), and large amount of N dopant. These advantages make the obtained nanocomposites the ideal alternatives for CE electrocatalysts. For comparison, the electrocatlytic activity of the nanocomposites of Ni based compounds on N-doped mesoporous carbon matrix rendered the corresponding DSC a high PCE of 8.42%, superior to that of platinized-based one (8.22%) in I^-/I_3^- redox species.

Although the high PCEs of DSCs are achieved via utilizing triiodide/iodide redox couple, there are some major disadvantages such as its corrosive nature towards most metals used as the electrical contacts, partial absorption of visible light, and high vapor pressure.[38] These cause long-term instability and reduction of the opportunity to scale up the module size of DSCs. There are some reports on the disulfide/thiolate redox couple that has the advantages over iodine based electrolyte, such as easy preparation including tuning of redox potential, high transmittance in the visible spectral region, and low corrosiveness.[36, 39] Consequently, this study also explored the solar cell performance based on di-5-(1-methyltetrazole) disulfide/5-mercapto-1-methyltetrazole N-tetramethylammonium salt (T_2/T^-) electrolyte. The electrochemical measurements showed that all N-doped mesoporous carbon CEs had higher electrocatalytic activity in the regeneration of T_2/T^- than platinized CE. This alternate design for CE electrocatalyst demonstrates the combination of excellent properties of the Co or Ni based compounds and N-doped mesoporous carbon to develop low-cost and high-efficiency DSCs.

2 Experimental Section

Synthesis of SBA-15 Mesoporous Silica Functionalized with Alkyldiamine Group[27, 40]

The Co-N-MC and Ni-N-MC were synthesized on the basis of replication through nanocasting of SBA-15 mesoporous silica. To prepare SBA-15 mesoporous silica, 4 g of

Pluronic ® 123 (nonionic triblock copolymer $(PEG)_{20}(PPG)_{70}(PEG)_{20}$) was dissolved in a solution of 20 mL of conc. HCl and 130 mL of deionized water. After the chemicals were dissolved under magnetic stirring, 8.5 g of tetraethyl orthosilicate (TEOS) was added and the reaction mixture was heated at 45 °C for 20 h. The as-prepared mesostructured silica was kept in an oven at 80 °C for 24 h as well as was retrieved by centrifugation, washed copiously with distilled water, and dried at room temperature. After this, the modification of external surface of the as-prepared mesostructured silica with trimethylsilyl ($-SiMe_3$) group was carried out (before template extraction started) by stirring 4 g of the obtained powder in hexamethyldiazane (HMDS)/toluene (5 mL/60 mL) solution for 18 h. Then, the Pluronic ® 123 template was subsequently removed by stirring 0.5 g of $SiMe_3$-functionalized mesostructured silica in a mixture of 50 mL of diethyl ether and 50 mL of ethanol for 5 h. After complete removal of template, 0.1 g of the resulting powder was stirred and heated in a mixture of 1.0 mL of *N*-(2-aminoethyl)-3-aminopropyltrimethoxysilane and 100 mL of toluene at 80 °C for 18 h. This makes the inner channel walls of the $SiMe_3$-functionalized mesostructured silica to be coated with alkyldiamine group. After functionalizing the internal surfaces with alkyldiamine group, the solid product was recovered by centrifugation, washed with copious amount of ethanol and dried at room temperature.

Synthesis of Co or Ni based compounds imbedded in N-doped mesoporous carbon (Co-N-MC or Ni-N-MC)[27]

100 mg of SBA-15 mesoporous silica functionalized with alkyldiamine group was stirred in 100 mL of 1.0 M HCl containing 600 mg of sodium persulfate for 2 h before recovering by centrifugation and washing with distilled water to remove any residual persulfate ions. The polymerization of aniline in the pore of SBA-15 mesoporous silica functionalized with alkyldiamine group was conducted as follows: 100 mg of the obtained powder after treating with persulfate ions was mixed with a solution containing 150 µL of

aniline and 10 mL of 1.0 M HCl in an ice bath (0-5 °C) under vigorous stirring for 4 h. The color of the solution was changed from white to green during aniline polymerization. After washing with acetone:ethanol (1:1 ratio), the resulting solid material was treated in 10 mL of 1.0 M ammonia solution under vigorous stirring for 2 h.

Cobalt(II) or nickel(II) ion was doped in the polyaniline (PANI) within the pores of SBA-15 according to the following procedure: the obtained solid material (100 mg) was vigorously stirred in 4 mL of 0.1 M $Co(NO_3)_2.6H_2O$ or $Ni(NO_3)_2.6H_2O$ aqueous solution for 6 h. The black product was washed with ethanol to remove any metal ions that are not electrostatically immobilized on it and dried at room temperature.

To pyrolyze the PANI doped with metal within the pores of SBA-15, the resultant sample was put into a quartz tube. The tube was purged under Ar for 1 h to get an inert atmosphere. Then, the sample was heated to 200 °C with a rate of 1 °C/min and kept for 2 h, and then for 2 h at 300 °C. After that, the temperature was increased once again to 800 °C with a rate of 10 °C/min and kept for 2 h. Then, it was cooled down naturally. The whole procedure was performed under constant Ar gas flow. Finally, Co-N-MC or Ni-N-MC electrocatalyst was obtained after removal of SBA-15 mesoporous silica template by etching in 1.0 M NaOH solution (~1 μg/mL) for 6 h at 100 °C.

Synthesis of N-doped mesoporous carbon (N-MC)[27]

N-MC was synthesized using the same method as mentioned above without doping the metal ions.

Electrodes Fabrication and Cells Assembly

A layer of TiO_2 sensitized by N719 (Solaronix SA, Switzerland) was used as a photoanode. N-MC, Co-N-MC, Ni-N-MC, and platinized electrodes were, each in turn, used as the counter electrodes. The redox couples in the electrolyte were triiodide/iodide and T_2/T^-

. The details of the electrodes fabrication and cells assembly are listed in the Supporting Information section.

Measurements

The X-ray diffraction (XRD) measurements were carried out with an X-ray diffractometer (Bruker D8 ADVANCE). The images of surface morphologies and the energy-dispersive spectrometry (EDS) spectra were acquired by scanning electron microscope (SEM) with JEOL JSM-5600LV and transmission electron microscope (TEM) with JEOL JEM-2011 F operated at 200 kV. The metal content in each sample was determined by atomic absorption spectroscopy (AAS; Varian Model AA280FS). The Raman spectra were measured by a confocal Raman microscope (Bruker Optics, 532 nm argon ion laser). Surface area and pore characteristics were measured by recording N_2 adsorption and desorption isotherms at 77 K using a Quantachrome® ASiQwin Automated Gas Sorption Autosorb Analyzer. Specific surface areas of the samples were calculated from nitrogen adsorption data in the relative pressure range from 0.05 to 0.2 using Brunauer–Emmett–Teller (BET) equation. Total pore volumes were analyzed from the amount of gas adsorbed at the relative pressure of 0.99. Pore-size distribution (PSD) was determined from adsorption branches by Barrett–Joyner–Halenda (BJH) method. The elemental composition and their bonding properties were determined by an X-ray photoelectron spectroscopy using synchrotron radiation from beamline no. 3.2 at the Synchrotron Light Research Institute, Thailand. Cyclic voltammetry (CV) was performed with a three-electrode system to study the electrocatalytic ability of the CEs. The scanning potential range was from −0.4 to 0.7 V at a scan rate of 50 mV s^{-1} by using potentiostat (Metrohm Autolab). A Pt served as a counter electrode and Ag/AgCl electrode served as a reference electrode. The electrolyte solution contained 0.1 M I_2, 0.1 M LiI, 0.6 M tetrabutylammonium iodide, and 0.5 M 4-tertbutylpyridine (TBP) in an argon-purged acetonitrile. Electrochemical impedance spectroscopy (EIS) experiments were

conducted with a traditional CE symmetrical cell by using Autolab Potentiostat PGSTAT 302 with FRA module. The measured frequency was in the range of 100 mHz to 1 MHz, and the AC amplitude was set at 10 mV. The bias was 0 V. Photovoltaic performance of the DSCs was measured with simulated AM 1.5 illumination from the Xenon arc lamp (100 mW cm^{-2}) with a Keithley 236 source-measure unit. A black mask was applied on the surface of DSCs to avoid stray light, and all solar cell tests were performed at room temperature.

3. Results and Discussion

3.1 Material Characterization

Figure 1 presents the XRD patterns of the prepared Co-N-MC and Ni-N-MC nanocomposites. In the XRD pattern of Co-N-MC composite (Figure 1 (a)), the three sharp diffraction peaks (circle label) can be indexed to the well-crystallized Co (JCPDS 15-0806), and other three obvious diffraction peaks (square label) identify that CoO (JCPDS 74-2392) is also present in the Co-N-MC composite. For Ni-N-MC composite, the intensity diffraction peaks at 2θ values of about 37.2, 43.3, and 62.8° in the XRD pattern (Figure 1(b)) are attributed to crystalline NiO (JCPDS 65-6920). Besides NiO, the other peak positions presented in the XRD pattern of Ni-N-MC composite can be indexed to those of $Ni(OH)_2$ (JCPDS 02-1112) and Ni (JCPDS 04-0850). Therefore, we can say that Co or Ni compounds imbedded in N-doped mesoporous carbons have been successfully synthesized. The average Co and NiO particle sizes are estimated using the Scherrer equation $d = 0.89\lambda/\beta \cdot \cos\theta$, where d is the average crystallite size of the Co and NiO, λ is the X-ray wavelength (Cu Kα, λ= 0.154 nm), β is the half-peak width for Co and NiO peaks in radians, and θ is the diffraction angle of Co (2θ = 44.2°) and NiO (2θ = 43.3°) peaks. The calculated average crystallite sizes of Co and NiO are 56.0 and 54.9 nm for Co-N-MC and Ni-N-MC, respectively. The structure and particle dispersion of the samples were further investigated by TEM analysis.

The crystallite structure of the carbons was characterized by XRD. The diffraction peak at $2\theta \approx 27°$ observed in the XRD patterns of all samples corresponds to the (002) diffraction of crystalline carbon as displayed in Figure 2. Although the culminating points of diffraction peak (002) related to graphitic carbon are similar for all samples, the shape of diffraction peaks (002) becomes sharper along with the addition of Co or Ni species. Then, the addition of Co or Ni species in N-doped mesoporous carbon is proved to cause an improved graphitic crystallinity. Moreover, it is also known that the (002) diffraction of the graphite structure is centered at 2θ of 26° and its interlayer spacing ($d_{(002)}$) is 0.336 nm. In our results, the interlayer spacing ($d_{(002)}$) of both Co-N-MC and Ni-N-MC was calculated to be 0.334 nm which was similar to that of graphite. This indicates a highly graphitic crystallinity resulting in excellent electrical conductivity. Consequently, the graphitic carbon structure in both synthesized nanocomposites might be theoretically beneficial for CE electrocatalysts in DSCs.

The microstructures of the Co-N-MC and Ni-N-MC electrocatalysts were examined by scanning electron microscopy (SEM) and transmission electron microscopy (TEM). The SEM images in Figure 3(b) – Figure 3(c) show that the microstructure of mesoporous carbons has the linear array of connected rod-like particles with a diameter of 30 - 70 nm and 500 – 750 nm long. This observation indicates that mesoporous carbon has been successfully synthesized because the obtained nanocomposites have similar geometric morphology to the original SBA-15 used as a template (Figure 3(a)).

Figure 4. shows the energy-dispersive X-ray spectroscopy (EDX) analysis of Co-N-MC and Ni-N-MC, disclosing the existence of Co and Ni, respectively in the nanocomposites.

Values of the Co and Ni contents of each sample were determined using atomic absorption spectrophotometry (AAS), after acid digestion of the samples. The synthesized

Co-N-MC contained 3.28 mmol/g of Co (19.30 Wt.%) and the Ni-N-MC contained 5.66 mmol/g of Ni (33.27 Wt.%).

The TEM images in Figure 5 show that these nanocomposites are comprised of randomly oriented fibers retaining well rod-like morphology of the SBA-15 template. This observation is in good agreement with the corresponding SEM images. Furthermore, the TEM images of the metal-N-MC (Figure 5(b) – Figure 5(c)) also display the homogeneous distribution of Co or Ni-based nanoparticles with average particle size of ca. 50 nm throughout the frameworks of N-MC, confirming the formation of Co and Ni species imbedded in N-MC supports. The particle sizes of the metal compounds obtained from TEM images are consistent with the values calculated from the Scherrer equation. The observation from TEM measurement also suggests that the particles with small sizes of metal compounds uniformly decorated onto the mesoporous carbon support can be attributed to effective confinement of mesoporous carbon structure towards growth process for particles of metal compounds. Moreover, it has been demonstrated by many studies that N species doped in carbon materials will act as localized defects which can provide initial nucleation sites for immobilizing nanoparticles. The presence of N species also helps dispersing particles of metal compounds on carbon support and avoids surface metal aggregation, thus achieving homogeneous dispersion of nanoperticles with small sizes on mesoporous carbon support.[41, 42] To further provide useful information about the nanoparticles in the composites, HRTEM images are also demonstrated in Figure 5(d) – Figure 5(e). It is obvious in magnifying images that Co and Ni-based compounds possess the well-crystallized structures. The lattice fringes of Co and Ni-based compounds with measured interplanar spacings of 0.20 nm (Figure 5(d)) and 0.21 nm (Figure 5(e)) are clearly observed, corresponding to the interplanar distances of cubic crystal metallic cobalt (111) facet and cubic crystal nickel oxide (200) facet, respectively. This can confirm the results analyzed by XRD. In addition, the well-defined

crystalline lattice spacing between carbon layers is also measured to be 0.33 nm for both samples, which matches well with the (002) plane of the typical graphite phase. This phenomenon indicates that the degree of graphitization can be improved by Co or Ni-based nanoparticles which can be confirmed by XRD results.

Raman measurement was conducted to identify carbon phases and structural defects. In first order Raman spectra for N-MC, Co-N-MC, and Ni-N-MC (shown in Figure 6), there are two peaks apparent in the spectra for all three samples, corresponding to the D- and G-bands at the vibration of 1355 cm^{-1} and 1580 cm^{-1}, respectively. The D band clearly demonstrates the existence of disorders or vibrational of sp^3 hybridized carbon atoms in the carbon materials.[43] The G band is associated with sp^2 hybridized carbon atoms (graphitic sheet) presenting in all carbon materials which arises from the E_{2g} vibrational mode. The relative area under the peak for the D band and G band, I_D/I_G value, is determined to be proportional to the ratio of defect sites to graphitic structure of carbon materials. The decrease of I_D/I_G value is indicative of improving degree of graphitization.[44, 45] As shown in Figure 6, I_D/I_G values were estimated at 1.56 for N-MC, 1.43 for Co-N-MC, and 1.09 for Ni-N-MC which were decreased monotonically along with the incorporation of Co and Ni species. This suggests that the graphitization degree of carbon samples can be enhanced with the addition of Co and Ni species because the metal dopants have catalytically graphitized the partly amorphous carbon during thermal treatment. This leads to a better graphitic crystallinity and electron conductivity of carbon composites. This result is in good agreement with those from XRD and HRTEM data.

The surface area, pore volume and mean pore size for the N-MC, Co-N-MC, and Ni-N-MC measured by nitrogen porosimetry are shown in Table 1. The surface areas for Co-N-MC and Ni-N-MC are 101 and 218 m^2/g, respectively, which are significantly higher than

that of N-MC (35 m^2/g). The nitrogen adsorption-desorption isotherms of all samples shown in Figure 7. exhibit type IV isotherms, with distinct hysteresis loop at the relative pressure (P/P_0) range of 0.40 to 0.70, which is due to the capillary condensation of nitrogen in the mesoporous texture.[46, 47] The mesopore size distribution was centered at 3.8 nm for Co-N-MC and Ni-N-MC, respectively, according to the Barrett–Joyer–Halenda (BJH) model (insets in Figure7(a) – Figure 7(b)), exhibiting narrow pore-size distribution. The pore-size distribution curve of N-MC, however, showed a broad pore size distribution which was centered at 6.5 and 9.5 nm (inset in Figure 7(a)). As concluded in Table 1, the N-MC obtained the smallest structure parameter, suggesting a greater shrinkage during the heat treatment. Nevertheless, the total pore volumes of the Co-N-MC (0.30 cm^2/g) and Ni-N-OMC (0.48 cm^2/g) are larger than that of N-MC (0.23 cm^2/g), which indicates that Co and Ni species can mechanically strengthen framework and decrease contraction during carbonization.

X-ray photoelectron spectroscopy (XPS) analyses were used to investigate and compare the surface electron states properties of carbon, nitrogen, cobalt, and nickel species in materials. The HR C 1s XPS spectra are depicted in Figure 8(a). C 1s spectra of three samples presented in Figure 8(a) can be deconvoluted to several single peaks corresponding to C-C=C (284.3 eV; labeled as I)[48], C-O/C-N (286.0 eV; labeled as II), and C=O (286.9 eV; labeled as III), indicating the existence of heteroatoms in composites.[49] The atomic percentage ratios of C-C=C/C-O, C=O in the N-MC, Co-N-MC, and Ni-N-MC samples determined from the peak area of C 1s are founded to be 1.40, 1.61, and 2.53, respectively (Figure 8(b)). The C-C=C contents in Co-N-MC and Ni-N-MC composites are much higher than that in bared N-MC sample, which is attributed to the efficiency of transition metal towards carbonization process. The content of C-C=C increases upon the addition of Co or Ni

species in carbon framework implying the improvement of electronic conductivity and fast electron transfer throughout the structural framework

The binding energy peaks observed in the HR N 1s spectra shown in Figure 9(b) can be fitted into three peaks at 398.3, 400.1, and 401.2 eV, which are attributed to the pyridine-like nitrogen atoms[50], pyrrolic-like nitrogen atoms[51, 52], and graphitic nitrogen atoms[53], respectively (Figure 9(a)). This suggests that nitrogen was successfully doped into carbon framework. In addition, the total concentrations of pyridinic and graphitic N determined based on the integrated peak areas are 53%, 63%, and 67% for N-MC, Co-N-MC, and Ni-N-MC, respectively (Figure 9(c)). It was previously reported that both pyridinic and graphitic N functionalities may provide effective electrocatalytic active sites.[22, 54] Consequently, the increased pyridinic and graphitic N contents are expected to improve the electrocatalytic performance towards I_3^- reduction of Co-N-MC and Ni-N-MC.

In addition, the high-magnification XPS spectra in the Co 2p region of Co-N-MC and Ni 2p region of Ni-N-MC are also used to further confirm the composition of the obtained products (Figure 10). The Co $2p_{3/2}$ peaks of Co-N-MC at 778.5 and 779.7 eV (Figure 10(a)) are attributed to Co^0 and Co^{2+}, respectively.[55-57] For Ni-N-MC, the Ni $2p_{3/2}$ region (Figure 10(b)) exhibits a small peak at binding energy of 852.6 eV which can be attributed to Ni^0 while the peak located at 854.0 eV is ascribed to Ni^{2+}.[58, 59] Therefore, all of the results clearly confirm the formation of Co and CoO in Co-N-MC as well as Ni, NiO, and $Ni(OH)_2$ in Ni-N-MC. These findings agree well with the XRD and HRTEM results.

3.2 Electrocatalytic Activity Characterization.

The CE is an important component impacting the performance of the DSCs. To regenerate the tri-iodide/iodide redox species with a minimum energy loss, the CE electrocatalyst should be modified to enhance the electrical conductivity, the specific surface

area, and the electrocatalytic activity.[5, 60] CV is a powerful tool to understand the electrocatalytic properties for N-doped mesoporous carbon immobilized by Co or Ni species. As shown in Figure 11, all electrodes show very well-resolved CV profiles with a pair of current peaks in CVs, exhibiting the electrocatalytic activity for I_3^-/I^- redox couple. The Ni-N-MC and Co-N-MC electrodes show a pair of current peaks similar to the platinized electrode, while N-MC electrode exhibits less intense current peaks. This suggests that the Co and Ni species immobilized on N-doped mesoporous carbons contribute to the electrocatalytic performance of the Co-N-MC and Ni-N-MC electrodes, respectively by providing more exposed active sites for accelerating the I_3^-/I^- redox reaction at the electrode-electrolyte interface.[61, 62] Moreover, the superior electrocatalytic activity of the Co-N-MC and Ni-N-MC electrodes is also consistent with the efficient charge transport and transfer rates during the electrocatalytic reaction process. These are attributed to both high pyridinic and graphitic N contents to provide sufficient electrocatalytic active sites as well as large surface area to facilitate electrolyte penetration. In comparison with the Ni-N-MC and Co-N-MC electrodes, the N-MC electrode has the smallest current peaks due to the lack of conductive mesoporous carbon matrix resulting in less efficient charge transport.

In addition to the current peak, the peak potential separation (ΔE_p) between the anodic and cathodic peaks is also used to determine the rate of interfacial charge transfer between the electrolyte and the electrode. ΔE_p is inversely proportional to the rate of an electrochemical reaction. As compared with platinized, Ni-N-MC, and Co-N-MC electrodes, the anodic peak of N-MC electrode appears at a relative positive potential (0.450 V vs Ag/Ag^+, the same applies hereinafter), along with the cathodic peak, which appears at a negative potential (-0.029 V) leading to the largest ΔE_p value (Figure 11). This indicates a relatively large charge-transfer resistance implying a low reversibility of the I_3^-/I^- redox reaction when N-MC is used as an electrocatalyst. For the N-doped mesoporous electrodes

with imbedding Co or Ni species, the cathodic peaks tend towards positive (0.103 V for Co-N-MC and 0.096 V for Ni-N-MC), whereas the anodic peaks tend towards negative (0.391 V for Co-N-MC and 0.406 V for Ni-N-MC), in contrast with N-MC electrode. This demonstrates that the electrocatalytic performance is improved by immobilizing Co or Ni species into N-MC because of their reversibility. Although the Co-N-MC and Ni-N-MC electrodes have similar current peaks and ΔE_p values to the platinized electrode, the electrocatalytic performance/cost is still higher than that of platinized electrode. In brief, the Co-N-MC and Ni-N-MC nanocomposites are advantageous as the potential low cost electrocatalysts for CEs in DSCs to replace the conventional and expensive Pt CE.

Chronoamperometry (CA) is an effective technique for investigating the mass transport of the redox couple in the bulk electrolyte solution and also within the structurally porous electrode as well as thereby for evaluating the electrocatalytic activity of an electrocatalyst. Particularly, it is more serious for mesoporous carbon which generally suffered from limited electrolyte diffusion and penetration through its pore.[63] The mass transport properties of I_3^- in our mesoporous carbon electrodes are more accurately characterized by chronoamperometry (CA) at room temperature (Figure 12). As expected from the semi-infinite Cottrell decay,[64] the observed current dropped linearly as $t^{-1/2}$ (t is time). The diffusion coefficient (D) can be calculated from the transition time (t) obtained by the extrapolation of both linear components of the chronoamperometric plot according to the eqs 1 and 2, where δ is the distance between electrodes.

$$\frac{n\,FAC.\sqrt{D}}{\sqrt{\pi\,t}} = \frac{2n\,FAC.D}{\delta} \quad (1)$$

$$D = t^{-1}\left(\frac{\delta^2}{4\pi}\right) \quad (2)$$

From the data in Figure 12 and eq 2, the *D* value can be calculated and was found to be ca. 1.1×10^{-5} cm^2/s (δ = 60 μm) for both all mesoporous carbons and platinized dummy cells in our system. Obviously, the obtained value is a reasonable agreement with values from the literature.[65] The limiting current of the Ni-N-MC was, however, slightly higher than that of platinized electrode. The higher limiting current of Ni-N-MC cell is mainly due to the enlargement of the surface area resulting in the enhancement of the mass transport for the redox couple within the structurally porous electrode.

To validate the electrochemical performance of CEs for DSC application, EIS using symmetrical cells with two identical CEs was carried out.[66] Figure 13(a) depicts the Nyquist plots of the symmetrical cells employing platinized, N-MC, Co-N-MC, and Ni-N-MC electrodes. Figure 13(b) gives a typical equivalent circuit used to fit the EIS spectra by using ZView software in order to obtain the electrochemical parameters. In a Nyquist plot, the ohmic process reflected by series resistance (R_s) can be obtained from the intercept on the real axis (Z') in high frequency end. This may include the contributions from the sheet resistance of FTO as well as the interfacial contact resistance between FTO and electrocatalyst layer and/or between individual electrocatalyst materials. In EIS spectra, there are two distinct characteristic semicircles. The left semicircle in high-frequency region can be attributed to the resistance capacitance (RC) networks of the electrode/electrolyte interface, including the charge-transfer resistance (R_{ct}) in parallel with the electric double layer capacitor (C_μ). For modeling porous electrodes, C_μ is generally replaced by a constant phase element (CPE) for non-ideal capacitor. The right semicircle in the low-frequency region can be assigned to the diffusion process of I^-/I_3^- species in the cell, which can be characterized by typical Nernst diffusion impedance (Z_N).[65] The EIS data were summarized in Table 2. Due to the high electrical conductivity of Pt electrocatalyst, the R_s value of cell using platinized electrode (25.2 Ω) is slightly lower than those of cells using N-MC (30.4 Ω), Co-N-MC (26.9

Ω), and Ni-N-MC (26.6 Ω) electrodes. The higher R_s values for all mesoporous carbon electrodes are resulting from large numbers of grain boundaries between the carbon nanoparticles. Among the N-doped mesoporous carbon electrodes, the decrease of R_s values was observed for Co-N-MC and Ni-N-MC electrodes, which may be attributed to the addition of Co and Ni compound nanoparticles that enhanced the graphitization degree of the Co-N-MC and Ni-N-MC composites, respectively. The R_{ct} values of Co-N-MC and Ni-N-MC are 4.6 and 3.8 Ω cm^2, respectively, which are lower than that of cell using N-MC (6.3 Ω cm^2), clearly demonstrating metal-doping effect. Moreover, the R_{ct} value of Ni-N-MC electrode is also lower than that of cell using platinized electrode (4.7 Ω cm^2). The results are in good agreement with the cyclic voltammetry revealing that the Ni-N-MC electrode exhibits higher electrocatalytic ability for I^-/I_3^- couple. Furthermore, the C_μ values of all mesoporous carbon samples (Ni-N-MC = 49.8 μF cm^{-2}, Co-N-MC = 42.7 μF cm^{-2}, and N-MC = 34.6 μF cm^{-2}) are significantly larger than that of platinized electrode (5.8 μF cm^{-2}) and the highest C_μ value of Ni-N-MC nanocomposite is observed as well. The enhanced capacitance at the Ni-N-MC-electrolyte interface can be attributed to the large surface area and pore volume in the Ni-N-MC which is consistent with the results from nitrogen adsorption/desorption isotherms.

To evaluate the electrochemical stability of the sample electrodes, the EIS of these CEs is measured with varying CV cycles at room temperature. With increasing the scan numbers of CV cycles under cycling potential between −1.0 and 1.0 V in I^-/I_3^- solution in acetonitrile, the variation curves of Nyquist plots for both platinized and Ni-N-MC electrodes assembled in the dummy cell compartment are shown in Figure 14(a) and Figure 14(b), respectively. The R_{ct} value for the freshly platinized electrode was initially 4.7 Ω cm^2 but it was increased to 9.2 Ω cm^2 in the final cycle. On the contrary, the freshly assembled Ni-N-MC electrode exhibited the R_{ct} value of 3.8 Ω cm^2 in the first cycle and it was slightly increased up to 4.3 Ω cm^2 after 10 times. As shown in Figure 14(c), the much slower and

milder deterioration of Ni-N-MC than platinized electrode clearly demonstrate that the Ni-N-MC had better electrochemical stability in I^-/I_3^- medium.

3.3 Photovoltaic Performances of the DSCs using Platinized, N-MC, Co-N-MC, and Ni-N-MC Counter Electrodes for Triiodide/Iodide and T_2/T^- Redox Couples.

To determine the effect of replacing Pt on the photovoltaic performance in DSC devices, the current-voltage characteristics of the DSCs fabricated with various CEs are analyzed at one sun of illumination as shown in Figure 15 and summarized in Table 3. All DSCs exhibit photovoltaic effect for converting light into electrical current with I^-/I_3^- redox couple as displayed in Figure 15(a). As compared with the DSC using N-MC CE, the short-circuit current densities (J_{sc}) of the DSCs using Co-N-MC and Ni-N-MC CEs are improved from 14.2 to 15.0 and 16.6 mA cm^{-2}, fill factors (FF) are improved from 0.62 to 0.70, and the power conversion efficiency (η) values are improved from 7.10 to 7.57 and 8.42 %, respectively. The lower degree of graphitization (as the Raman measurements confirm) and lower electrocatalytic performance (as the CV experiments confirm) of N-MC CE give rise to a significantly decrease in the J_{sc} and FF values resulting in lower η value of DSC. The incorporation of metal compound nanoparticles into N-doped mesoporous carbon is indispensable for facilitating the heterogeneous electron-transfer process at the CE/electrolyte interface which is evident from the smaller value of R_{ct}. Moreover, the large surface area and wide pore volume including pore size of metal species immobilized on N-doped mesoporus carbon give also rise to high transport rate of electrolyte species. As shown in Table 3, both the open-circuit voltage (V_{oc}) and FF values of Ni-N-MC-based DSC (V_{oc} = 0.73 V, FF = 0.70) are slightly higher than those of platinized-based DSC (V_{oc} = 0.70 V, FF = 0.66) leading to the improvement of the overall cell performance (8.42 % for Ni-N-MC CE and 8.22% for platinized CE). The superior cell performance of Ni-N-MC based-DSC can be attributed to the high electrocatalytic activity as indicated by high pyridinic and graphitic N contents

combined with the feasibility of the charge-transfer process as indicated by the small R_{ct} value. Therefore, these make Ni-N-MC applicable to the large-scale DSC application.

In the case of di-5-(1-methyltetrazole) disulfide/5-mercapto-1-methyltetrazole *N*-tetramethyl-ammonium salt redox couple (T_2/T^-, Figure S1 of the Supporting Information),[36, 39] Figure 15(b) shows the *J*–*V* curves of the N-MC, Co-N-MC, Ni-N-MC, and platinized-based DSCs with T_2/T^-, as a redox couple. The platinized-based DSC shows a J_{sc} of 16.6 mA cm^{-2}, a V_{oc} of 0.70 V, a FF of 0.45, and a η of 5.25%. When the CE was changed from platinized CE to all N-doped mesoporous carbon CEs, the FF values were improved significantly to 0.53, 0.60, and 0.62 for N-MC, Co-N-MC, and Ni-N-MC, respectively. Consequently, the η of DSCs based on all N-doped mesoporous carbon CEs increased to 5.90, 6.80, and 6.95 % for DSCs using N-MC, Co-N-MC, and Ni-N-MC, respectively. Interestingly, unlike in the case of I^-/I_3^- redox couple, all N-doped mesoporous carbon CEs show higher electrocatalytic activity than platinized CE for the regeneration of T_2/T^- redox couple. This implies an ease or efficiency of the interfacial electron transfer reaction towards T_2/T^- redox couple at the interfaces between all N-doped mesoporous carbons and electrolyte. Therefore, it is highly desirable to match the appropriate CE electrocatalysts to the redox couple in order to achieve optimum devices.[28, 36]

To further examine the electrocatalytic activity of N-MC, Co-N-MC, Ni-N-MC, and platinized electrodes with T_2/T^- redox couple, EIS experiments of dummy cells were carried out similarly, as previously discussed for the reduction of I^-/I_3^- redox system. Figure 16 shows the Nyquist plots of the N-MC, Co-N-MC, Ni-N-MC, and platinized symmetrically cells and EIS parameters are summarized in Table 2. The value of R_{ct} of the platinized (44.2 Ω cm^2) dummy cell is much larger than those of the N-MC (21.3 Ω cm^2), Co-N-MC (16.0 Ω cm^2), and Ni-N-MC (14.4 Ω cm^2) dummy cells. This implies the enhanced power photovoltaic performance of the DSCs using N-MC, Co-N-MC, and Ni-N-MC CEs with

T_2/T^- redox couple. However, the DSCs operating under T_2/T^- redox couple have higher R_{ct} values than those operating under I^-/I_3^- redox system, resulting in the lower photovoltaic performance. The higher R_{ct} values for the reduction of T_2 to T^- are due to the impediment of the electrolyte transport in the narrow pore channels inside the carbon matrix, leading to the increased mass-transfer resistance and slow diffusion of T_2/T^- redox couple. As an evident, the increase in impedance is observed in the low-frequency semicircle for T_2/T^- redox couple.

4. Conclusions

In summary, the synthesized Co or Ni species immobilized on N-doped mesoporous carbon (Co-N-MC or Ni-N-MC) with high surface area showed excellent electrocatalytic activity towards the electrochemical reduction of triiodide in DSC systems as compared with N-doped mesoporous carbon (N-MC). The predominating contents of pyridinic and quaternary N species over pyrrolic N as well as good electrical conductivity in the Co-N-MC and Ni-N-MC frameworks are considered to contribute positively on the photoelectric conversion efficiency of DSCs. Moreover, the improvement of photovoltaic performance can also be ascribed to a much lower charge-transfer resistance (R_{ct}) related to superb structural surface properties and metal-doping of the Co-N-MC and Ni-N-MC. Compared to the DSC employing platinized counter electrode (FF = 0.66 and η = 8.22%), the fill factor (FF) and photoelectric conversion efficiency (η) of DSC employing Ni-N-MC counter electrode (FF = 0.70 and η = 8.42%) were higher. Furthermore, the Ni-N-MC electrode that was experienced 10 CV cycles also showed good electrochemical stability. In addition, N-MC, Co-N-MC, and Ni-N-MC all preformed better than platinized electrode in catalyzing the T_2/T^- organic redox system. The combination of electrocatalytic Co or Ni species and N-doped mesoporous carbon matrix is an alternative design for counter electrode electrocalyst to reduce the cost of DSCs. Last but not least, in the fabrication procedure of DSCs, an attempt to couple the suitable counter electrode electrocatalysts and the redox couples should also be considered.

Acknowledgements

This research was supported by The Thailand Research Fund (TRF) and Kasetsart University Research and Development Institute (KURDI) under contract number (TRG5780227). This work also supported by Department of Chemistry, and the Center of Excellence for Innovation in Chemistry (PERCH-CIC) and Faculty of Science at Kasetsart University. In addition, the authors gratefully thank to the SUT-NANOTEC-SLRI Joint Research Facility for XPS facility

Appendix A. Supplementary material

Preparation of N-MC, Co-N-MC, Ni-N-MC, and platinized counter electrodes, symmetrical dummy cells for electrochemical impedance spectroscopy (EIS), preparation of photoanode and cells fabrication, chemical structure of the redox couple of disulfide/thiolate (T_2/T^-)

References

[1] B. O'REGAN and M. GRÄTZEL, Nature 353 (1991) 737-740.

[2] A. Hagfeldt, G. Boschloo, L.C. Sun, L. Kloo and H. Pettersson, Chemical Reviews 110 (2010) 6595-6663.

[3] Y. Chiba, A. Islam, Y. Watanabe, R. Komiya, N. Koide and L.Y. Han, Japanese Journal of Applied Physics Part 2-Letters & Express Letters 45 (2006) L638-L640.

[4] W.D. Zeng, Y.M. Cao, Y. Bai, Y.H. Wang, Y.S. Shi, M. Zhang, F.F. Wang, C.Y. Pan and P. Wang, Chemistry of Materials 22 (2010) 1915-1925.

[5] N. Papageorgiou, Coordination Chemistry Reviews 248 (2004) 1421-1446.

[6] T.L. Ma, X.M. Fang, M. Akiyama, K. Inoue, H. Noma and E. Abe, Journal of Electroanalytical Chemistry 574 (2004) 77-83.

[7] G. Calogero, P. Calandra, A. Irrera, A. Sinopoli, I. Citro and G. Di Marco, Energy & Environmental Science 4 (2011) 1838-1844.

[8] E. Oslen, G. Hagen and S.E. Linquist, Sol. Energy Mater. Sol. Cells 63 (2000) 267.

[9] Andreas Kay and M. Gratzel, Solar Energy Materials and Solar Cells 44 (1996) 99-117.

[10] E. Ramasamy and J. Lee, Carbon 48 (2010) 3715-3720.

[11] K. Imoto, K. Takahashi, T. Yamaguchi, T. Komura, J. Nakamura and K. Murata, Solar Energy Materials and Solar Cells 79 (2003) 459-469.

[12] T.N. Murakami, S. Ito, Q. Wang, M.K. Nazeeruddin, T. Bessho, I. Cesar, P. Liska, R. Humphry-Baker, P. Comte, P. Pechy and M. Gratzel, Journal of the Electrochemical Society 153 (2006) A2255-a2261.

[13] G. Veerappan, K. Bojan and S.W. Rhee, Acs Applied Materials & Interfaces 3 (2011) 857-862.

[14] D.W. Zhang, X.D. Li, H.B. Li, S. Chen, Z. Sun, X.J. Yin and S.M. Huang, Carbon 49 (2011) 5382-5388.

[15] J.E. Trancik, S.C. Barton and J. Hone, Nano Letters 8 (2008) 982-987.

[16] E. Ramasamy, W.J. Lee, D.Y. Lee and J.S. Song, Electrochemistry Communications 10 (2008) 1087-1089.

[17] C.L. Wang, J.Y. Liao, S.H. Chung and A. Manthiram, Advanced Energy Materials 5 (2015).

[18] B.Z. Fang, S.Q. Fan, J.H. Kim, M.S. Kim, M. Kim, N.K. Chaudhari, J. Ko and J.S. Yu, Langmuir 26 (2010) 11238-11243.

[19] M.X. Wu, X. Lin, T.H. Wang, J.S. Qiu and T.L. Ma, Energy & Environmental Science 4 (2011) 2308-2315.

[20] K.S. Lee, W.J. Lee, N.G. Park, S.O. Kim and J.H. Park, Chemical Communications 47 (2011) 4264-4266.

[21] Y.H. Xue, J. Liu, H. Chen, R.G. Wang, D.Q. Li, J. Qu and L.M. Dai, Angewandte Chemie-International Edition 51 (2012) 12124-12127.

[22] S.C. Hou, X. Cai, H.W. Wu, X. Yu, M. Peng, K. Yan and D.C. Zou, Energy & Environmental Science 6 (2013) 3356-3362.

[23] T.N. Murakami and M. Gratzel, Inorganica Chimica Acta 361 (2008) 572-580.

[24] K.P. Gong, F. Du, Z.H. Xia, M. Durstock and L.M. Dai, Science 323 (2009) 760-764.

[25] G. Wu, K.L. More, C.M. Johnston and P. Zelenay, Science 332 (2011) 443-447.

[26] G. Wu, N.H. Mack, W. Gao, S.G. Ma, R.Q. Zhong, J.T. Han, J.K. Baldwin and P. Zelenay, Acs Nano 6 (2012) 9764-9776.

[27] R. Silva, D. Voiry, M. Chhowalla and T. Asefa, Journal of the American Chemical Society 135 (2013) 7823-7826.

[28] D.S. Yang, C. Kim, M.Y. Song, H.Y. Park, J.C. Kim, J.J. Lee, M.J. Ju and J.S. Yu, Journal of Physical Chemistry C 118 (2014) 16694-16702.

[29] M.K. Wang, A.M. Anghel, B. Marsan, N.L.C. Ha, N. Pootrakulchote, S.M. Zakeeruddin and M. Gratzel, Journal of the American Chemical Society 131 (2009) 15976-+.

[30] Q.W. Jiang, G.R. Li and X.P. Gao, Chemical Communications (2009) 6720-6722.

[31] M.X. Wu, X.A. Lin, A. Hagfeldt and T.L. Ma, Angewandte Chemie-International Edition 50 (2011) 3520-3524.

[32] P. Sudhagar, S. Nagarajan, Y.G. Lee, D. Song, T. Son, W. Cho, M. Heo, K. Lee, J. Won and Y.S. Kang, Acs Applied Materials & Interfaces 3 (2011) 1838-1843.

[33] G.R. Li, F. Wang, J. Song, F.Y. Xiong and X.P. Gao, Electrochimica Acta 65 (2012) 216-220.

[34] S. Das, P. Sudhagar, S. Nagarajan, E. Ito, S.Y. Lee, Y.S. Kang and W. Choi, Carbon 50 (2012) 4815-4821.

[35] J.H. Wu, G.T. Yue, Y.M. Xiao, M.L. Huang, J.M. Lin, L.Q. Fan, Z. Lan and J.Y. Lin, Acs Applied Materials & Interfaces 4 (2012) 6530-6536.

[36] M.X. Wu, X. Lin, L. Wang, W. Guo, Y.D. Wang, J.Q. Xiao, A. Hagfeldt and T.L. Ma, Journal of Physical Chemistry C 115 (2011) 22598-22602.

[37] M. Chen, L.L. Shao, Z.M. Gao, T.Z. Ren and Z.Y. Yuan, Journal of Power Sources 286 (2015) 82-90.

[38] H.N. Tian, Z. Yu, A. Hagfeldt, L. Kloo and L. Sun, Journal of the American Chemical Society 133 (2011) 9413-9422.

[39] M.K. Wang, N. Chamberland, L. Breau, J.E. Moser, R. Humphry-Baker, B. Marsan, S.M. Zakeeruddin and M. Gratzel, Nature Chemistry 2 (2010) 385-389.

[40] D. Zhao, J. Feng, Q. Huo, N. Melosh, G.H. Fredrickson, B.F. Chmelka and G.D. Stucky, Science 279 (1998) 548.

[41] S.C. Roy, A.W. Harding, A.E. Russell and K.M. Thomas, Journal of the Electrochemical Society 158 (2011) S3-S3.

[42] B. Yue, Y.W. Ma, H.S. Tao, L.S. Yu, G.Q. Jian, X.Z. Wang, X.S. Wang, Y.N. Lu and Z. Hu, Journal of Materials Chemistry 18 (2008) 1747-1750.

[43] S. Maldonado, S. Morin and K.J. Stevenson, Carbon 44 (2006) 1429-1437.

[44] A.C. Ferrari and J. Robertson, Physical Review B: Condensed Matter and Materials Physics 61 (2000) 14095-14107.

[45] N.Q. Jia, Z.Y. Wang, G.F. Yang, H.B. Shen and L.Z. Zhu, Electrochemistry Communications 9 (2007) 233-238.

[46] S.H. Liu, M.T. Wu, Y.H. Lai, C.C. Chiang, N.Y. Yu and S.B. Liu, Journal of Materials Chemistry 21 (2011) 12489-12496.

[47] T. Wang, C.X. Zhang, X. Sun, Y.X. Guo, H. Guo, J. Tang, H.R. Xue, M.Z. Liu, X.X. Zhang, L. Zhu, Q.Q. Xie and J.P. He, Journal of Power Sources 212 (2012) 1-12.

[48] Y.D. Xia and R. Mokaya, Chemistry of Materials 17 (2005) 1553-1560.

[49] Z.Y. Lin, G. Waller, Y. Liu, M.L. Liu and C.P. Wong, Advanced Energy Materials 2 (2012) 884-888.

[50] J.R. Pels, F. Kapteijn, J.A. Moulijin, Q. Zhu and K.M. Thomas, Carbon 33 (1995) 1641-1653.

[51] S. Delpeux, F. Beguin, R. Benoit, R. Erre, N. Manolova and I. Rashkov, European Polymer Journal 34 (1998) 905-915.

[52] J. Lahaye, G. Nanse, A. Bagreev and V. Strelko, Carbon 37 (1999) 585-590.

[53] D. Hulicova-Jurcakova, M. Seredych, G.Q. Lu and T.J. Bandosz, Advanced Functional Materials 19 (2009) 438-447.

[54] D.S. Yu, Q. Zhang and L.M. Dai, Journal of the American Chemical Society 132 (2010) 15127-15129.

[55] N.S. McIntyre and M.G. Cook, Analytical Chemistry 47 (1975) 2208-2213.

[56] A.B. Mandale, S. Badrinarayanan, S.K. Date and A.P.B. Sinha, Journal of Electron Spectroscopy and Related Phenomena 33 (1984) 67-72.

[57] B.J. Tan, K.J. Klabunde and P.M.A. Sherwood, Journal of the American Chemical Society 113 (1991) 855-861.

[58] M.J. Kenney, M. Gong, Y.G. Li, J.Z. Wu, J. Feng, M. Lanza and H.J. Dai, Science 342 (2013) 836-840.

[59] M. El Baydi, S.K. Tiwari, R.N. Singh, J.-L. Rehspringer, P. Chartier, J.F. Koenig and G. Poillerat, Journal of Solid State Chemistry 116 (1995) 157-169.

[60] G.R. Li, F. Wang, Q.W. Jiang, X.P. Gao and P.W. Shen, Angewandte Chemie-International Edition 49 (2010) 3653-3656.

[61] M. Motlak, N.A.M. Barakat, M.S. Akhtar, A.M. Hamza, B.S. Kim, C.S. Kim, K.A. Khalil and A.A. Almajid, Electrochimica Acta 160 (2015) 1-6.

[62] K. Saranya, A. Subramania and N. Sivasankar, Rsc Advances 5 (2015) 43611-43619.

[63] H.N. Tsao, P. Comte, C.Y. Yi and M. Gratzel, Chemphyschem 13 (2012) 2976-2981.

[64] M. Liberatore, A. Petrocco, F. Caprioli, C. La Mesa, F. Decker and C.A. Bignozzi, Electrochimica Acta 55 (2010) 4025-4029.

[65] A. Hauch and A. Georg, Electrochimica Acta 46 (2001) 3457-3466.

[66] N. Papageorgiou, W.F. Maier and M. Grätzel, J. Electrochem. Soc. 144 (1997) 876-884.

Table:

Table 1.

Carbon	**Surface area (m^2/g)**	**Pore volume (cm^2/g)**	**Pore size (nm)**
N-MC	35	0.23	6.5
Co-N-MC	101	0.30	3.8
Ni-N-MC	218	0.48	3.8

Table 2.

Electrolyte	Electrode	R_s (Ω)	R_{ct} (Ω cm^2)	CPE (μF/cm^2)	j_0 (mA/cm^2)
I^-/I_3^-	Platinized	25.2 ± 0.4	4.7 ± 0.2	5.8 ± 0.3	2.7 ± 0.1
	N-MC	31.8 ± 0.5	6.3 ± 0.4	34.6 ± 0.3	2.0 ± 0.4
	Co-N-MC	26.9 ± 0.3	4.9 ± 0.5	42.7 ± 0.5	2.6 ± 0.4
	Ni-N-MC	26.6 ± 0.1	3.8 ± 0.3	49.8 ± 0.4	3.4 ± 0.2
T_2/T^-	Platinized	31.1 ± 0.2	44.2 ± 0.5	4.1 ± 0.5	0.29 ± 0.04
	N-MC	42.4 ± 0.3	21.3 ± 0.1	20.9 ± 0.2	0.60 ± 0.01
	Co-N-MC	40.2 ± 0.2	16.0 ± 0.4	40.4 ± 0.3	0.80 ± 0.04
	Ni-N-MC	33.3 ± 0.4	14.4 ± 0.5	63.6 ± 0.1	0.89 ± 0.01

Table 3.

Electrolyte	CE	V_{oc} (V)	J_{sc} (mA/cm^2)	FF	η (%)
I^-/I_3^-	Platinized	0.70 ± 0.01	17.8 ± 0.1	0.66 ± 0.05	8.22 ± 0.02
	N-MC	0.72 ± 0.01	14.2 ± 0.1	0.62 ± 0.01	6.34 ± 0.01
	Co-N-MC	0.72 ± 0.03	15.0 ± 0.3	0.70 ± 0.01	7.57 ± 0.01
	Ni-N-MC	0.73 ± 0.04	16.6 ± 0.4	0.70 ± 0.02	8.42 ± 0.02
T_2/T^-	Platinized	0.70 ± 0.03	16.6 ± 0.5	0.45 ± 0.03	5.25 ± 0.02
	N-MC	0.70 ± 0.01	15.9 ± 0.1	0.53 ± 0.01	5.90 ± 0.01
	Co-N-MC	0.70 ± 0.01	16.0 ± 0.2	0.60 ± 0.01	6.80 ± 0.01
	Ni-N-MC	0.71 ± 0.03	16.0 ± 0.3	0.62 ± 0.03	6.95 ± 0.02

Figure captions:

Figure 1. XRD patterns of the N-doped mesoporous carbon imbedded with (a) Co species and (b) Ni species.

Figure 2. XRD patterns of the N-doped mesoporous carbon, Co species, and Ni species imbedded in N-doped mesoporous carbons.

Figure 3. Surface morphology of (a) SBA-15, (b) Co-N-MC, and (c) Ni-N-MC.

Figure 4. EDX analysis of (a) Co-N-MC and (b) Ni-N-MC.

Figure 5. TEM images of (a) N-MC, (b) Co-N-MC, (c) Ni-N-MC and HRTEM images of (d) Co-N-MC, (d) Ni-N-MC samples.

Figure 6. Raman spectra of N-MC, Co-N-MC, and Ni-N-MC samples.

Figure 7. Nitrogen (77 K) adsorption−desorption isotherms of (a) N-MC, (b) Co-N-MC, and (c) Ni-N-MC samples (insets show the pore size distribution of the N-MC , Co-N-MC, and Ni-N-MC samples).

Figure 8. (a) XPS C 1s spectrum of N-MC, Co-N-MC and Ni-N-MC and (b) Atomic %C of each sample determined by XPS.

Figure 9. (a) Schematic representation of the different N-based functional groups detected on MC by XPS, (b) XPS N 1s spectrum of N-MC, Co-N-MC and Ni-N-MC, and (c) Atomic %N of each sample determined by XPS.

Figure 10. XPS spectra of (a) Co 2p of Co-N-MC and (b) Ni 2p of Ni-N-MC.

Figure 11. Cyclic voltammograms of the platinized, N-MC, Co-N-MC, and Ni-N-MC electrodes.

Figure 12. Potential-step chronoamperometry with the potential step from 0 V to 0.8 V for 10 s.

Figure 13. (a) Nyquist plots of EIS measured at 0 V from 10^6 to 0.1 Hz on the symmetrical dummy cells with platinized, N-MC, Co-N-MC, and Ni-N-MC as the counter electrodes

using I^-/I_3^- redox couple in acetonitrile and (b) Equivalent circuit diagram for fitting of EIS data.

Figure 14. Electrochemical stability of dummy cells with (a) platinized and (b) Ni-N-MC in acetonitrile solution of I^-/I_3^-. The sequence of measurements is as follows: 10 × CV scans (from 0 V → 1 V→ −1 V→ 0 V at a scan rate of 50 mVs^{-1}) followed by 30 s relaxation at 0 V and then EIS measurement at zero bias potential. The sequence of electrochemical tests was repeated 10 times. (c) R_{CT} versus EIS scan number.

Figure 15. Current-voltage characteristics of DSCs with platinized, N-MC, Co-N-MC, Ni-N-MC as the CEs in (a) I^-/I_3^- and (b) T_2/T^- electrolytes.

Figure 16. Nyquist plots measured at 0 V from 10^6 to 0.1 Hz on the symmetrical dummy cells with platinized, N-MC, Co-N-MC, and Ni-N-MC as the counter electrodes using T_2/T^- redox couple system.

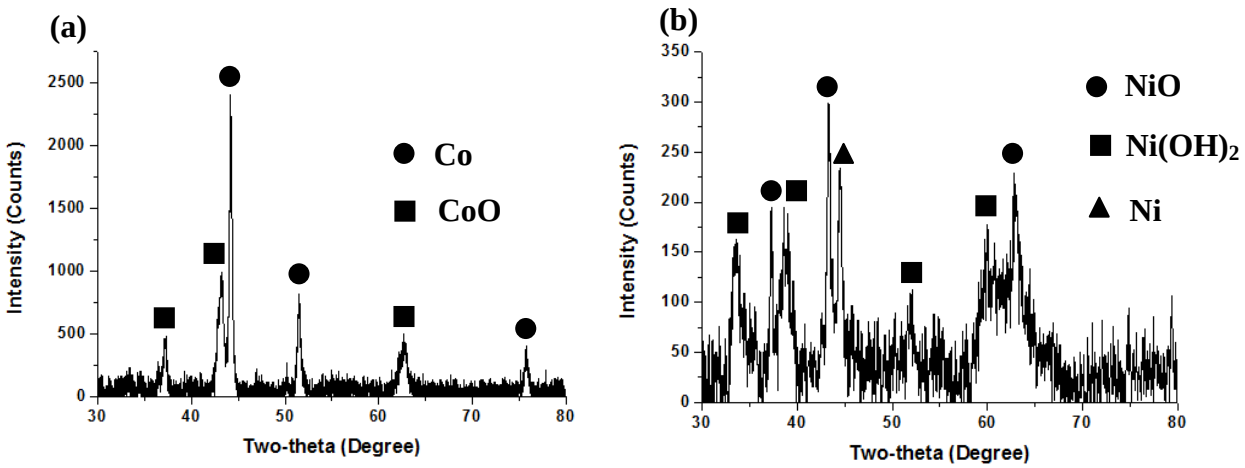
(a)
Intensity (Counts)
Two-theta (Degree)
Co
CoO
(b)
Intensity (Counts)
Two-theta (Degree)
NiO
Ni(OH)2
Ni

Figure 1.

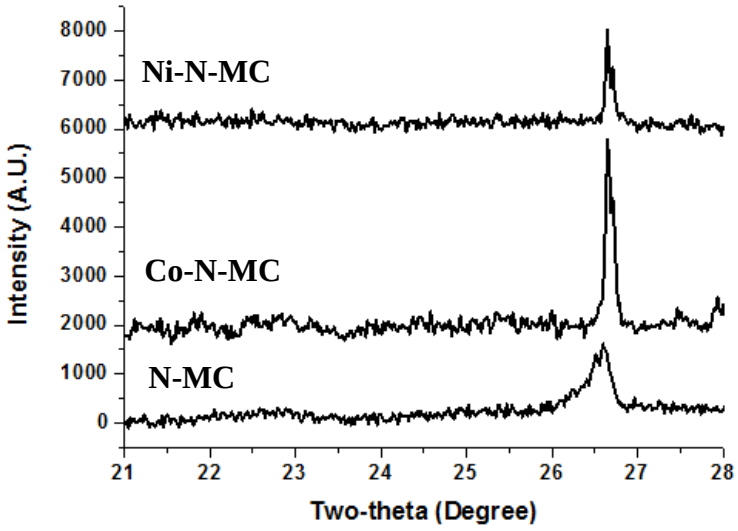
Ni-N-MC
Co-N-MC
N-MC
Intensity (A.U.)
Two-theta (Degree)
8000
7000
6000
5000
4000
3000
2000
1000
0
21
22
23
24
25
26
27
28

Figure 2.

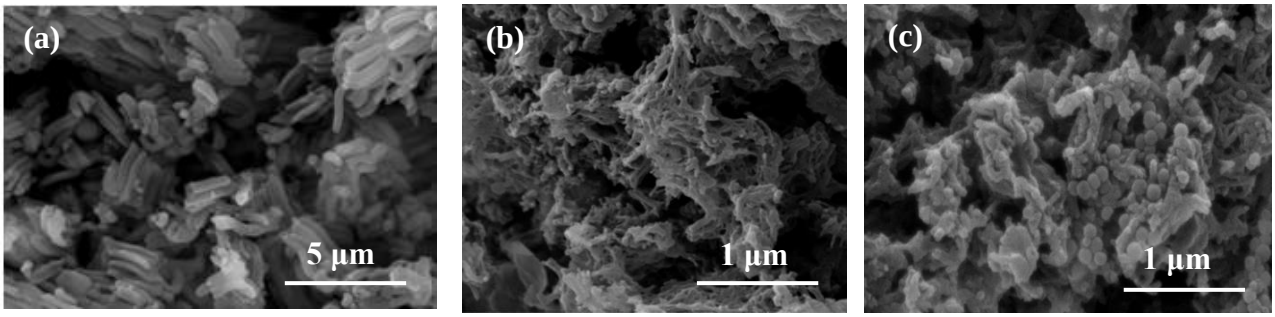

Figure 3.

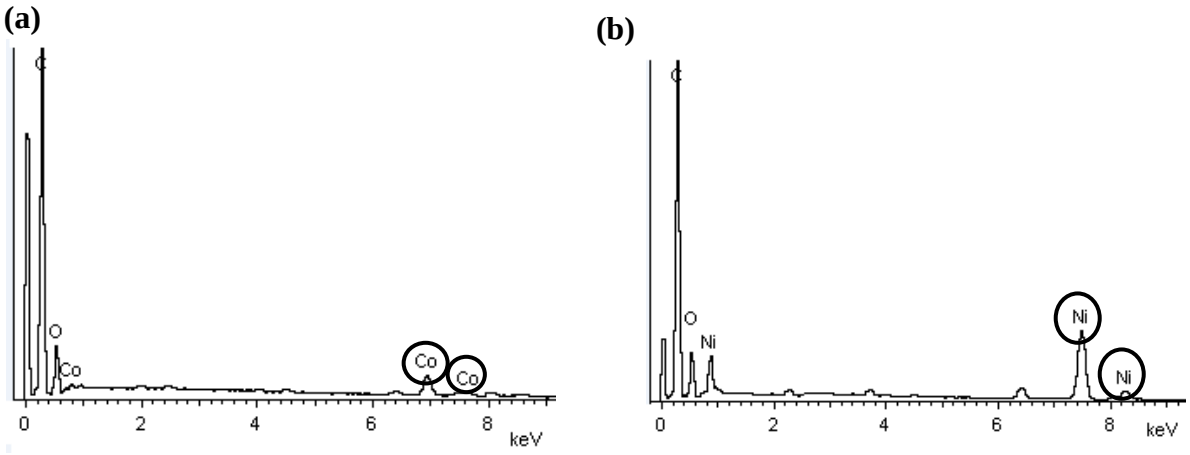

Figure 4.

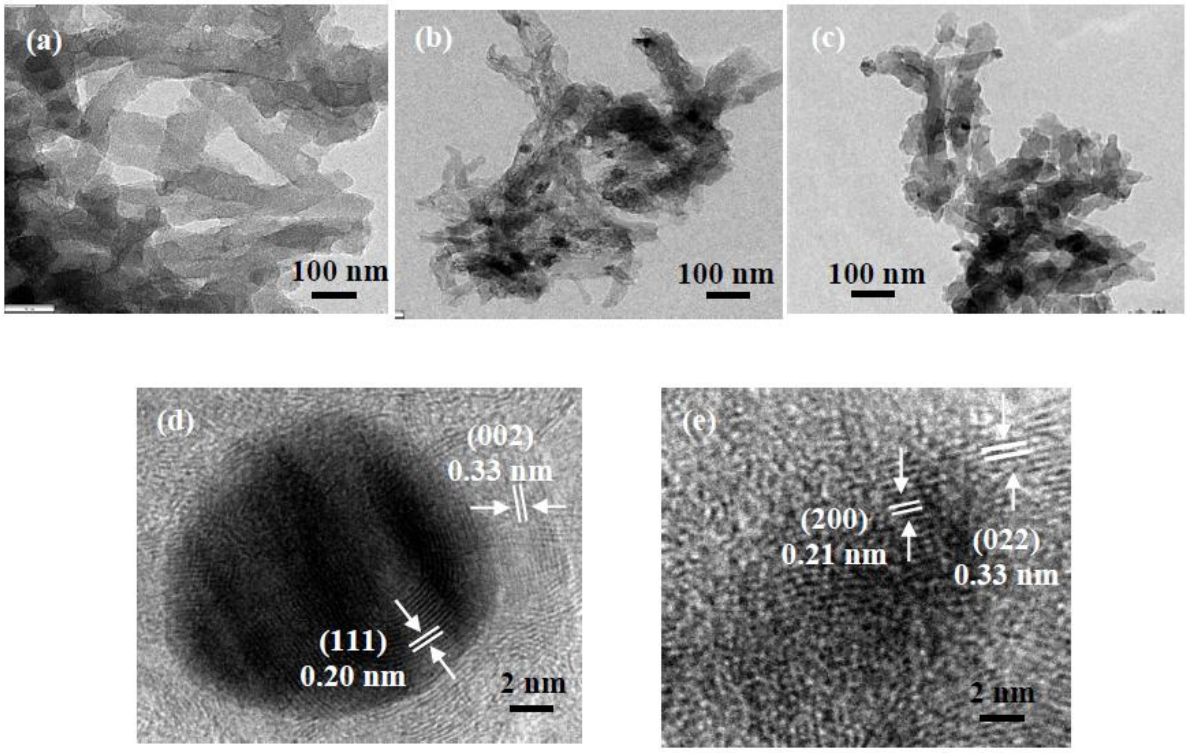
(a)
100 nm
(b)
100 nm
(c)
100 nm
(d)
(002)
0.33 nm
(111)
0.20 nm
2 nm
(e)
(200)
0.21 nm
(022)
0.33 nm
2 nm

Figure 5.

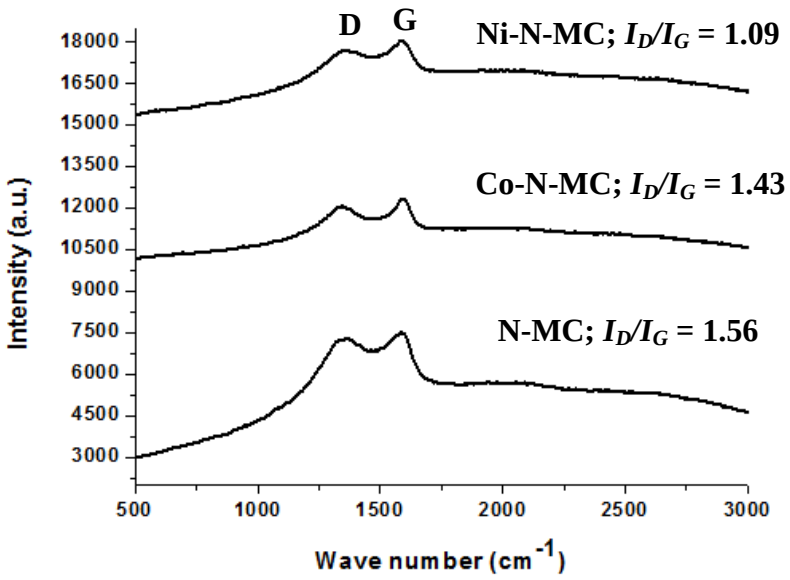
D
G
Ni-N-MC; I_D/I_G = 1.09
Co-N-MC; I_D/I_G = 1.43
N-MC; I_D/I_G = 1.56
Intensity (a.u.)
18000
16500
15000
13500
12000
10500
9000
7500
6000
4500
3000
500
1000
1500
2000
2500
3000
Wave number (cm^{-1})

Figure 6.

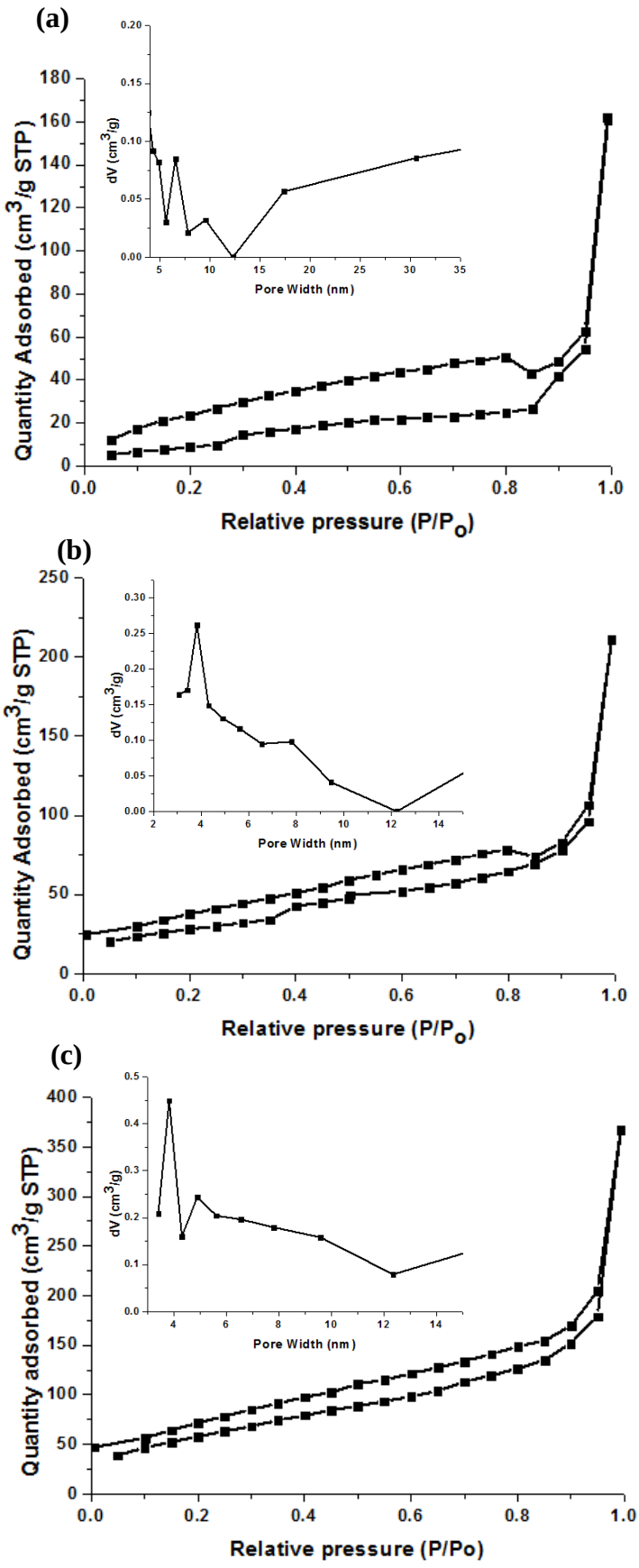
(a)
Quantity Adsorbed (cm3/g STP)
Relative pressure (P/Po)
dV (cm3/g)
Pore Width (nm)
(b)
Quantity Adsorbed (cm3/g STP)
Relative pressure (P/Po)
dV (cm3/g)
Pore Width (nm)
(c)
Quantity adsorbed (cm3/g STP)
Relative pressure (P/Po)
dV (cm3/g)
Pore Width (nm)

Figure 7.

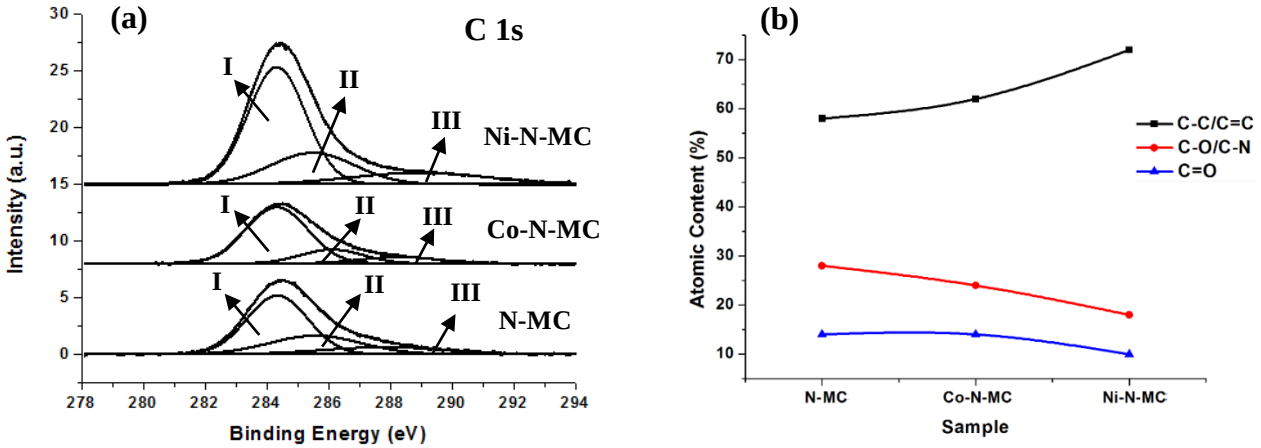
(a)
C 1s
I
II
III
Ni-N-MC
Co-N-MC
N-MC
Intensity (a.u.)
Binding Energy (eV)
(b)
C-C/C=C
C-O/C-N
C=O
Atomic Content (%)
N-MC
Co-N-MC
Ni-N-MC
Sample

Figure 8.

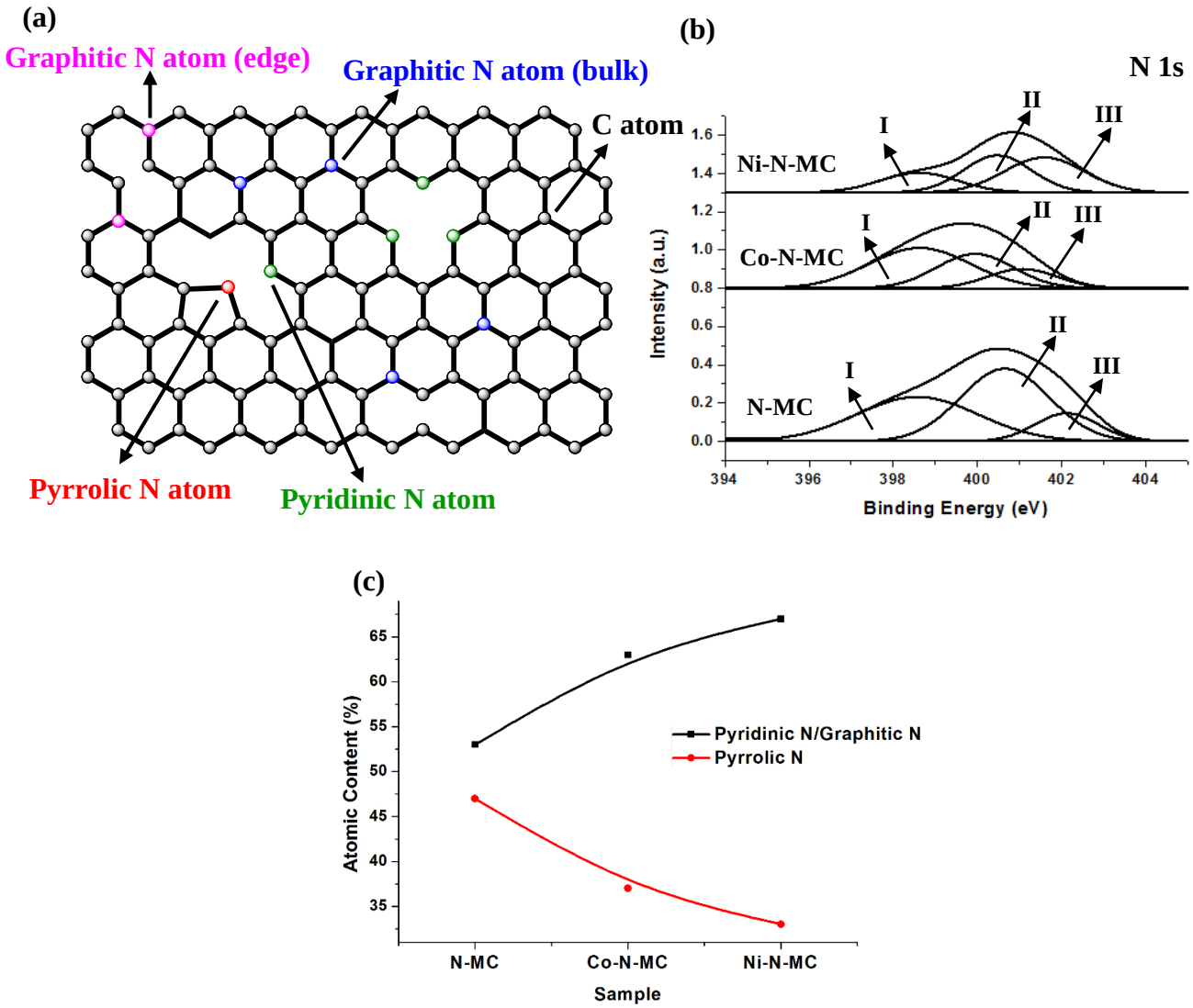
(a)
Graphitic N atom (edge)
Graphitic N atom (bulk)
C atom
Pyrrolic N atom
Pyridinic N atom
(b)
N 1s
Ni-N-MC
Co-N-MC
N-MC
I
II
III
Intensity (a.u.)
Binding Energy (eV)
(c)
Atomic Content (%)
Pyridinic N/Graphitic N
Pyrrolic N
N-MC
Co-N-MC
Ni-N-MC
Sample

Figure 9.

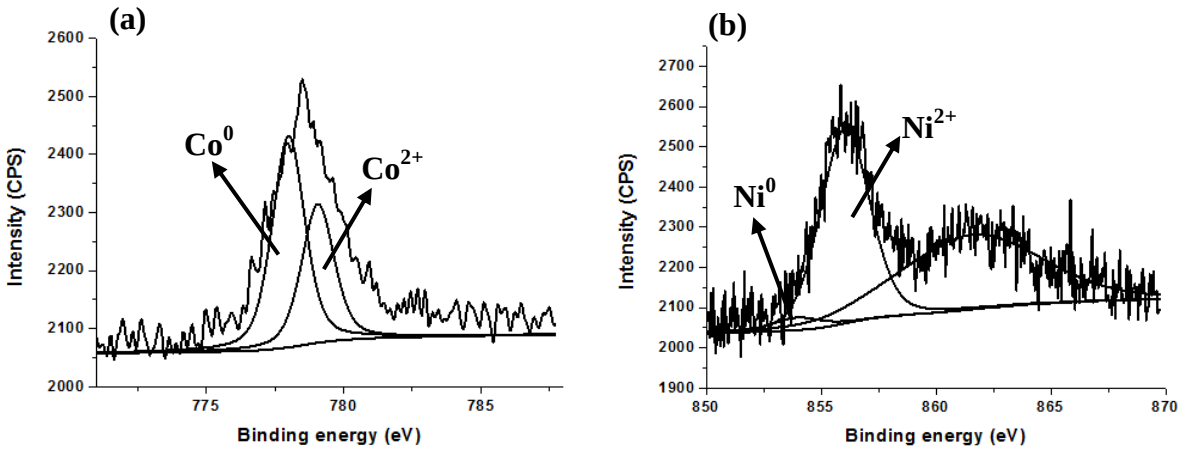
(a)
Co0
Co2+
Intensity (CPS)
Binding energy (eV)
(b)
Ni0
Ni2+
Intensity (CPS)
Binding energy (eV)

Figure 10.

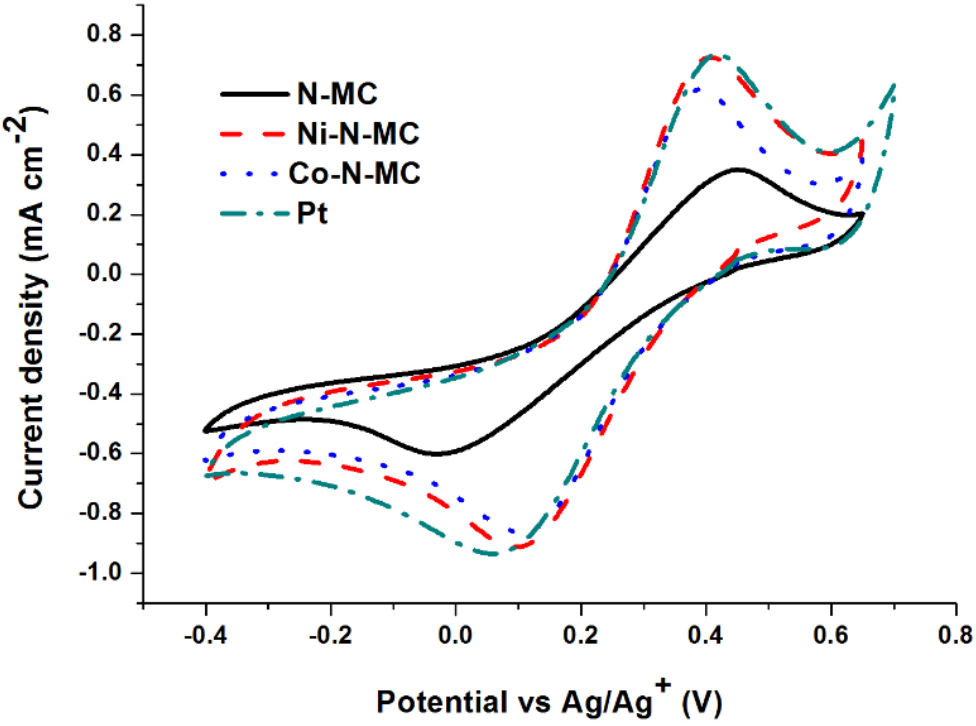
N-MC
Ni-N-MC
Co-N-MC
Pt
Current density (mA cm-2)
Potential vs Ag/Ag+ (V)
0.8
0.6
0.4
0.2
0.0
-0.2
-0.4
-0.6
-0.8
-1.0
-0.4
-0.2
0.0
0.2
0.4
0.6
0.8

Figure 11.

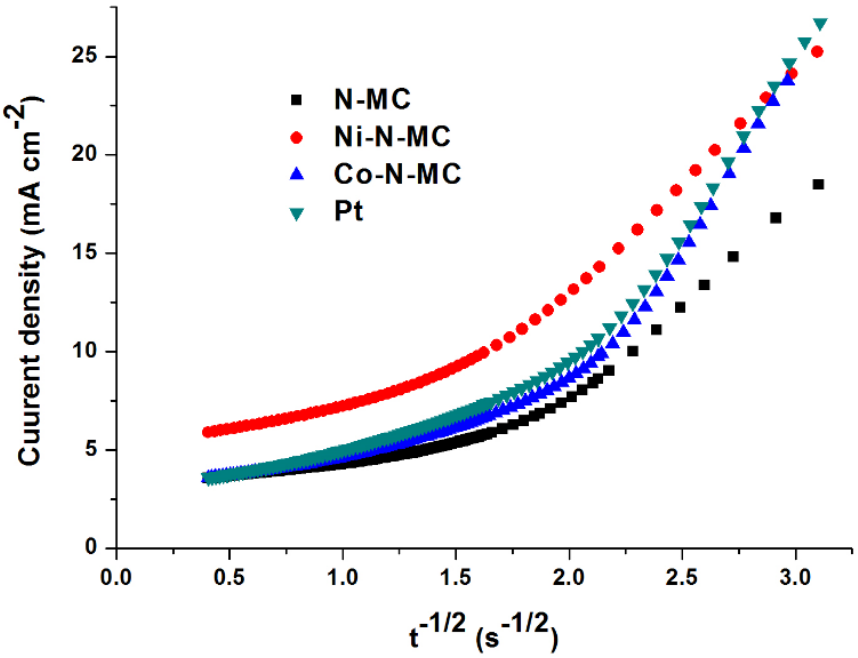
N-MC
Ni-N-MC
Co-N-MC
Pt
Cuurent density (mA cm-2)
t-1/2 (s-1/2)
0
5
10
15
20
25
0.0
0.5
1.0
1.5
2.0
2.5
3.0

Figure 12.

(a)

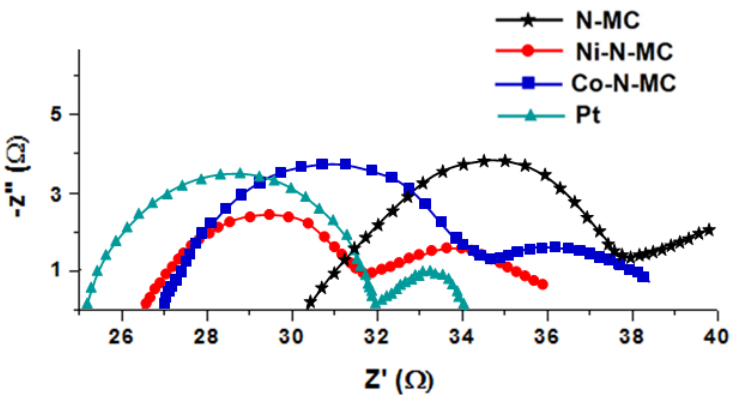

(b)

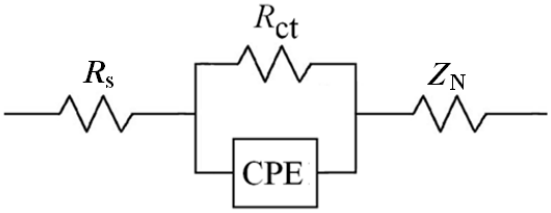

Figure 13.

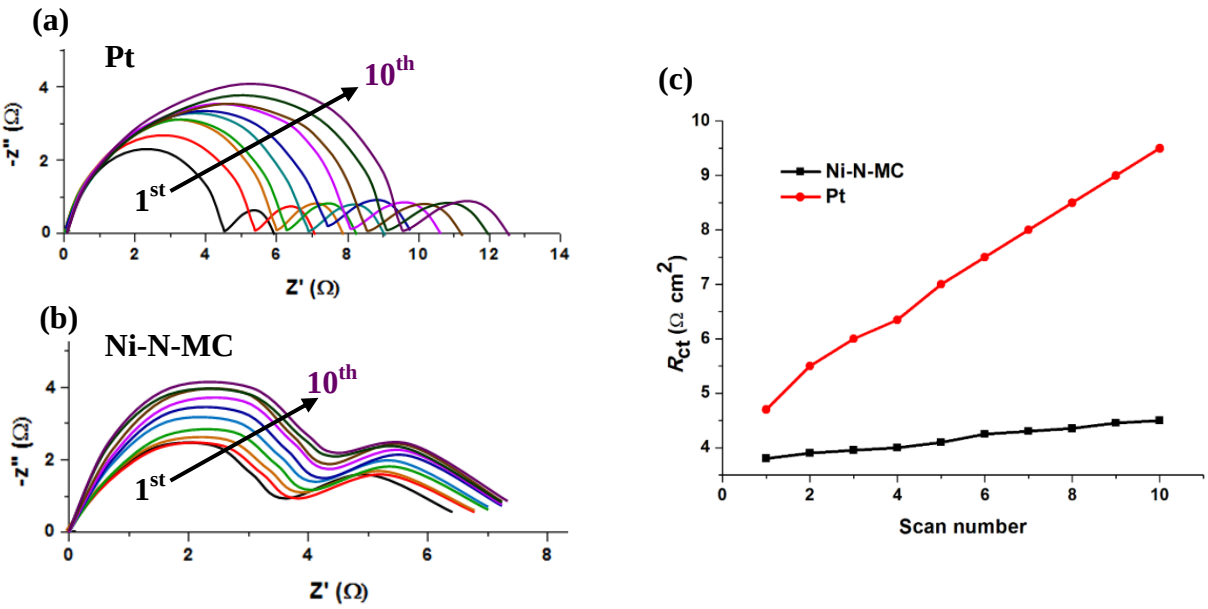
(a)
Pt
10th
1st
-Z'' (Ω)
Z' (Ω)
(b)
Ni-N-MC
10th
1st
-Z'' (Ω)
Z' (Ω)
(c)
Ni-N-MC
Pt
Rct (Ω cm2)
Scan number

Figure 14.

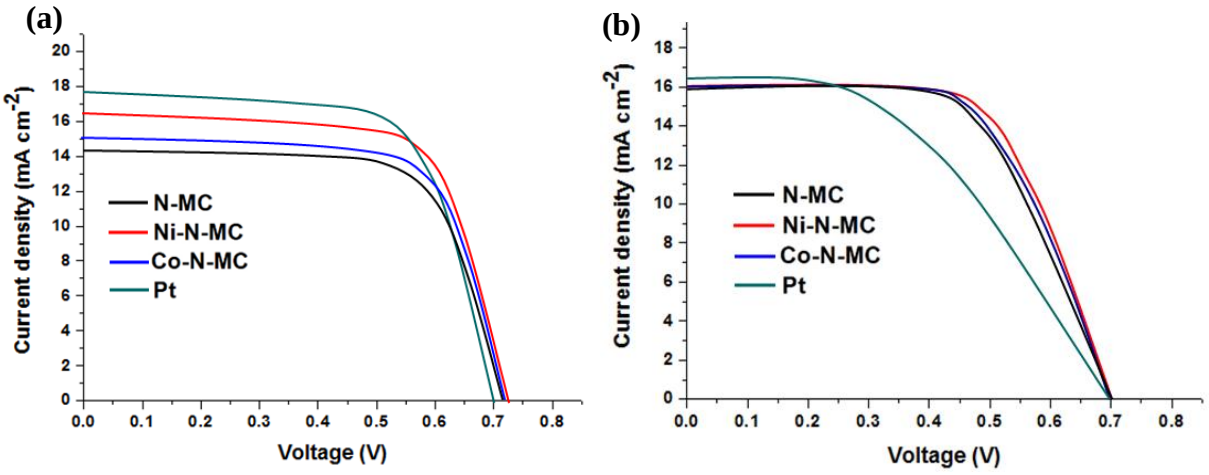
(a)
Current density (mA cm-2)
Voltage (V)
N-MC
Ni-N-MC
Co-N-MC
Pt
(b)
Current density (mA cm-2)
Voltage (V)
N-MC
Ni-N-MC
Co-N-MC
Pt

Figure 15.

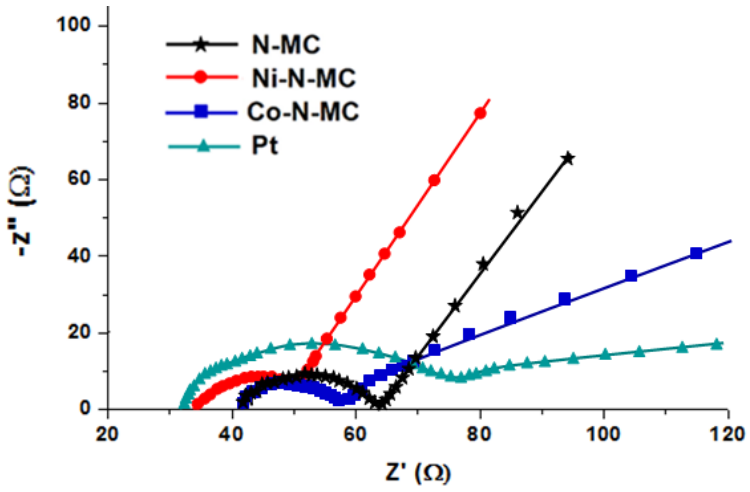

Figure 16.